

ABSTRACT

ANAND, NADISH. Application of Ferrohydrodynamic Flows for Heat Transfer Enhancement and Energy Harvesting. (Under the direction of Dr. Richard Gould).

Ferrofluid flow manipulation applications have been around for a few decades now. However, their applicability is increasing with the further advance in nano-technology, and the development of multiphysics systems. There have been a lot of numerical studies on ferrofluid flows which have focused on simulation of ferrofluids using different constitutive models and magnetic field conditions. However, the numerical simulations using multiphysics finite element codes are usually rare. With this motivation two applications of ferrofluid flows are explored in this research. The first application pertains to heat transfer and the second pertains to energy harvesting. The numerical multiphysics simulations are planned and executed in such a way that the complexity of the analysis increases as one progresses through the work. The first application is completely a steady-state flow analysis while the second application is an unsteady flow.

The first application pertaining to heat transfer enhancement in ferrofluid flows is bifurcated into two configurations. The first configuration investigated the enhancement in 'self-mixing' when a ferrofluid flow inside a 90° bend channel is subjected to two magnetic fields, one strong and one weak. This study introduced a mixing viscosity term in the momentum equation of the Navier Stokes equations, which depicted the effect of the magnetization and the applied magnetic field not being sensibly collinear. The non-uniform magnetic field applied on the bend channel is by using two parametrically placed wires which can carry current in either directions. This gave rise to symmetric and anti-symmetric cases for the magnetic field. In order to study the mixing enhancement three mixing scalars based on velocity amplification of the flow were introduced to study the effects on both local and global flow characteristics. The second configuration is similar to the one in mixing enhancement, however the non-collinearity between

the magnetization and magnetic field is removed and an additional channel which has an external radius twice that of the original channel is introduced. Here, a heat flux is applied to the boundary of the channels and different channel parameters were varied to obtain variation of Nusselt number (or heat transfer enhancement) with these parameters. The highest local and global heat transfer enhancements were of the order of 600% and 160% for the smaller channel, respectively. For the larger channel, these values were smaller as compared to the smaller channel but were significant.

The second application studied was energy harvesting from sloshing motion of the ferrofluid placed inside a container with a non-uniform magnetic field. This application was also studied through two configurations. In the first configuration a rectangular symmetric ferrofluid vibration energy harvester is proposed, which has four magnets symmetrically placed to impart non-uniform magnetic field. The system was parametrized in terms of the significant length scale and was studied for variation in the significant length scale and the polarity of the magnets placed around the sloshing container. Other parameters like the fill level of the ferrofluid, distance of magnets, and external acceleration were not varied. The maximum harvested power was $20 \mu\text{W}$ which was for a particular case of magnet polarity, and for the tank with $L = 10 \text{ cm}$. For the tank with $L = 5 \text{ cm}$ the maximum power harvested was around $0.7 \mu\text{W}$, which is significantly lower. Hence, establishing size effects on the potential for energy harvesting from ferrofluid sloshing vibration energy harvester. The second configuration studied is a hybrid energy harvester, in which the sloshing tank has a piezoelectric bimorph for harvesting energy through both ferrofluid motion and the deflection of the piezoelectric bimorph through the fluid structure interaction between ferrofluid and the beam. The aim of the study was to evaluate the feasibility of such a hybrid system, and it was found that the system is feasible and can be made more efficient through system optimization.

© Copyright 2020 by Nadish Anand

All Rights Reserved

Application of Ferrohydrodynamic Flows for Heat Transfer Enhancement and Energy
Harvesting

by
Nadish Anand

A thesis submitted to the Graduate Faculty of
North Carolina State University
in partial fulfillment of the
requirements for the degree of
Doctor of Philosophy

Mechanical Engineering

Raleigh, North Carolina
2020

APPROVED BY:

Richard Gould
Committee Chair

Alexei Saveliev

Tiegang Fang

Matthew Bryant

Warren Jasper

DEDICATION

This work is a tribute to my maternal grandmother Smt. Sunderbai Bukhariya

BIOGRAPHY

Nadish Anand was born in the city of Indore in the state of Madhya Pradesh, India. He attended the National Institute of Technology, Calicut for his baccalaureate degree in mechanical engineering (B.Tech.). Thereafter he worked for Bharat Petroleum Corporation Limited (BPCL) from 2010 to 2013, in the capacity of Assistant Manager Operations. After that he attended North Carolina State University for his MS and PhD in mechanical engineering. His work is very diverse, and under the guidance of Prof. Richard Gould he has worked on developing low order thermal modeling of single floored houses for his MS thesis. After that he started working on his dissertation research on applications of Ferrohydrodynamic flows under the guidance of Dr. Gould. In his PhD work he has also been involved with research work in the college of Textiles with Dr. Warren Jasper on the topics of contact angle, wetting and thermal comfort properties of textiles.

ACKNOWLEDGEMENTS

Although writing this work (not actually doing it) has been a tough job for me, however the toughest part is writing this section. For any endeavor especially as arduous as a PhD one gets help, motivation, and support in numerous ways (both direct and indirect). Without this help, motivation, and support, the success of such endeavors hangs in balance and are seldom successful. I believe that this work is a success, and it is not because of my efforts alone but it is because of the countless people who have helped me throughout this journey. Firstly, I would like to thank my advisor Dr. Richard Gould for his constant support and motivation throughout this journey, right from the day of my master's degree. This has been one of the most fruitful associations of my life. Secondly, I would like to thank Dr. Warren Jasper for providing me with two additional topics of research in addition to this work, which helped me gain a lot of research experience, while learning a lot from him personally. It was an amazing experience working with both of you. I would also like to thank Dr. Alexei Saveliev, Dr. Tiegang Fang and Dr. Matthew Bryant for being on my committee and for being amazingly understanding through multiple delays in my defense. I would also like to mention that your suggestions have made this work even better than originally thought.

I would like to thank my family for their constant support and faith in me. This work is truly a testament to their painstaking efforts in assuring that I get the best education and the freedom to pursue the toughest of endeavors in life.

I want to thank all my friends Pranav, Yesaswi, Aravind, Karthik, Nadish Saini, Megan, Hey-Sang, Vikram for being amazing colleagues and my go-to resource when I am stuck or had a bad day. Thank you, guys, your support made this work possible. I would also like to thank my

roommates Badal, Lucky, Haritha, Shreyas, Chatty and Mithilesh for never making any moment seem dull.

Finally, I want to thank the people of the state of North Carolina and those of the United States of America. This work could not have been possible without your invisible help and hospitality, that helped me stay comfortably and pursue higher learning.

TABLE OF CONTENTS

LIST OF TABLES	viii
LIST OF FIGURES	ix
PART I: Introduction to this work.....	1
PART II: Mixing and Heat Transfer Enhancement.....	4
Chapter 1: Introduction	6
Chapter 2: Mixing Enhancement in an Elbow Channel	8
1. Introduction.....	8
2. Model Geometry and Ferrofluid Properties.....	9
2.1 Geometry	9
2.2 Ferrofluid Properties.....	12
3. Governing Equations	13
3.1 Governing Equations.....	13
3.2 Details of Numerical Modeling.....	15
4. Results and Discussions.....	18
4.1 Comparison of mixing for the two cases.....	23
5. Conclusions.....	28
Chapter 3: Heat Transfer Enhancement in Elbow Channels.....	31
1. Introduction.....	31
2. System Configuration	32
3. Governing Equations	35
4. Numerical Modeling	39
5. Results and Discussions.....	41
5.1 Results for Channel 1	41
5.2 Results for Channel 2	46
6. Conclusions.....	49
PART III: Application of Ferrohydrodynamic Flows for Energy Harvesting	50
Chapter 1: Introduction	51
1. Energy Harvesting.....	51
2. Fluidic Energy Harvesting through Solid State Transduction Mechanisms	53
2.1 Ionic Polymer Metal Composites	53
2.2 Piezoelectric Energy Harvesting Using Flow Induced Vibrations.....	57

2.3 Piezoelectric Energy Harvesting Using Airfoil Fluttering	62
2.4 Acoustic Energy Harvesting Using Sonic Crystals and Piezoelectric Beam	64
3. Energy Harvesting Through Liquid State Transduction Mechanism.....	65
3.1 Ferrofluid Sloshing Based Energy Harvester	66
Chapter 2: Analysis of a Symmetrical Ferrofluid Sloshing Vibration Energy Harvester	70
1. Introduction.....	70
2. Geometry and setup	71
3. Governing Equations	72
4. Numerical Modeling and Validation	77
5. Results and Discussion	80
5.1 Analysis of output from L = 10 cm tank	81
5.2 Analysis of Output from L = 5 cm tank	88
6. Conclusion	95
Chapter 3: Feasibility Study of a Hybrid Solid – Liquid Vibration Energy Harvester	97
1. Introduction.....	97
2. Problem setup.....	98
3. Governing Equations	100
4. Numerical Modeling	104
5. Results & Discussion	106
6. Conclusion	112
REFERENCES.....	113
APPENDICES	129
Appendix A: Surface Evolution for L =10 cm tank	129
Appendix B: Voltage Evolution plots for different cases	137
1. For PZT7A	137
2. For PVDF	141
Appendix C: Physical properties of materials.....	145

LIST OF TABLES

Table 1	Ferrofluid property data.....	13
Table 2	Parameters and their variation limits.....	16
Table 3	Current Direction and cases	17
Table 4	Ferrofluid physical properties	38
Table 5	Parameter varied for simulation and their values/limits.....	40
Table 6	Cases for current flowing in wire 1 and wire 2	41
Table 7	Cases for Magnet orientation	80
Table 8	Summary of properties of coils for $L = 10$ cm tank.....	82
Table 9	Summary of properties of coils for $L = 5$ cm tank.....	90
Table 10	Simulation cases for energy harvester.....	105

LIST OF FIGURES

Figure 1	Zoomed out view of the problem geometry.....	9
Figure 2	Schematic view of elbow channel and external wires	10
Figure 3	Channel bend with the two current carrying conductors	10
Figure 4	Mesh of the whole domain.....	11
Figure 5	Structured mesh in the channel.....	12
Figure 6	Grid convergence for $I = 6A$. a) case 4, b) case 3.....	17
Figure 7	Magnetic Flux density norm for $I=6A$. Top plot - case 1, Bottom plot - case 2.....	19
Figure 8	Velocity magnitude plot for $I = 6A$ for a) case 4, b) case 3, and c) no current	20
Figure 9	Velocity magnitude plot for $I = 6 A$ for a) case 1, b) case 2, and c) no current	22
Figure 10	Mixing number in the bend for $I=6 A$ a) case 2&1 and b) case 3&4	24
Figure 11	Mixing scalar 1 for same & opposite current cases a) Location 1 case 1&2, b) Location 1 case 3&4, c) Location 2 case 1&2, d) Location 2 case 3&4, e) Location 3 case 1&2 and f) Location 3 case 3&4.....	26
Figure 12	Mixing scalar 2 for $I=6A$ for a) Location 1 case 1&2, b) Location 1 case 3&4, c) Location 2 case 1&2, d) Location 2 case 3&4, e) Location 3 case 1&2 and f) Location 3 case 3&4	27
Figure 13	Configuration of the elbow channel.....	32
Figure 14	Elbow channel bend for outer radius of 2 channel widths.....	33
Figure 15	Angular position of the wires with respect to the horizontal for a),b) and c) outer radius of $2w_0$ and d),e) and f) outer radius of $4w_0$	34
Figure 16	Velocity magnitude plot for $2w_0$ channel for $\alpha = 45^\circ$ for $Re = 5$ for a) Case 1 b) Case 2 c) Case 3 d) Case 4 e) Case 5 f) Case 6 g) Case 7 h) Case 8 i) Case 9.....	42
Figure 17	Nusselt number for $2w_0$ channel for a) Channel with $\alpha = 30^\circ$ b) Channel with $\alpha = 45^\circ$ c) Channel with $\alpha = 60^\circ$ d) Bend with $\alpha = 30^\circ$ e) Bend with $\alpha = 45^\circ$ f) Bend with $\alpha = 60^\circ$	43
Figure 18	% increase in Nusselt number for $2w_0$ channel for a) Channel with $\alpha = 30^\circ$ b) Channel with $\alpha = 45^\circ$ c) Channel with $\alpha = 60^\circ$ d) Bend with $\alpha = 30^\circ$ e) Bend with $\alpha = 45^\circ$ f) Bend with $\alpha = 60^\circ$	45

Figure 19 Nusselt number for $4w_0$ case for a) Channel with $\alpha = 30^\circ$ b) Channel with $\alpha = 45^\circ$ c) Channel with $\alpha = 60^\circ$ d) Bend with $\alpha = 30^\circ$ e) Bend with $\alpha = 45^\circ$ f) Bend with $\alpha = 60^\circ$	47
Figure 20 (%) increase in Nusselt number for $4w_0$ case for a) Channel with $\alpha=30^\circ$ b) Channel with $\alpha=45^\circ$ c) Channel with $\alpha=60^\circ$ d) Bend with $\alpha=30^\circ$ e) Bend with $\alpha=45^\circ$ f) Bend with $\alpha=60^\circ$	48
Figure 21 Schematic representation of an energy harvesting device	51
Figure 22 Classification of Fluidic Energy Harvesting methods	52
Figure 23 Energy harvesting from IPMC attached to a flapping flag [91]	54
Figure 24 Energy harvesting from IPMC by the action of an oscillating fluid a) &b) experimental setup, c) schematics [99].....	55
Figure 25 Energy harvesting from IPMC energy harvester by action of vortex induced deformation [102], [103].....	57
Figure 26 Aeroelectromechanical coupling in flow based piezoelectric energy harvesters [75]	58
Figure 27 Piezoelectric in the wake of a bluff body a, b- side view of vortex interacting with a PVDF beam a PIV image , c- top view of the experimental setup [107], [110]	60
Figure 28 a) Schematic top and side view of the bluff body attached harvester and b) Experimental setup	61
Figure 29 A general 2 DOF aero elastic energy harvester configuration [74], [81]	62
Figure 30 Airfoil based energy harvesters a) Piezo aeroelastic b) Electromagnetic Induction based [81], [119]	63
Figure 31 Energy harvesting from acoustic waves by using sonic crystals a) schematic representation and b) experimental setup	65
Figure 32 A Cylindrical Ferrofluid based Vibration Energy Harvester [23]	67
Figure 33 Schematic representation of a rectangular Ferrofluid sloshing tank for vibration energy harvesting [24]	69
Figure 34 Schematic representation of the proposed harvester configuration	71
Figure 35 Harvester and the large domain surrounding it.....	72
Figure 36 Comparison between a) 1H configuration of Liu[24] and b) present work.....	79
Figure 37 Surface evolution and magnetic flux density arrow surface for case 1, near resonance frequency for $L=10$ cm tank	81

Figure 38 RMS voltage plots for Cases 1-16 while considering horizontally wound coil for L = 10 cm tank.....	83
Figure 39 RMS voltage plots for Cases 1-16 while considering vertically wound coil for L=10 cm tank	84
Figure 40 Maximum power output from horizontal coil for L = 10 cm tank.....	86
Figure 41 Maximum power output from vertical coil for L = 10 cm tank.....	87
Figure 42 Surface evolution and magnetic flux density arrow surface for case 1, near resonance frequency for L = 5 cm tank	88
Figure 43 RMS voltage plots for Cases 1-16 while considering horizontally wound coil for L=5 cm tank	91
Figure 44 RMS voltage plots for Cases 1-16 while considering vertically wound coil for L=5 cm tank	92
Figure 45 Maximum power output from Horizontal winding for L = 5cm tank.....	93
Figure 46 Maximum power output from Vertical winding for L = 5cm tank.....	95
Figure 47 Configuration of the hybrid VEH system a) the tank and piezo bimorph and b) close-up of the piezo bimorph	99
Figure 48 Magnetic Field function.....	99
Figure 49 Meshing of the domain of Energy harvester.....	104
Figure 50 Flow Evolution for a) PZT7A and b) PVDF for f = 1 Hz at t = 0.47 sec	107
Figure 51 RMS total voltage for a) PZT-7A and b) PVDF and Voltage from sloshing from c) PZT-7A and d) PVDF.....	108
Figure 52 Graph for a) Magnetic field function 1 and b) Magnetic field function 2, for $H_{max} = 20[kA/m]$	109
Figure 53 Total RMS voltage for PVDF for a) Magnetic function 1 b) magnetic function 2 and sloshing voltage for PVDF for a) magnetic function 1 and b) magnetic function 2	110
Figure 54 Case 2.....	129
Figure 55 Case 3.....	129
Figure 56 Case 4.....	130
Figure 57 Case 5.....	130
Figure 58 Case 6.....	131

Figure 59 Case 7.....	131
Figure 60 Case 8.....	132
Figure 61 Case 9.....	132
Figure 62 Case 10.....	133
Figure 63 Case 11.....	133
Figure 64 Case 12.....	134
Figure 65 Case 13.....	134
Figure 66 Case 14.....	135
Figure 67 Case 15.....	135
Figure 68 Case 16.....	136
Figure 69 Case1 time evolution for different frequencies with PZT7A.....	137
Figure 70 Case2 time evolution for different frequencies with PZT7A.....	138
Figure 71 Case3 time evolution for different frequencies with PZT7A.....	139
Figure 72 Case4 time evolution for different frequencies with PZT7A.....	140
Figure 73 Case1 time evolution for different frequencies with PVDF	141
Figure 74 Case2 time evolution for different frequencies with PVDF	142
Figure 75 Case3 time evolution for different frequencies with PVDF	143
Figure 76 Case4 time evolution for different frequencies with PVDF	144

PART I: Introduction to this work

Flow manipulation via non-invasive tactics has a plethora of applications in today's world with increasingly complex engineering requirements to solve modern problems[1]–[3]. Flow manipulation is often used as a technique in external flows, such as cooling jet impingement and propulsion via thrust vectoring[4], [5], and in internal flow applications such as rough pipe flow and droplet dynamics of nanofluids, etc.[6], [7]. There are many different methods for flow manipulation, which can be broadly classified into active and passive methods. Passive methods involve the manipulation of flow through permanent structures or surfaces, for example pipes with rough walls, corrugated channels, etc.[8] Active methods, involve tunable flow control, generally by means of an external force field, which is usually an electric field or magnetic field. Since, magnetic and electric field effects are especially strong over shorter distances, active flow control with these forces is unusually useful for micro-scale applications[9], [10].

In recent times with the advancement in nanotechnology and particularly nano-fluidics and colloidal chemistry, new nano-fluids have been developed which can be actively controlled through the application of electric or magnetic forces. One such fluid is a ferrofluid, which can be controlled through external magnetic field, and in cases where conductive particles are involved, through an electric field as well[11]–[13].

Ferrofluids are colloidal suspensions of ceramic coated nanosized ferromagnetic particles like magnetite, titanium dioxide etc., in a base fluid (or carrier fluid), which exhibit a fundamental property known as super-paramagnetism. Super-paramagnetism allows the ferrofluid to orient itself in the direction of an externally applied magnetic field, as the ferromagnetic particles become magnetized [11]. This unique property paves the way for various engineering applications of

ferrofluids involving active flow control, like self-pumping, electronic cooling, mixing, navigation, refrigeration, lab on chip applications, microfluidics etc.[14].

Mixing enhancement for chemical engineering of internal flows has been an area of interest for a long time[15], [16]. Similarly, mixing enhancement, is also being used for lab on chip applications and for drug delivery applications[17], [18]. Furthermore, cooling applications at the microscale and liquid cooling applications have been at the very forefront of modern cooling problems for electronics. Ferrofluids are actively being utilized to solve both mixing and heat transfer enhancement problems[19]–[22].

Recently, ferrofluids have been utilized to generate energy through vibration energy harvesting[23]. Here, the ferrofluid serves as both the transduction mechanism and the energy harvesting element, behaving similar to a moving magnet. This problem is studied experimentally and computationally for a fixed configuration[24], [25]. In this work two different areas of applications of ferrofluids are explored.

This dissertation is divided into two parts. Each part deals with two problems/configurations in the same area of application of ferrofluids. The first part (part II) deals with the application of ferrofluids for mixing and heat transfer enhancement. The geometry considered in this section is a 2-D, 90° elbow channel, with different boundary conditions on the electromechanical components, to achieve mixing and heat transfer enhancement.

In the second part (part III) two configurations of ferrofluid vibration energy harvesting are introduced and studied numerically. The first is a symmetric energy harvester with four permanent magnets, tested using different magnet configurations and different length scales. The parameters responsible for power conversion in the energy harvester are analyzed for different significant length scales of the system. The second configuration considered is a hybrid sloshing-piezoelectric

energy harvester, where the energy is harvested by means of ferrofluid sloshing and ferrofluid-piezoelectric fluid-structure interaction. The feasibility of this system is analyzed, and the impacts of significant parameters are discussed.

PART II: Mixing and Heat Transfer Enhancement

The nomenclature for this section is as follows:

w_0	Width of the channel	α	Angle made by line joining the wires with horizontal
L_0	Length of the channel	R_{out}	Outer radius of the bend
χ_m	Magnetic Susceptibility of the ferrofluid	T	Temperature
U	Inlet Velocity	Nu_{ch}	Nusselt Number for the whole channel
\vec{V}	Velocity vector	Nu_{bend}	Nusselt number for the bend
Re	Flow Reynolds Number	Nu_{bend1}	Nusselt number in the first bend section
u	x component of velocity	Nu_{bend2}	Nusselt number in the second bend section
v	y component of velocity	k_p	Thermal conductivity of particles
η	Dynamic viscosity of the ferrofluid	k_L	Thermal conductivity of carrier liquid
ρ	Density of the ferrofluid	η_L	Dynamic viscosity of carrier liquid
$I_1 \& I_2$	Current magnitude in the current carrying wires	ρ_L	Density of the carrier liquid
M_s	Initial Magnetization of the ferrofluid	ρ_p	Density of ferromagnetic particles
$dist1$	Distance of the wire center from the channel center	C_{pL}	Specific heat of the carrier liquid
N_{cell}	Mesh refinement parameter	C_{pp}	Specific heat of ferromagnetic particles
H	Magnetic field generated from the wires	d	Diameter of ferromagnetic particles
B	Magnetic Flux Density	μ_B	Bohr Magneton ($9.27 \times 10^{-27} Am^2$)
Eu	Euler Number	T_{ref}	Reference temperature
N_{mix}	Mixing Number	ϕ	Volume fraction of ferrofluid
N_{mix1}	Mixing Scalar 1	m	Magnetic moment of ferromagnetic particles
N_{mix2}	Mixing Scalar 2	n	Number density of ferromagnetic particles
p	Pressure	k_B	Boltzmann constant ($1.38 \times 10^{-23} J/K$)
μ_0	Permeability of free space $4\pi \times 10^{-7} N/A^2$	M_d	Saturation magnetization for magnetite (423 kA/m)

Chapter 1: Introduction

Mixing enhancement by the action of magnetic nanofluids has been a widely studied topic, and has been utilized for process intensification in various manufacturing processes, particularly pertaining to lab-on-a-chip applications[26], [27]. Usually, for process intensification or mixing applications, a spatially non-uniform magnetic field[28]–[30] is used, with some applications utilizing temperature sensitive ferrofluids[31], [32] and time varying magnetization to achieve the required flow manipulation[33], [34].

Numerical studies of fluid flow through pipe and channel bends have revealed that the flow through them can generate secondary motion superposed on the primary one due to the presence of centrifugal forces and the walls. The flow can further become complex depending upon the flow regime (laminar, transitional or turbulent) and can form vortices depending upon the geometry and flow Reynolds number[35].

Most investigations involving process intensification consider a system with two or more species, which would have different miscibility with each other. The role of process intensification here is to increase the inter-mixing of the species via tunable flow manipulation[36]. This would usually involve doping the flow with a nano-fluid which then can be controlled by external force.

In this work mixing enhancement is viewed differently, as only one species (i.e. the ferrofluid) is considered for self-mixing enhancement. The mixing is characterized in terms of velocity based mixing scalars, and the dependence of mixing on Reynolds number is also investigated.

In contrast there have been many research investigations, both experimental and computational, studying the effects of ferrofluid flow for cooling of electronics and thermomagnetic pumping[37]–[40], where researchers have created self-sustaining pumping

action utilizing the temperature and magnetic field dependence of the magnetization of ferrofluids[41].

Heat transfer enhancement through a 90° elbow channel has been studied before[42]. Current research is an extension of the previous studies, in which two current carrying wires are introduced to produce a spatially non-uniform magnetic field. Additionally, the wires are allowed an angular degree of freedom, to create further heat transfer enhancement.

Chapter 2: Mixing Enhancement in an Elbow Channel

1. Introduction

Ferrofluid flow through a 90° elbow channel under the effects of non-uniform magnetic field has been studied previously through numerical simulation[42]. However, this previous study does not shed light on how the ferrofluid gets magnetized, on the collinearity/non-collinearity of magnetization, and on the magnitude of the applied magnetic field. Furthermore, the previous calculations, through use of an arbitrary magnetic number to describe the magnetization of the fluid does not consider the direction of magnetization, which is the bulk representation of the alignment of magnetic dipoles after a magnetic field is applied. Finally, the effects studied in most of the previous articles consider flow manipulation of ferrofluids as secondary, while focusing on heat transfer enhancement, mixing enhancement, etc. which includes additional physics or additional species in the flow.

In this chapter, the flow of a ferrofluid through a 90° elbow channel, where the ferrofluid is pre-magnetized in the direction of the inlet flow, under the influence of an external magnetization circuit is presented. Also, a spatially non-uniform magnetic field is applied to the elbow by means of two current carrying conductors, placed parametrically along a radial line passing through the center of the bend. The non-collinearity in the direction of magnetization of the ferrofluid and the applied non-uniform magnetic field is accounted for in the governing equations. Additionally, a resultant magnetization is introduced with a component of the external applied magnetic field in the flow direction, because of the boundary condition on magnetization. This formulation results naturally into another body force term, known as an enhanced viscosity[12], [43], [44]. Moreover, the primary effects of ferrofluid flow manipulation by a

parametrized non-uniform magnetic field are presented. Hence, secondary physics for example 2-species mixing, heat transfer, etc. is not considered, in order to simplify the analysis. In section 2 the problem geometry and ferrofluid properties are discussed, while section 3 discusses the governing equations and numerical formulation, and section 4 presents results and discussion.

2. Model Geometry and Ferrofluid Properties

2.1 Geometry

Figures 1-3 show the geometrical construction of the problem. In **Figure 1** the outer domain and the 90° elbow channel are shown. The outer domain is kept sufficiently large in order for the magnetic field generated by the two wires to attain convergence. The domain boundaries have magnetic insulation (Neuman) boundary conditions.

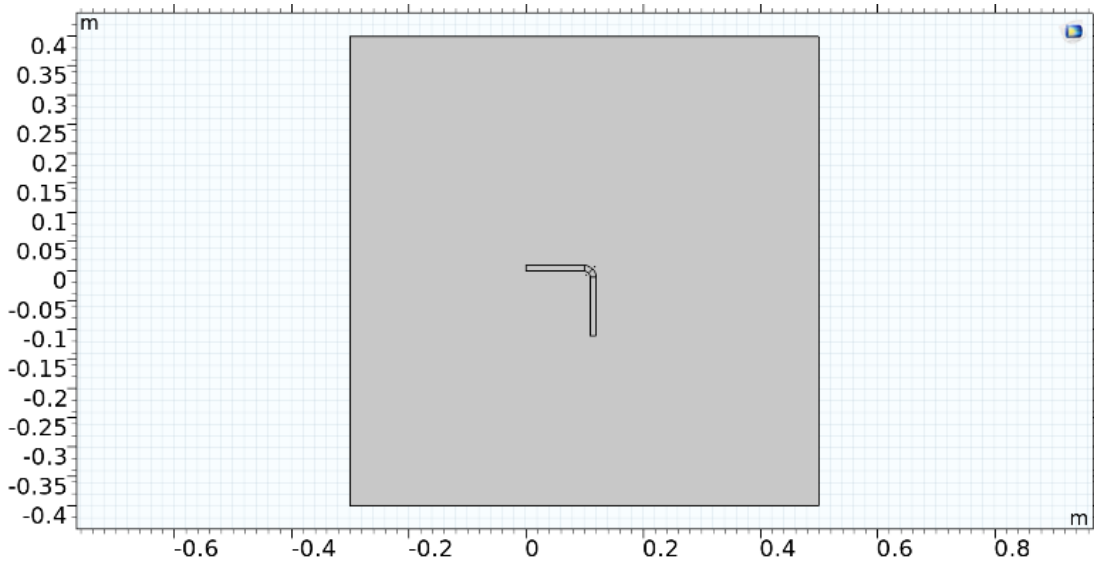


Figure 1 Zoomed out view of the problem geometry

Figure 2 shows a zoomed-in view of the elbow. The whole channel is comprised of two straight channels at the entrance and exit of the bend. The length of these channels is L_0 , which is set to 10 channel widths, giving hydrodynamically fully developed flow ($Re < 50$ here) before it enters the bend.

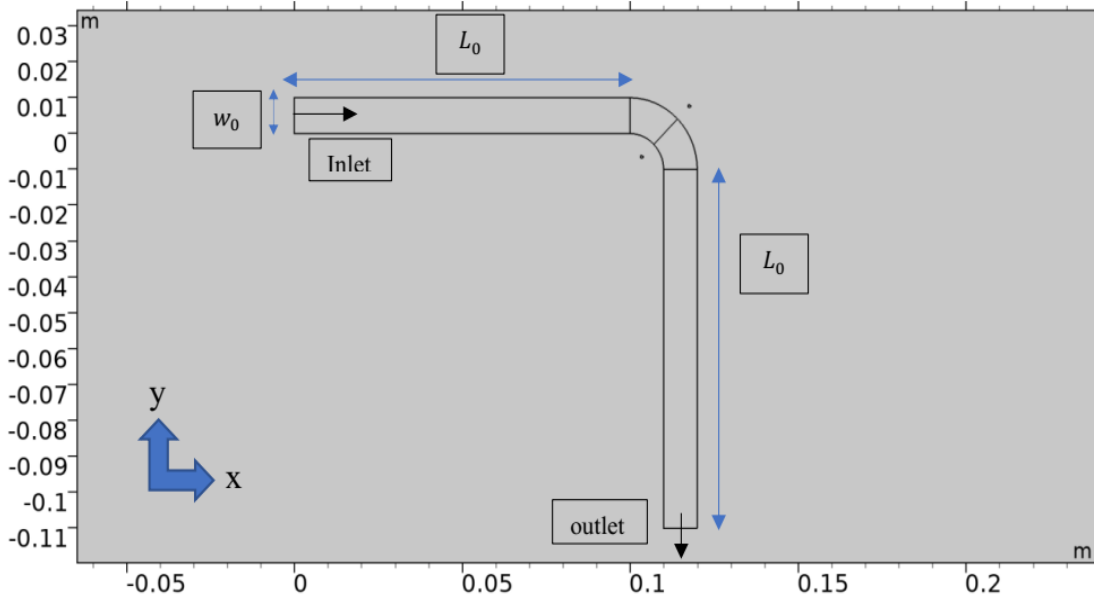


Figure 2 Schematic view of elbow channel and external wires

Figure 3 shows the placement of the wires with respect to the bend, and the channel center. We have identified three locations in the bend as Locations 1, 2 & 3 as marked in **Figure 3**, which will be utilized in the coming sections to analyze the mixing in the channel.

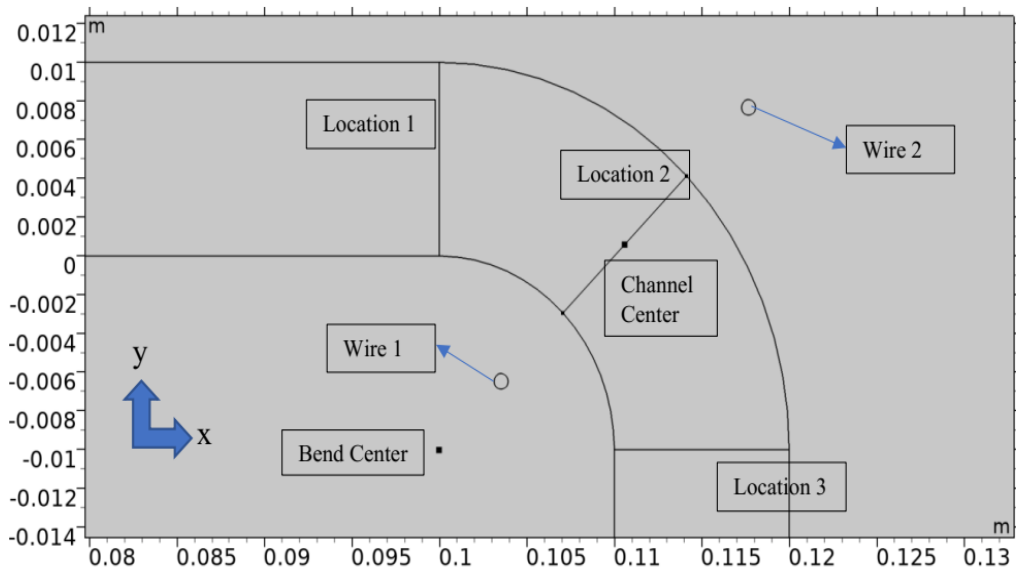


Figure 3 Channel bend with the two current carrying conductors

Locations 1 and 3 are at the entrance and the exit of the bend respectively, while location 2 is at the intersection of the bend centerline and the radial line containing the two wires as shown. Figure 3 also depicts the center of the bend which is 2 channel widths from the outer arc of the channel. Hence the inner arc is at a distance of w_0 (i.e. the channel width), from the bend center location.

In **Figure 3** the current carrying wires are along a radial line passing through the center of the bend and the distance between their centers and the channel center is equal to the width of the channel i.e. w_0 . This ensures geometrical symmetry in the domain. The wires can carry current in either direction, that is into the plane or out of the plane. **Figure 4** shows the meshing of the full domain, where the outer parts of the domain away from the channel and the wires is meshed coarsely, so as to conserve required computing power.

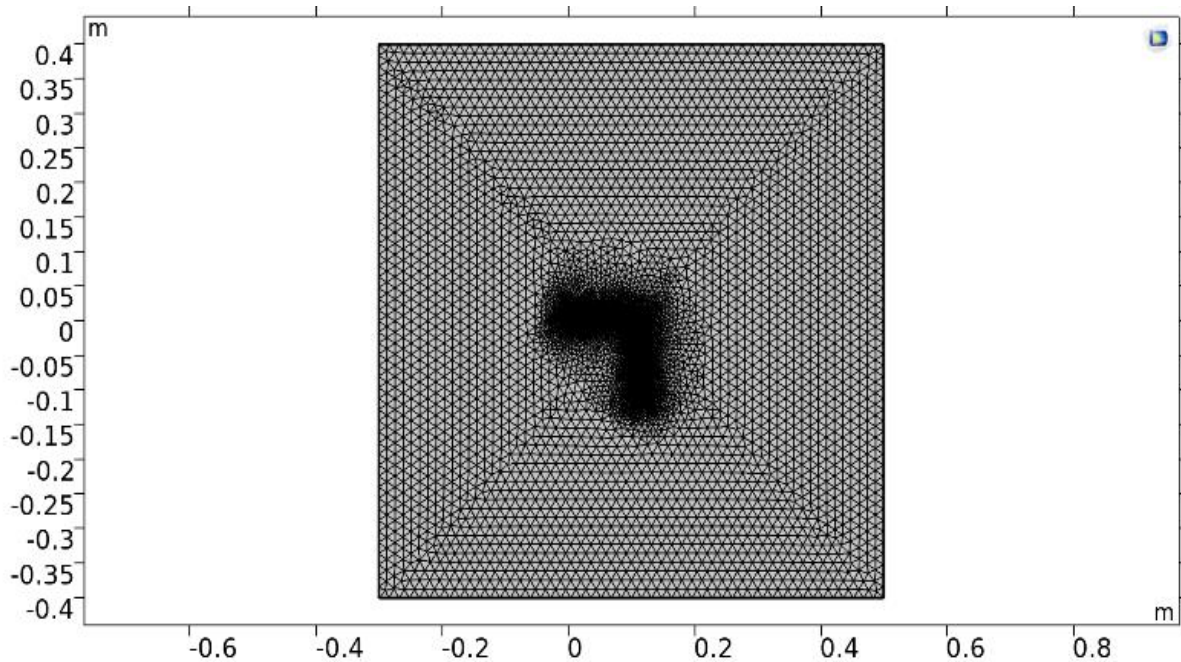


Figure 4 Mesh of the whole domain

Figure 5 shows the meshing in the bend region, which is obtained through a distribution of elements on the boundary of the channel. One parameter that controls the mesh size and the distribution is N_{cell} and is used in grid convergence studies.

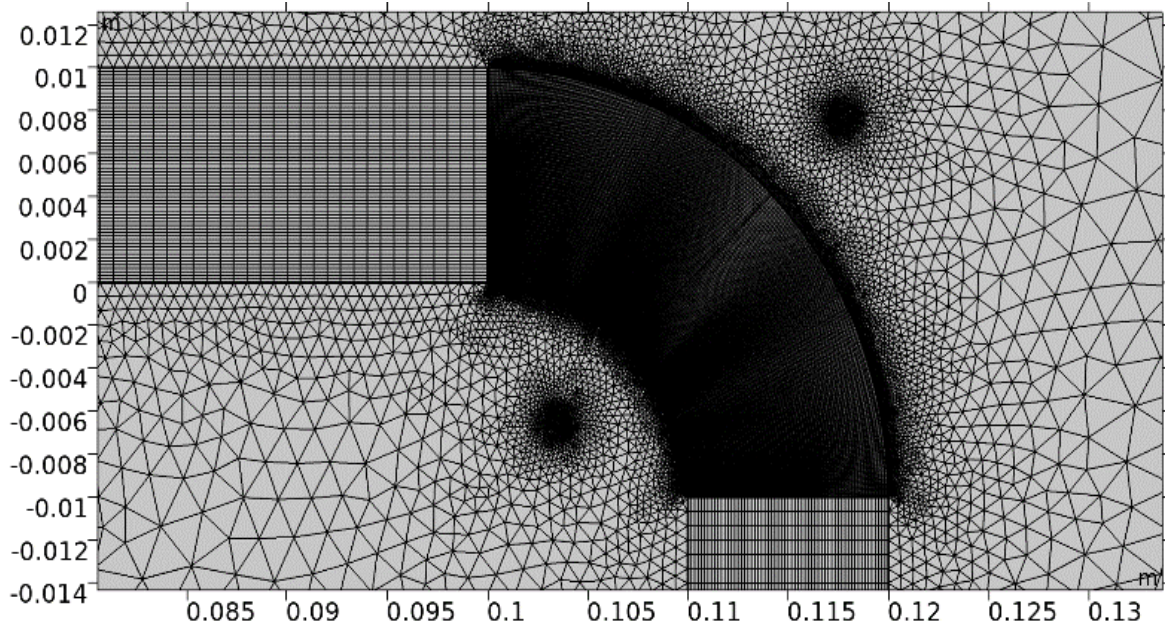


Figure 5 Structured mesh in the channel

2.2 Ferrofluid Properties

The properties used for this study are of ferrofluid EFH3 manufactured by Ferrotec corporation[45] and are listed in **Table 1**. It is assumed that:

- (i) the ferrofluid is electrically non-conductive,
- (ii) the properties of the ferrofluid are independent of magnetic field strength, and
- (iii) the properties remain constant.

Another assumption is that the problem is one-way coupled with respect to the magnetic field, i.e. the magnetic field emanating from the wires will influence the flow field, however, the flow field and the magnetized ferrofluid will not influence the current and flux generated by the

wires. The Lorentz force is also assumed insignificant for the analysis and the flow is assumed to be isothermal.

Table 1 Ferrofluid property data

Property	Value
Viscosity	12 [mPa.s]
Density	1420 [kg/m ³]
Magnetic susceptibility	3.52
Saturation magnetization	65 [mT]

3. Governing Equations

In this section we will discuss, the governing equations for the flow, and the numerical procedures used to solve the equations.

3.1 Governing Equations

The flow of the ferrofluid through the channel is governed by the Navier-Stokes equations. The equations considered here are from Odenbach[12] and Shilomis[43]. The flow is assumed to be incompressible and steady, and the fluid is assumed to be Newtonian. The following are the continuity and momentum equations used:

$$\nabla \cdot \vec{V} = 0 \quad (1)$$

$$\rho(\vec{V} \cdot \nabla \vec{V}) = -\nabla p + \eta \nabla^2 \vec{V} + \vec{M} \cdot (\nabla \vec{H}) + \frac{1}{2} \nabla \times (\vec{M} \times \vec{H}) \quad (2)$$

In the momentum equation the first term signifies advection, the second term the gradient of pressure, the third term the viscous dissipation, the fourth term is the Kelvin Body Force (KBF), and the fifth term arises from the non-collinearity of the magnetization and magnetic field. The fifth term can be expanded using vector calculus as:

$$\nabla \times (\vec{M} \times \vec{H}) = \vec{M}(\nabla \cdot \vec{H}) - \vec{H}(\nabla \cdot \vec{M}) + (\vec{H} \cdot \nabla)\vec{M} - (\vec{M} \cdot \nabla)\vec{H} \quad (3)$$

In order to close the system of equations, equations related to the conservation laws for magnetic field are introduced. Since the ferrofluid is assumed to be non-conducting, and the relationship between magnetization and the magnetic field is linear, we have the following equations:

$$\nabla \times \vec{H} = 0 \quad (4)$$

$$\vec{M} = \chi_m \vec{H} \quad (5)$$

The ferrofluid entering the channel is assumed to be pre-magnetized in the flow direction, and hence the magnetization, M_s , has a fixed direction in the curvilinear coordinate along the length of the channel. This magnetization magnitude is affected as the ferrofluid is influenced by the external magnetic field, which is much smaller in magnitude compared to the set magnetization values we have used in the study. Hence, it is reasonable to assume that the direction of bulk magnetization essentially remains constant, but to account for this external influence on the magnitude a component of the induced magnetization along the curvilinear coordinate is added to the magnetization as:

$$|\vec{M}_s| = (\vec{M}_s + \chi_m \vec{H}) \cdot \hat{e}_1 \quad (6)$$

where \hat{e}_1 is the curvilinear coordinate along the direction of the channel. Since the direction of the \vec{H} and \vec{M} fields are not the same, the fifth term in the N-S equation is non-zero in this study. To analyze the (self)-mixing of the ferrofluid we have introduced three different mixing scalars (or velocity intensification factors) based in velocity. The phenomenon of mixing is usually quantified in terms of mixing efficiency when more than one species mixes with each other. However, in this study, since the flow of a single fluid is studied, the scalars formulated here to map the non-uniform structures in the flow must be rooted in the velocity of the flow. They are formulated as follows:

$$N_{mix} = \frac{\int ((\vec{V})-U)^2 dA}{\int U^2 dA} \quad (7)$$

The mixing number as given by equation 7 is a scalar based on the square of the difference between the local and inlet velocities, normalized by the integration of the square of the inlet velocity, over an appropriate area. In our case the area used is the cross-sectional area of the bend. This quantification of the mixing is rooted in the ratio of areal averages of the difference and the baseline velocities. The baseline velocity has been defined to be the inlet velocity U for all the mixing scalars. The first mixing scalar is very similar to the mixing number, but the integration is over a radial line for this case, rather than an area. It is given as[46]:

$$N_{mix1} = \frac{\int ((\vec{V})-U)^2 dl}{\int U^2 dl} \quad (8)$$

This scalar has been analyzed at three locations in the channel, as shown in figure 3. Hence the integration is over the width of the channel along a radial line. The second mixing scalar is similar to the first mixing scalar, with respect to the integration over channel width, however the integrand is the individual squared components of the velocity differences. It is given as:

$$N_{mix2} = \frac{1}{2} \left[\left(\frac{\int \sqrt{(u-U \hat{n}_x)^2} dl}{\int U dl} \right)^2 + \left(\frac{\int \sqrt{(v-U \hat{n}_y)^2} dl}{\int U dl} \right)^2 \right] \quad (9)$$

Equation 10 defines the flow Reynolds number using the channel width as the length scale of the problem.

$$Re = \frac{U w_0}{\eta} \quad (10)$$

3.2 Details of Numerical Modeling

COMSOL Multiphysics version 5.4 is used for numerically simulating the set of governing equations discussed in the previous section[47]. COMSOL is Finite Element based software which

solves conservation laws using the weak form and weighting functions of specified order. The internal multiphysics interface to couple magnetic and flow fields is utilized. Additionally, we have used curvilinear coordinates to define the magnetization of the ferrofluid. The magnetic field generated by the current carrying conductors is the non-uniform magnetic field, and its component in the direction of the flow is used to obtain resultant magnetization. Second order elements for both pressure and velocity fields while discretizing the problem are used. The magnetic field is discretized with quadratic elements as well.

Since the inlet velocity is uniform it can be expressed in terms of the Reynolds number. The solution procedure uses the fully coupled non-linear finite element[48] method. The whole mass matrix is solved directly using the PARDISO non-linear solver with the tolerance on the solution and relative residual error set to 10^{-5} ensuring tight convergence. **Table 2** lists the parameters that are varied along with their limits.

The negative and positive values for the current accounts for the bidirectionality of the current flow (into [-] and out of [+] the plane). The simulations consider 4 current flow direction combinations, as listed in **Table 3**. This offers a new perspective as to how flow manipulation can take place simply by reversing the current flow direction.

Table 2 Parameters and their variation limits

Parameter	Limits
Current (I)	0 to 6 [A]
Magnetization (M)	10000 to 50000 [A/m]
Reynolds Number (Re)	5 to 50

The symmetric cases (cases 1 & 4) have the current flowing in the same direction in both the wires, whereas the anti-symmetric cases are (cases 2 & 3) have the current flowing in opposite directions.

Table 3 Current Direction and cases

Case	Wire 1	Wire 2
1	Into the plane [-]	Into the plane [-]
2	Into the plane [-]	Out of the plane [+]
3	Out of the plane [+]	Into the plane [-]
4	Out of the plane [+]	Out of the plane [+]

Grid convergence studies were performed, taking extreme cases with magnetization of 50000 A/m and current of 6A, and by varying the Reynolds number from 5 to 50. The mesh generation parameter N_{cell} was varied from 50 to 100 and it was found that the pressure drop across the channel incrementally decreases as N_{cell} increases. The value of $N_{cell} = 100$ was chosen for the simulations, as the relative error in pressure drop calculated between $N_{cell} = 90$ and 100 is small (i.e. less than 3%). **Figure 6** shows the relative error (as compared to preceding N_{cell} value) in pressure drop calculation in the channel for the grid convergence study. Both the cases of same and opposite current direction for five N_{cell} values over the whole Reynolds number range are plotted. For all cases the difference between the simulated pressure drop for $N_{cell} = 90$ & 100 are small.

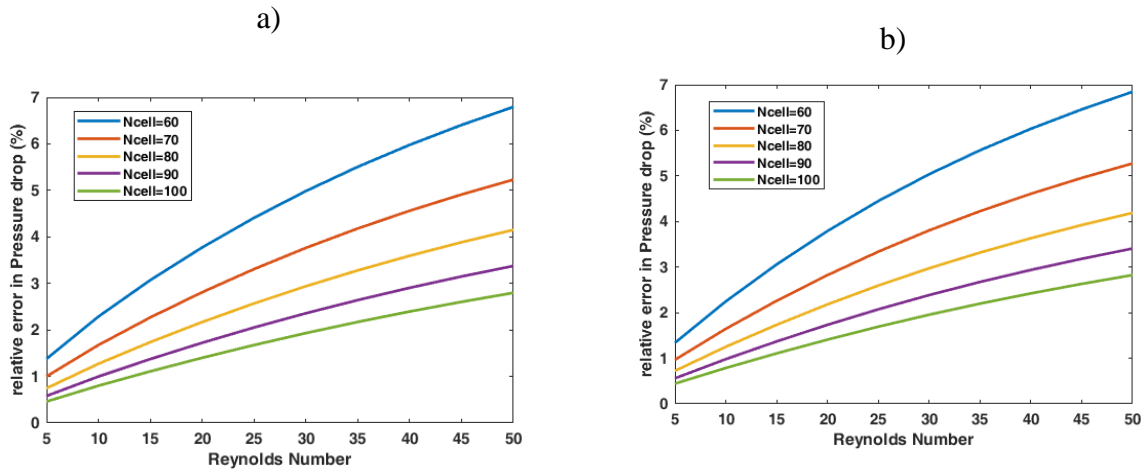


Figure 6 Grid convergence for I = 6A. a) case 4, b) case 3

4. Results and Discussions

Figure 7 shows the obtained magnetic flux density norm (i.e. the magnitude of the B field) for symmetric (case 1) and anti-symmetric (case 2) cases. It is to be noted that when the current flows in opposite direction the magnetic flux density in the channel is intensified, while the opposite is true for the symmetric current direction case. This variation in the magnetic flux density and by extension the magnetic field (H) between the two cases, will produce different results with respect to the mixing as quantified by the three mixing scalars introduced. It must be noted that the mixing phenomenon observed in **Figure 8** is different from the usual mixing that is associated with the mixing of two or more species together. Such mixing phenomenon is tracked through mixing efficiencies, etc., which are based in the concentration of individual species.

Secondly, the vortical (self)-mixing observed here is a large-scale phenomenon, as indicated by the significant size of the flow structure.

Finally, in order to quantify and further study this mixing phenomenon, the non-dimensional numbers or scalars introduced earlier are calculated. These scalars look like scalars used to quantify turbulent flows but are really a measure of flow velocity non-uniformity, since the flows we are considering here are steady and laminar. The non-uniform flow structure which we term as ‘vortical (self)-mixing’ is due to the magnetic energy applied on the ferrofluid by the virtue of its initial magnetization and the non-uniform magnetic field applied by the wires.

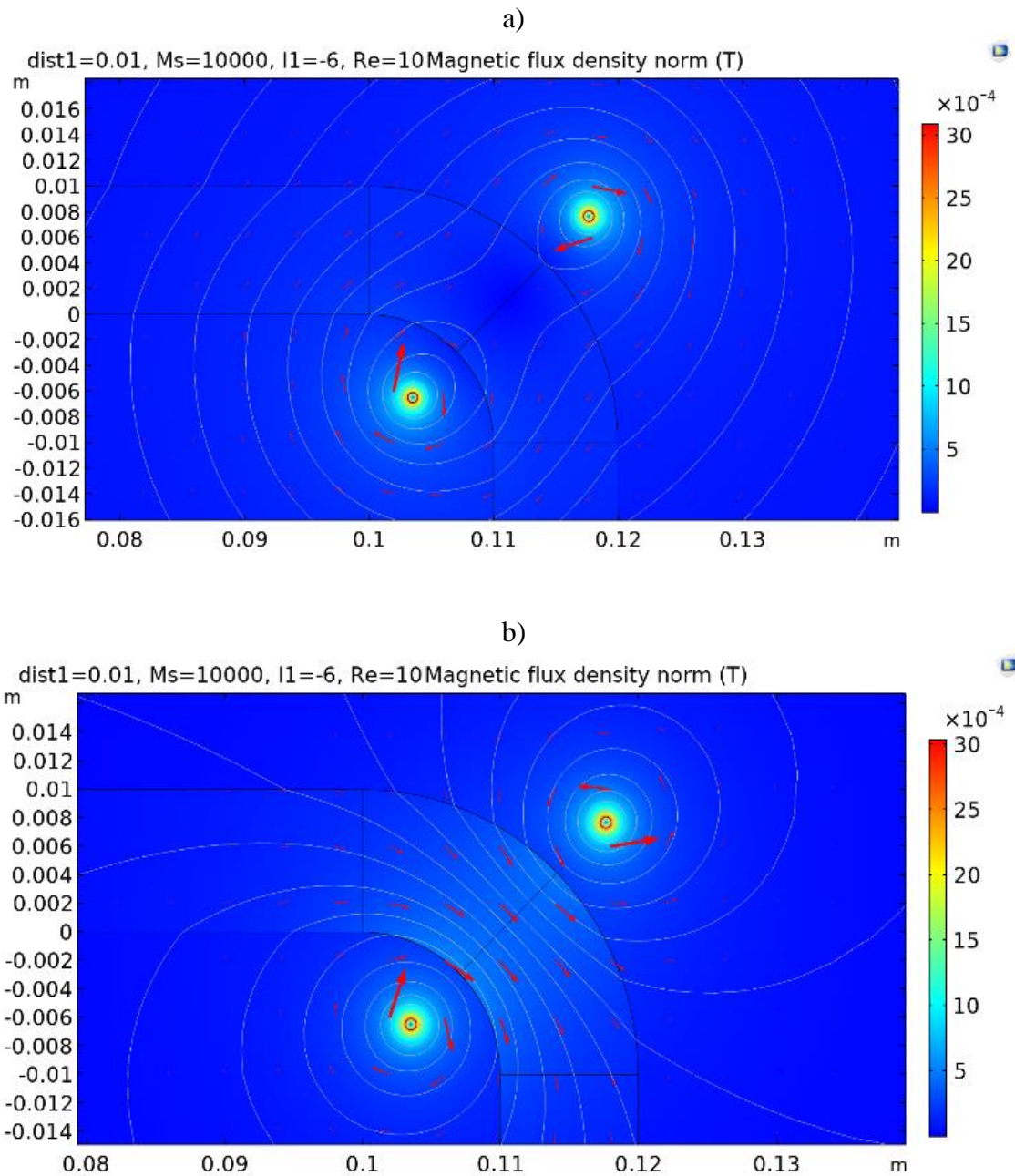


Figure 7 Magnetic Flux density norm for $I=6A$. Top plot - case 1, Bottom plot - case 2

In **Figure 8**, the velocity magnitude for two such cases (3 & 4), where the parameters are the same, except for the direction of the current flows. The Reynolds number is 15, magnetization is 50000 A/m and the current magnitude is 6 A. In both the cases it is seen that the magnetic fields

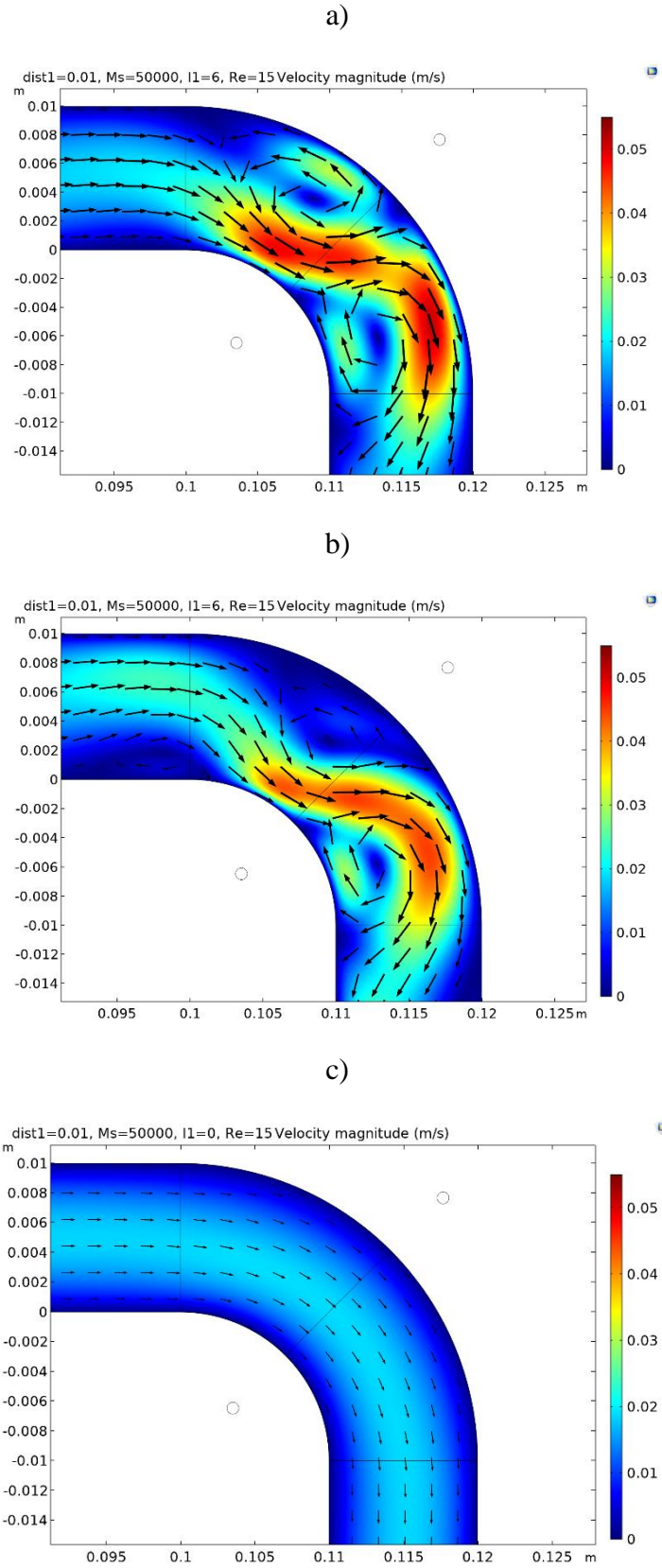


Figure 8 Velocity magnitude plot for $I = 6A$ for a) case 4, b) case 3, and c) no current

and the initial magnetization of the ferrofluid create a vortical structure in the bulk flow. These structures resemble the formation of wakes behind a bluff body [9].

It is observed that the rotation of the ferrofluid structure is almost symmetric for case 4, whereas the structure tends to travel downstream for case 3. This would give different results for the line integration based mixing scalars.

In order to maintain comparative consistency, the velocity magnitude lies between 0 and 0.055 m/s for all the plots shown in **Figure 8**. **Figure 9** shows the velocity flow field for current flow cases 2 & 1.

There is clear difference between these two cases, where in case 1 the highest velocity magnitude is higher than that for case 2.

It is observed that the rotation and direction of the structure for cases 1 & 2 are reversed from those for cases 3 & 4. For case 2 the rotation is more pronounced in the first half of the bend, whereas it was found to be more pronounced in the second half of the bend for case 3. This shows that not only can there be enhancement in the vortical (self)-mixing, there can be domain specific excitation of the ferrofluid, that can give higher and lower swirling in the two portions of the bend. Furthermore, the magnitude of the current is always maintained to be equal for all the cases in this study. The preferential rotation as seen here by changing the direction of the current can also be manifested when the current magnitudes in the two wires are unequal.

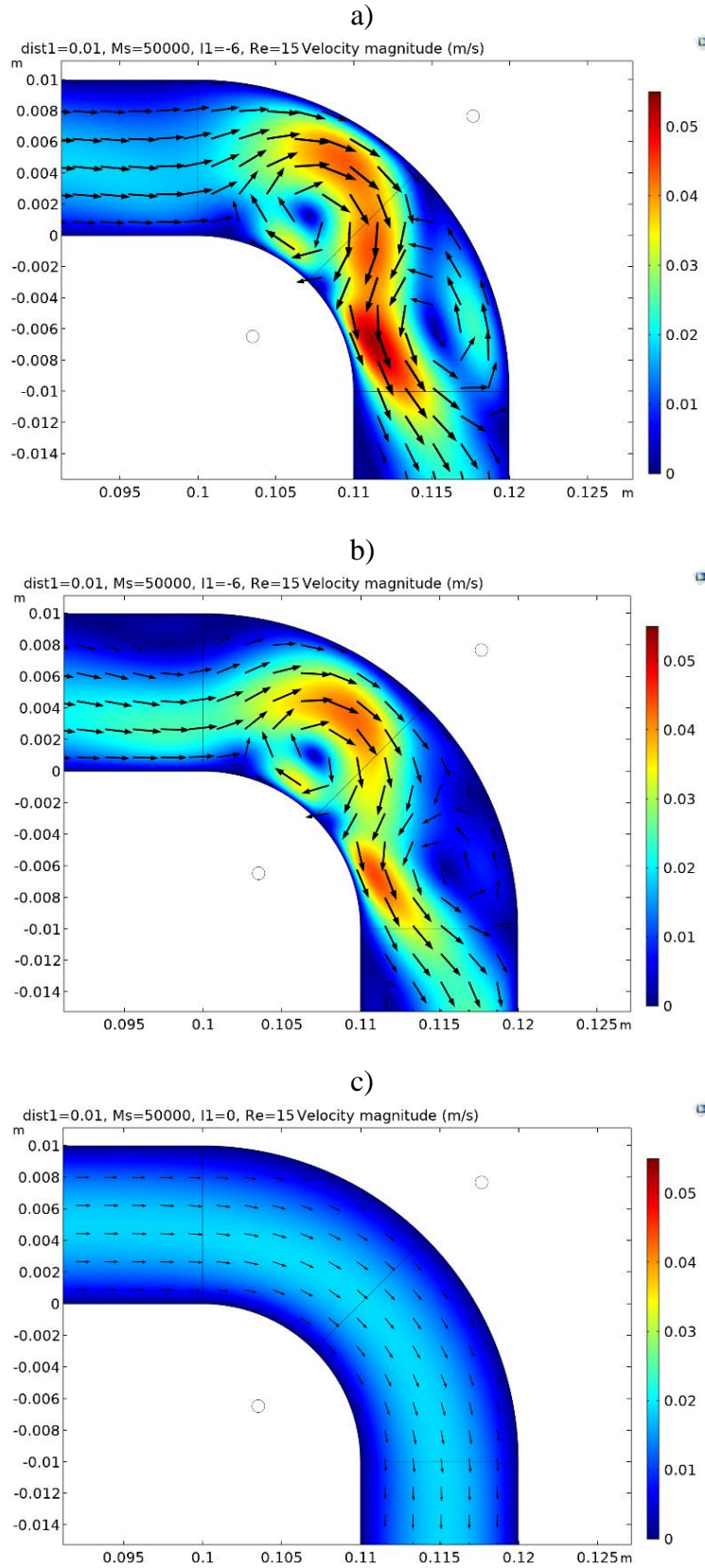


Figure 9 Velocity magnitude plot for $I = 6$ A for a) case 1, b) case 2, and c) no current

4.1 Comparison of mixing for the two cases

This subsection is dedicated for the analysis and comparison of the two mixing scalars and mixing number formulated in section 3 for the four cases defined in table 3, while varying the magnetization magnitude and Reynold number.

4.1.1 Comparison Utilizing Mixing Number

Figure 10 shows the comparison of mixing number integrated over the area of the bend. The two cases are plotted on two y axes with the left y axis defining the antisymmetric current direction cases (case 2&3), and the right y axis the symmetric current direction cases (case 1&4). It is observed that, for all four cases, the mixing numbers are slightly higher when the current is flowing out of the plane in wire 1, (for case 3 & 4) than when it is flowing into the plane in wire 1 (for case 1 & 2). This can be attributed to the curvature of the elbow which is oriented in the clockwise direction. Secondly, the mixing numbers for symmetric current cases (i.e. case 1 & 4) are much higher than for the antisymmetric cases. The highest mixing number achieved is 34 for case 4 when $I = 6$ A, $Re = 5$ and $M_s = 50000$ A/m. However, it is 23.5 for case 3 at the same conditions. Finally, it is observed that the mixing number goes to zero for higher Reynolds number values. The reduction in mixing is much quicker for lower magnetization values, but as the magnetization increases the mixing enhancement occurs till Reynolds number as high as 20, for $M_s = 50000$ A/m. However, the mixing reduces very quickly for $M_s = 10000$ A/m. Since, the mixing number is a scalar based in areal average of velocity intensity, it does not explain and quantify the differential vortical structures observed in figures 8 and 9. Hence, a deeper look into mixing is conducted by using the mixing scalars based in lineal averages, at different locations in the bend.

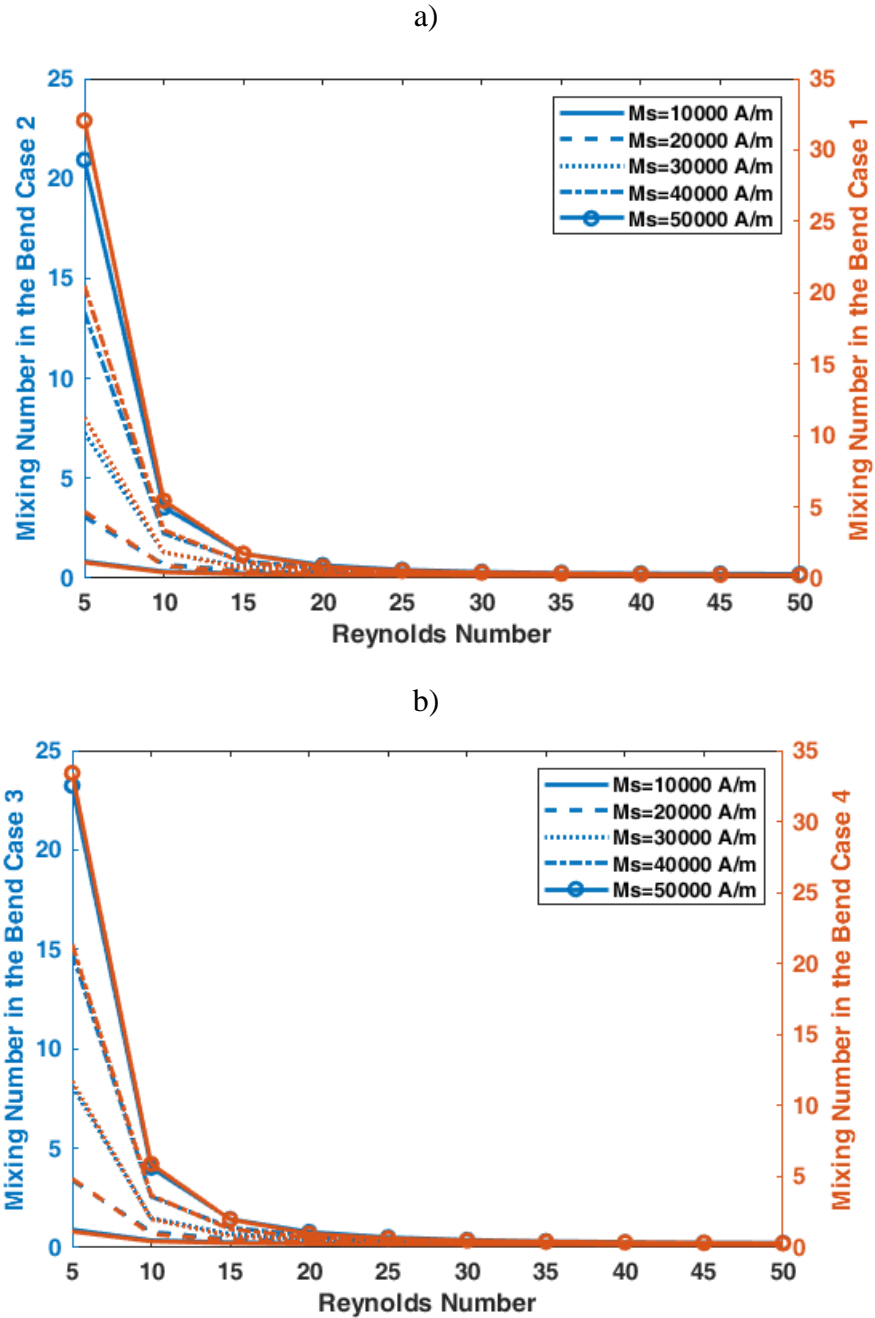


Figure 10 Mixing number in the bend for $I=6$ A a) case 2&1 and b) case 3&4

4.1.2 Comparison Utilizing Mixing Scalar 1

The vortical structures shown in **Figure 8** & **Figure 9** show some clear local features, which can be quantified by line integral scalar quantities. Mixing scalar 1, as given by equation 8 is evaluated at three locations in the elbow. Figure 11 shows mixing scalar1 as a function of

Reynolds number for the four current direction cases, with $I = 6A$, and for different ferrofluid magnetizations. These figures are plotted with two y axes so that two current direction cases can be compared. The sub figures a) and b) are for location 1 (i.e. at the inlet of the elbow), and a) is for cases 1 & 2 and b) is for cases 3&4. Similarly, the sub figures c) and d) are for location 2, and e) and f) for location 3.

At low Reynolds number values, the mixing scalar is very high, because of the larger residence time in the domain, and lower inertia, as seen previously with mixing number. It is observed that for cases 2&3 (anti-symmetric) the values of the mixing scalar 1 at location 1 is higher than those for cases 1&4 (symmetric). This means that the disturbances in the flow start sooner upstream for the anti-symmetric case than for the symmetric case. Also, case 4 has higher mixing scalar 1 values at location 1 as compared to case 1, which may be due to the bend structure and flow direction.

Further, when comparing mixing scalar 1 at location 2 the most interesting observation is between cases 2 & 3, where mixing scalar1 values for case 3 are almost double those for case 2. This observation can be confirmed from the velocity magnitude plot in figures 8 and 9, where the velocity magnitudes for case2 at the centerline are much lower as compared to those seen in case 3. This is very critical because this phenomenon can be utilized to control mixing differentially as needed, in zones which are prone to the highest gradients in the applied magnetic field. Moreover, mixing scalar 1 evaluated at location 3 is higher in magnitude for both symmetric cases 1 and 4 as compared to the anti-symmetric cases 2 &3. Secondly, for case 3 mixing scalar 1 is smaller than those observed for case 2, which is confirmed from observations from figs 8 & 9, where higher velocity magnitudes are seen in the second half of the bend for case 2, nearer to location 3. Finally,

the magnitude of the scalar is much higher at location 3 than it is at location 1 for all the cases. This observation might be useful for mixing enhancement in two species systems.

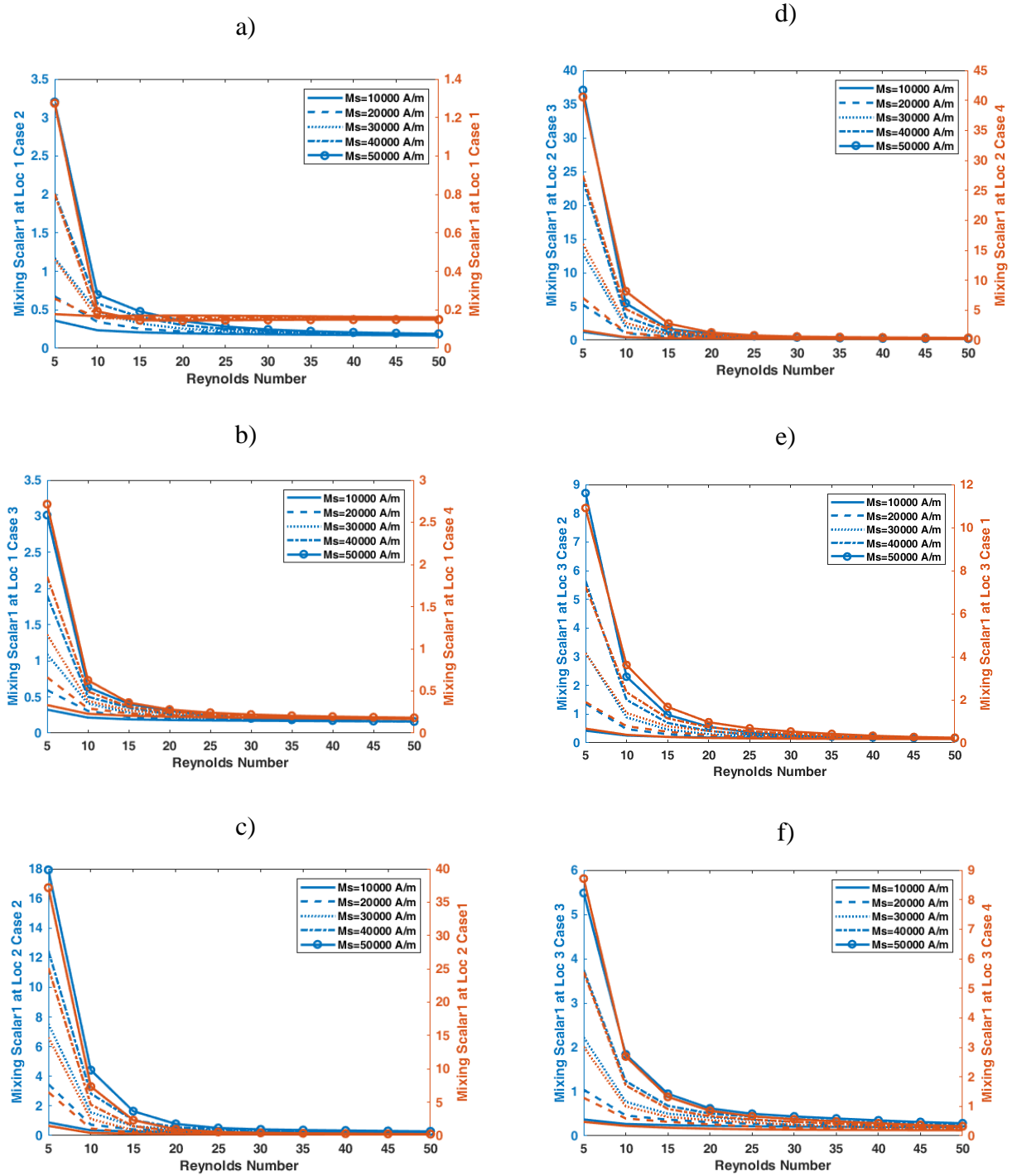


Figure 11 Mixing scalar 1 for same & opposite current cases a) Location 1 case 1&2, b) Location 1 case 3&4, c) Location 2 case 1&2, d) Location 2 case 3&4, e) Location 3 case 1&2 and f) Location 3 case 3&4

4.1.3 Comparison Utilizing Mixing Scalar 2

Mixing scalar 2, as given by equation 9 is evaluated at three locations in the elbow. **Figure 12** shows mixing scalar 2 as a function of Reynolds number for the four current direction cases, with $I = 6A$, and for different ferrofluid magnetizations.

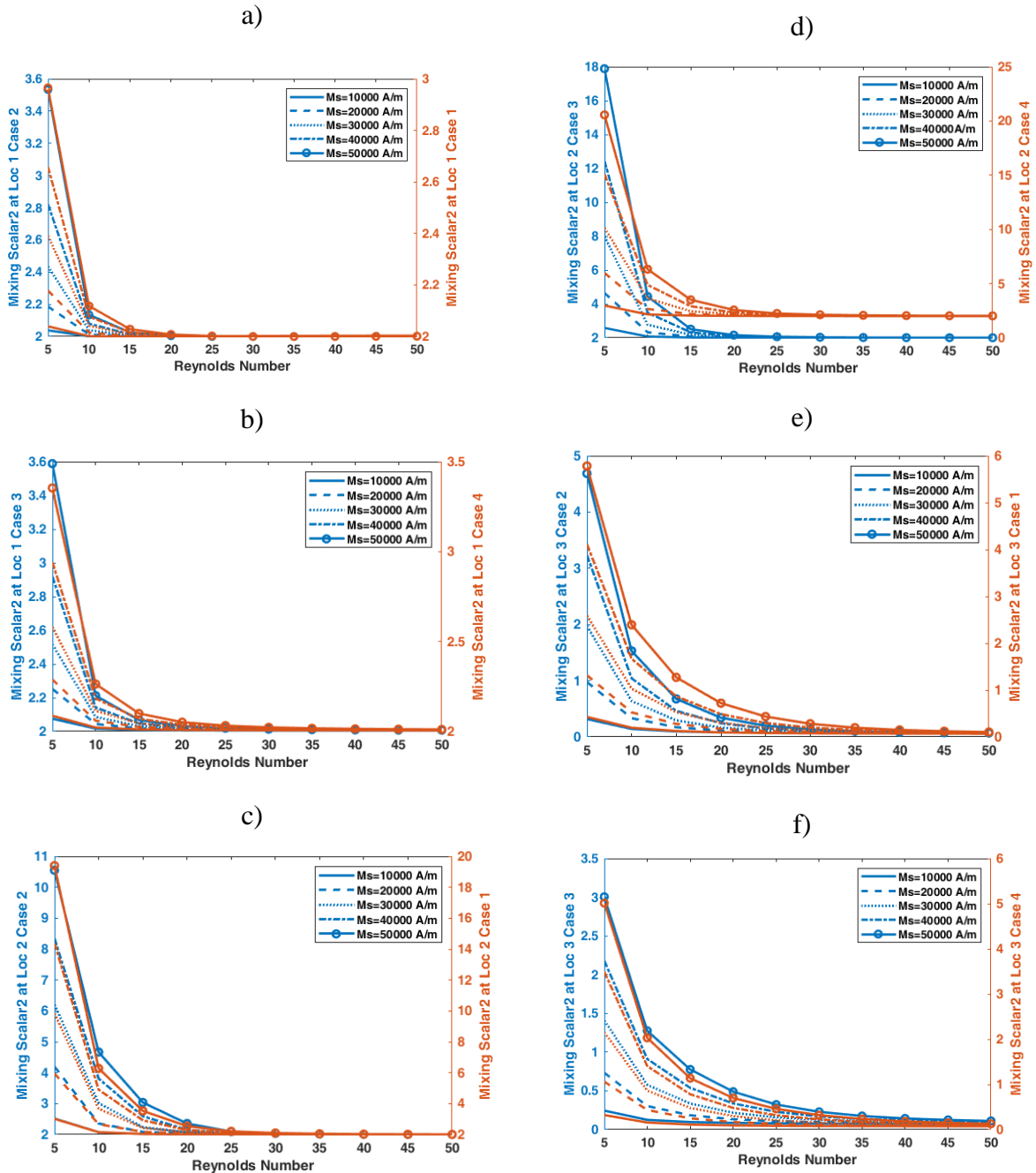


Figure 12 Mixing scalar 2 for $I=6A$ for a) Location 1 case 1&2, b) Location 1 case 3&4, c) Location 2 case 1&2, d) Location 2 case 3&4, e) Location 3 case 1&2 and f) Location 3 case 3&4

Again, two y axes plots are used. The sub figures a) and b) are for location 1 (i.e. at the inlet to the elbow) and a) is for cases 1 & 2 and b) is for cases 3&4. Similarly, the sub figures c) and d) are for location 2 and e) and f) for location 3.

From equation 9 the mixing scalar can be defined as the summation of normalized kinetic energy scalar obtained for each case. In essence, it is the excess kinetic energy at a location. This kinetic energy is however different from the absolute kinetic energy of the flow, as the individual velocities considered are normalized velocity scalars of the difference above the velocity scale U .

Although the magnitude of mixing scalar 2 is different than that of mixing scalar 1, similar trends are observed. At location 1 mixing scalar 2 for cases 1 & 4 (symmetric) is smaller as compared to cases 2 & 3 (anti-symmetric). At location 2 for cases 2 & 3, there is significant difference between the values of mixing scalar 2, as was similarly indicated when using mixing scalar 1. For mixing scalar 2 when comparing cases 2 & 3 it is observed that the magnitudes for case 2 are higher than those for case 3, as was also observed from mixing scalar 1 and seen in figs 8 & 9. Also, at location 3 case 1 and case 4 are of higher magnitude than case 2 & 3, which indicates that downstream mixing is more pronounced for symmetric cases than for anti-symmetric cases. This again can be useful for preferential mixing systems.

5. Conclusions

In this research ferrofluid flow in a 90° elbow channel is studied, under the influence of non-uniform magnetic fields generated by two current carrying conductors placed parametrically from the channel center. The ferrofluid was assumed to be magnetized in the curvilinear direction of the channel before entering the channel, and it is affected by the non-uniform magnetic field generated by two wires near the bend. In the governing equations, included is a new term arising from the magnetics, apart from the Kelvin Body Force, which is due to the non-collinearity

between the ferrofluid magnetization and the applied magnetic field. To quantify the effects of the magnetic field on the vortical (self)-mixing of the ferrofluid, three velocity based mixing scalars were introduced, two of which used linear averages, and one used an areal average. It was observed that mixing can be enhanced significantly by the action of a non-uniform magnetic field, but this enhanced vortical (self)-mixing can only be sustained by higher ferrofluid magnetization and higher applied non-uniform magnetic field, which is directly proportional to the current flowing in the conductors (wires). The mixing scalars gave a picture of the mixing, with the mixing number based in area only providing information about total mixing action, whereas mixing scalars 1 and 2 provided information about how the mixing is concentrated at particular locations in the channel, which is more indicative of the differential mixing behavior seen from the velocity magnitude plots. The trends in the mixing scalar plots are identical for symmetric and anti-symmetric current direction cases, and for different current magnitudes flowing through the conductors. The mixing invariably decreases with increase in Reynolds number, which is expected, as with higher Reynolds number the fluid has higher inertia and less residence time in the channel. To quantify the vortical (self)-mixing adequately, one needs two mixing scalars, one which is an areal average like the mixing number, which gives bulk statistics about the flow, and the second a lineal mixing scalar like mixing scalars 1 and 2, which give local statistics about the flow. Furthermore, it is observed that preferential mixing can be induced into the system by changing the direction of the current, and possibly by flowing unequal currents in the two wires. Hence, this system is useful for flow configurations where controlled and spatially preferential mixing is required for contributing species. Finally, the non-collinearity of the magnetization and the magnetic field should also be looked at from the point of view of fluid rotation. Although in this study we have assumed that the magnetization remains unaltered in its direction, there can be systems or

ferrofluids where there can be internal dipole rotations due to fluid rotations, which would need additional accounting than what is produced in this work.

Chapter 3: Heat Transfer Enhancement in Elbow

Channels

1. Introduction

As discussed earlier, ferrofluids are used in a wide variety of systems for heat transfer or thermodynamic applications[49]. Heat transfer enhancement with externally controllable fluids is of special importance in electronics cooling[50]. There are a wide variety of studies performed for ferrofluid/nanofluid convection in enclosures with different types of heat sources. However, of late there has been much interest in self-pumping mechanisms and cooling through temperature sensitive ferrofluids[51]–[55]. In this chapter, a numerical analysis of heat transfer enhancement in a 90° elbow channel is presented. The analysis is performed on two different 90° elbows with outer radii of the bend equal to two and four channel widths. The ferrofluid flow inside the channel is controlled by a set of two parametrically placed wires, at a distance of 1 channel width from the center of the channel. These wires are allowed to carry current either into the plane or out of the plane and can have different magnitudes as well. The non-uniform magnetic force generated by the wires will be responsible for exerting a Kelvin body force on the ferrofluid

Furthermore, the system is configured in such a way that it allows for cooling system design with an additional angular variable, which can be adjusted to change the cooling needs for the channel. This angular variable helps maintain the distance from the center point of the channel, while providing an extra degree of freedom to alter the magnetic field distribution inside the channel. The alteration of the magnetic field will be responsible for different flow behavior and thus may increase/decrease local or global cooling performance. The cooling performance is

characterized by a set of four Nusselt numbers, which characterize both local and global cooling performance of the system. In the next section the configuration of the system is described, in section 3 the governing equations along with the constitutive relations and thermophysical properties are discussed, section 4 provides the details of numerical modeling, section 5 presents the results of the numerical modeling, & section 6 summarizes the findings and draws conclusions.

2. System Configuration

Figure 13 and **Figure 14** represent the system configuration for the elbow channel with outer radius of 2 channel widths from the bend center point. The outer domain is kept sufficiently large as shown in **Figure 13**, which will allow for the convergence of magnetic field.

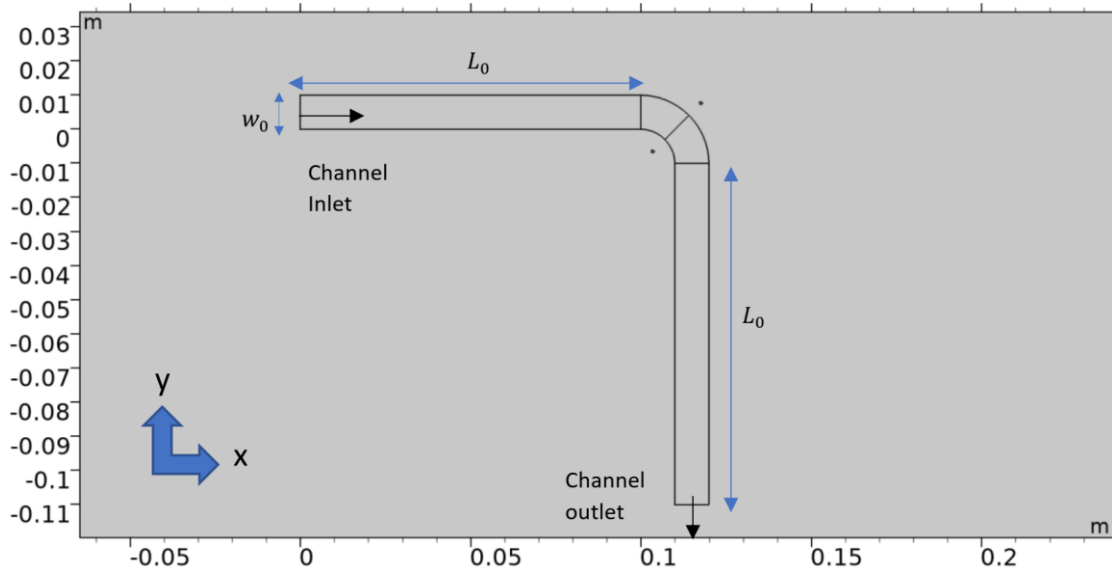


Figure 13 Configuration of the elbow channel

Similar to the configuration shown in the previous chapter, the lengths of the two channels before and after the bend is L_0 , which is set to 10 channel widths, giving leading to a hydrodynamically fully developed flow before it enters the bend. The wires can carry current in both the directions i.e. into and out of the plane. These cases are discussed in detail in section 4.

In **Figure 14** the parametric placement of the wires is shown along with the bend inlet, outlet and the bend center. The bend center is chosen such that it divides the bend and by extension the channel into two parts of equal area, separated by an angle of 45° .

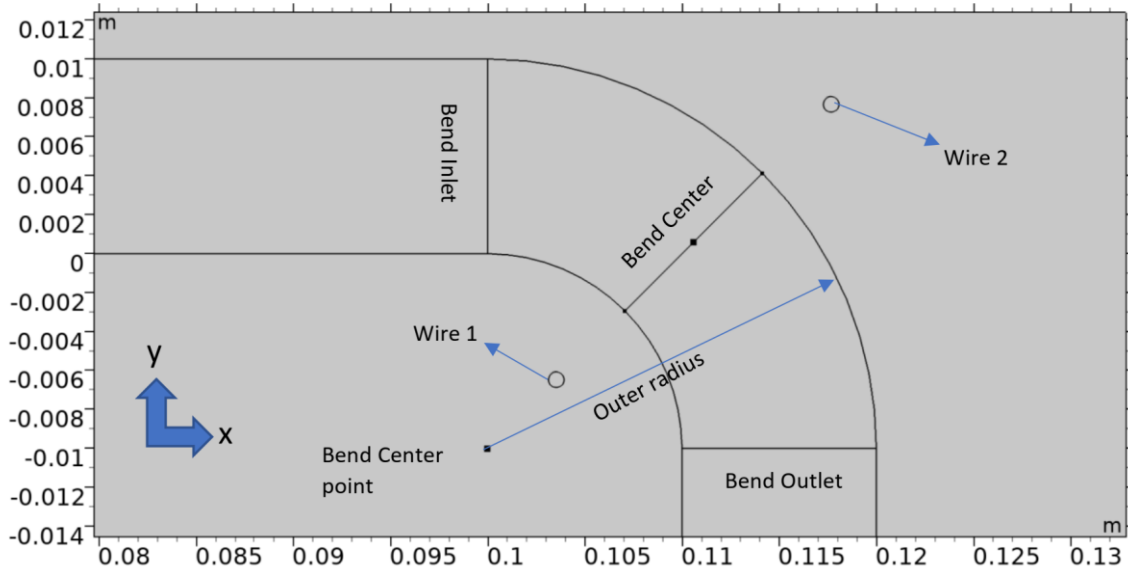


Figure 14 Elbow channel bend for outer radius of 2 channel widths

In this study two channels are studied. Both elbow channels undergo a 90° bend, however, differ from each other by the magnitude of the outer radius. The first channel has an outer radius of $2w_0$ while the second has an outer radius of $4w_0$. Another variation is within the angle which the line joining the two wires make with the horizontal. **Figure 15** shows the three different cases of symmetrical angular displacement of the wires with respect to both the channels centers.

The wires are always kept at a distance of $dist_1$ from the center of the bend and are given an angular displacement of $\alpha = 30^\circ, 45^\circ$ and 60° . The mesh generation is identical to what is shown in the previous chapter, and will be discussed with respect to grid convergence in section 4.

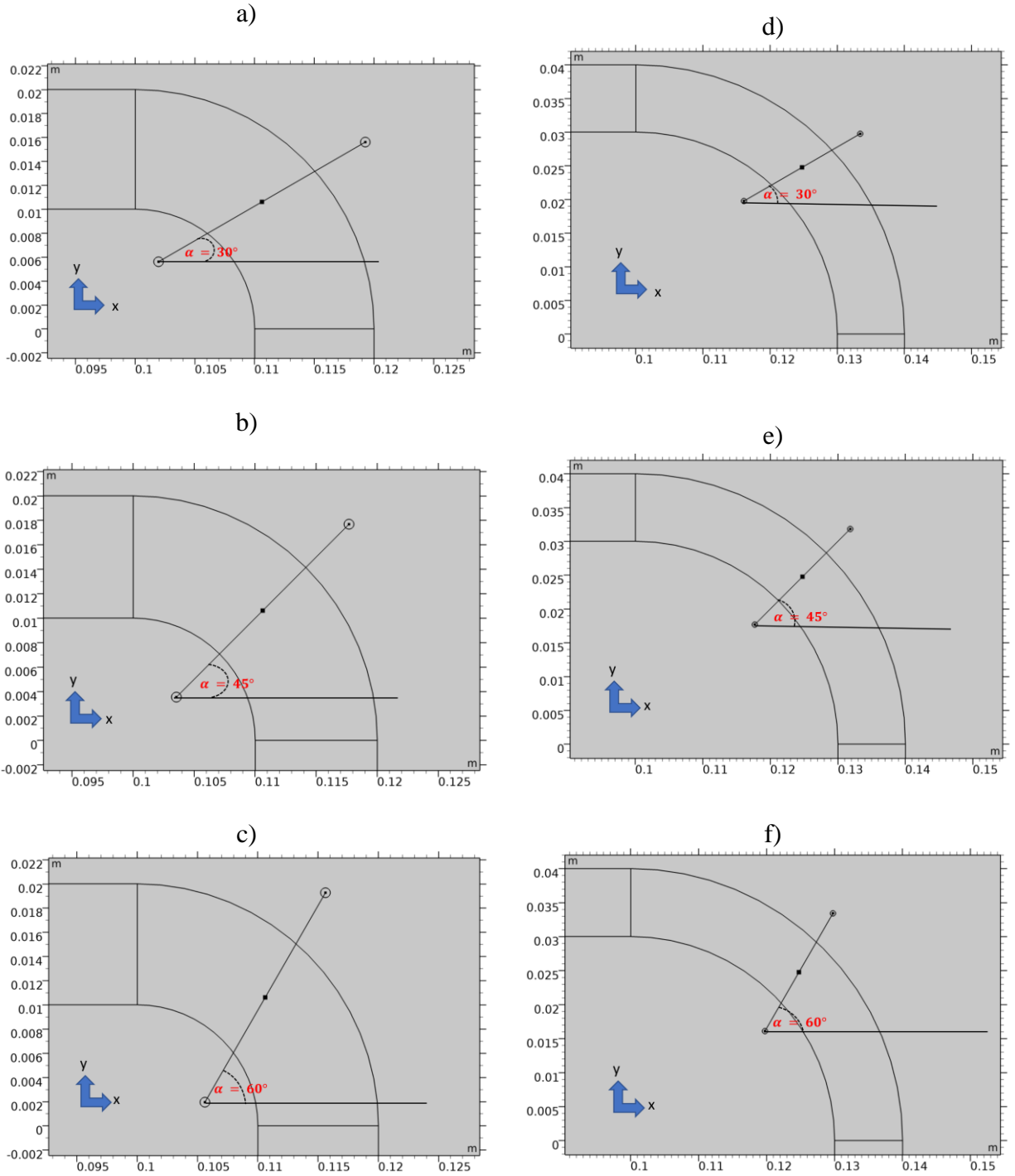


Figure 15 Angular position of the wires with respect to the horizontal for a),b) and c) outer radius of $2w_0$ and d),e) and f) outer radius of $4w_0$

3. Governing Equations

The general continuity, momentum and energy equations govern the ferrofluid flow through the channels. The following assumptions are made for the fluid and the flow:

- a.) The ferrofluid is linear, i.e. the magnetization is linearly related to the magnetic field strength
- b.) Ferrofluid is a Newtonian fluid
- c.) Ferrofluid is non-conductive
- d.) Steady state, laminar, irrotational and incompressible flow
- e.) No internal heat generation
- f.) The ferrofluid is not temperature-sensitive (Magnetocaloric effect is not considered)

The ferrofluid is assumed to be a colloidal solution of 11 nm diameter Magnetite (Fe_3O_4) nanoparticles and de-ionized water. The concentration of ferrofluid is assumed to be 5% and since the Curie temperature of magnetite is around 850 K [56], [57], it is a good assumption to neglect the temperature dependence of physical properties. The continuity and momentum equations are given by (1)-(3) as follows:

Continuity:

$$\frac{\partial u}{\partial x} + \frac{\partial v}{\partial y} = 0 \quad (1)$$

x and y Momentum:

$$u \frac{\partial u}{\partial x} + v \frac{\partial u}{\partial y} = -\frac{1}{\rho} \frac{\partial p}{\partial x} + \nu \left(\frac{\partial^2 u}{\partial x^2} + \frac{\partial^2 u}{\partial y^2} \right) + \frac{\mu_0}{\rho} \left(M_x \frac{\partial H}{\partial x} + M_x \frac{\partial H}{\partial y} \right) \quad (2)$$

$$u \frac{\partial v}{\partial x} + v \frac{\partial v}{\partial y} = -\frac{1}{\rho} \frac{\partial p}{\partial y} + \nu \left(\frac{\partial^2 v}{\partial x^2} + \frac{\partial^2 v}{\partial y^2} \right) + \frac{\mu_0}{\rho} \left(M_y \frac{\partial H}{\partial y} + M_y \frac{\partial H}{\partial x} \right) - g \quad (3)$$

The third term on the RHS in equations (2) and (3) are the Kelvin body force exerted on the ferrofluid due to non-uniform magnetic field. The ferrofluid magnetization and magnetic fields are assumed to be sensibly collinear, and hence there is no additional viscous term as was observed in the previous chapter, where a set inlet magnetization was imparted.

Energy Equation with a constant heat flux is given as:

$$u \frac{\partial T}{\partial x} + v \frac{\partial T}{\partial y} = \frac{1}{\rho C_p} \left(\frac{\partial^2 T}{\partial x^2} + \frac{\partial^2 T}{\partial y^2} \right) + \frac{\eta}{\rho C_p} \left\{ 2 \left[\left(\frac{\partial v}{\partial y} \right)^2 + \left(\frac{\partial u}{\partial x} \right)^2 \right] + \left(\frac{\partial v}{\partial x} + \frac{\partial u}{\partial y} \right)^2 \right\} \quad (4)$$

The following constitutive relations hold for the magnetic field:

$$\nabla \cdot \vec{B} = 0 \quad (5)$$

$$\nabla \times \vec{H} = 0 \quad (6)$$

$$\vec{M} = \chi_m \vec{H} \quad (7)$$

Since the ferrofluid is assumed to be generic, in order to find the material properties of the dissolved phase of the ferrofluid the following property relations, in terms of the volume fraction, ϕ , are used for the thermal conductivity, heat capacity, density and magnetic susceptibility of the ferrofluid [58]–[63]:

Thermal conductivity:

$$k = \frac{(2k_L + k_p - 2\phi(k_L - k_p))}{k_L + k_p + \phi(k_L - k_p)} k_L \quad (8)$$

Density:

$$\rho = (1 - \phi)\rho_L + \phi\rho_p \quad (9)$$

Heat capacity:

$$\rho C_p = (1 - \phi)(\rho C_p)_L + \phi(\rho C_p)_p \quad (10)$$

Viscosity:

$$\eta = \frac{\eta_L}{(1 - \phi)^{2.5}} \quad (11)$$

Magnetic susceptibility:

The initial Langevin susceptibility is given by:

$$\chi_i = \frac{\phi M_d m}{3\mu_0 k_B T_{ref}} \quad (12)$$

The magnetic moment of one magnetite molecule is 4 Bohr Magneton, which can be converted into volumetric quantity through[64], [65]:

$$m = \frac{4\mu_B \pi d^3}{6 \times 91.25 \times 10^{-30}} \quad (13)$$

The modified Langevin susceptibility for the ferrofluid is given by[59]:

$$\chi = \chi_i \left(1 + \frac{\chi_i}{3}\right) \quad (14)$$

The boundary conditions applied are:

- a) For fluid flow the flow is considered to be hydrodynamically fully developed as it enters the channel. The flow enters the channel with a preset Reynolds number which determines the inlet velocity. On the channel walls the flow has a ‘no-slip’ boundary condition.
- b) For magnetic field, since the magnetic susceptibility sharply varies at the air and channel interface (i.e. channel wall), the continuity of the normal B field and tangential H field is accounted for. To this effect the walls of the channel are considered to be perfect magnetic conductor. This combined with the constitutive relations described above maintain the continuity of the field. Moreover, the outer domain as shown in figure 1 of chapter 2 has the magnetic insulation boundary condition.

c) Finally, for the thermal boundary conditions, the whole of the channel walls is subjected to a net inward heat flux (q'') of 1000 W/m², with the inlet temperature set at 300 K. The reference temperature is set at 300 K.

In order to, quantify the heat transfer a Nusselt number is defined as:

$$Nu = q'' \times \frac{w_0}{(T_{wall} - T_{mean}) \times k} \quad (15)$$

Where, the mean temperature T_{mean} is defined as:

$$T_{mean} = \frac{\iint T \cdot U \, dA}{\iint U \, dA} \quad (16)$$

Where, A is the surface area of the channel and U the velocity magnitude.

Finally, the Reynolds number is defined as:

$$Re = \frac{U w_0}{\eta} \quad (17)$$

Table 4 summarizes the properties of the ferrofluid for $\phi = 0.05$.

Table 4 Ferrofluid physical properties

Property	Magnetite Particles	Water	Ferrofluid
Viscosity	none	0.001[Pa. s]	0.0011368 [Pa·s]
Density	5100[kg/m ³]	1000[kg/m ³]	1205 [kg/m ³]
Thermal conductivity	7[W/m-K]	0.585[W/m-K]	0.7096[W/m-K]
Specific Heat	660[J/kg-K]	4180[J/kg-K]	3435.1[J/kg-K]
Magnetic Susceptibility	-	-	0.72803

In order to study the effects of the non-uniform magnetic field generated by the parametric placement of the wires for both the channels different parameters are chosen. Then the system is

numerically modeled and 4 Nusselt numbers are calculated. These Nusselt numbers are for 4 different parts of the channel. They are as follows:

- a) Nusselt number for the whole channel
- b) Nusselt number for the whole bend
- c) Nusselt number for the first bend section (i.e. from bend inlet to bend center)
- d) Nusselt number for the second bend section (i.e. from bend center to bend outlet)

The choice of these Nusselt numbers allows for the quantification of heat transfer enhancement at local and global levels.

4. Numerical Modeling

COMSOL Multiphysics version 5.4 is used for numerically simulating the set of governing equations discussed in the previous section[47]. COMSOL is Finite Element Method (FEM) based software which solves conservation laws using the weak form and weighting functions of specified order. COMSOL uses Newton's method to solve the partial differential equations and for Navier-Stokes equation and uses stabilization methods based on Streamline Upwind Petrov Galerkin (SUPG) methods, which resolves the issue of oscillation of solutions in cases where upwinding is not used[52], [66]–[69]. The internal multiphysics interfaces/modules to couple magnetic and flow fields is utilized. Second order elements are used to discretize both pressure and velocity fields. The magnetic field is discretized using quadratic elements.

Since the inlet velocity is uniform entering the channel it can be expressed in terms of the Reynolds number. The solution procedure employed uses a segregated approach in which different dependent variable groups are solved simultaneously but separately within one iteration of the whole solution. The PARDISO algorithm is used to solve for all the segregated groups within the

segregated iteration of the solution for all the internal groups. The dependent variables solved for in groups are as follows:

- a) Group 1: Velocity and Pressure
- b) Group 2: Temperature
- c) Group 3: Magnetic vector potential, wire current and wire voltage.

A convergence criterion is set in tolerance to be 10^{-5} for the solution and residual for all the groups and the solution in one main iteration of the solution. This is in general considered to be a very tight convergence criterion[70], [71]. The parameters which were varied are stated in

Table 5.

Table 5 Parameter varied for simulation and their values/limits

Parameter	Values/Limits
Current in wire 1 (I_1)	-5, 0 and 5 [A]
Current in wire 2 (I_2)	-5, 0 and 5 [A]
Outer Radius of the bend	$2w_0$ (channel 1) and $4w_0$ (channel 2)
Angle of wires with horizontal (α)	30° , 45° and 60°
Reynolds Number (Re)	1 to 20

Since the current in the two wires have three values each, there would be 9 different cases of wire current as listed in **Table 6**. They are similar to the symmetric and anti-symmetric cases discussed in the previous chapter, but with more variability since the wires can carry zero current as well. Grid convergence studies were performed on a modified grid with N_{cell} going from 10 to 50, for both channels, for all the parameters and for the 9 current cases. It was observed that $N_{cell} = 40$ provides a very accurate solution with less than 2% variation of the Nusselt number values for the channel and bend compared to those calculated from $N_{cell} = 50$. Hence a value of $N_{cell} = 40$ is used in the simulations.

Table 6 Cases for current flowing in wire 1 and wire 2

Case Number	I_1	Direction for I_1	I_2	Direction for I_2
1	-5[A]	Into the plane	-5[A]	Into the plane
2	-5[A]	Into the plane	0[A]	none
3	-5[A]	Into the plane	5[A]	Out of the plane
4	0[A]	none	-5[A]	Into the plane
5	0[A]	none	0[A]	none
6	0[A]	none	5[A]	Out of the plane
7	5[A]	Out of the plane	-5[A]	Into the plane
8	5[A]	Out of the plane	0[A]	none
9	5[A]	Out of the plane	5[A]	Out of the plane

5. Results and Discussions

The heat transfer characteristics are analyzed using the 4 Nusselt numbers as described in the previous section. Each of the 9 cases are analyzed for each case of the angle α to obtain a comparison between the Nusselt numbers. Nusselt number % increase is also calculated for the channel and the bend for all the cases, angles and channel dimensions. The analysis is subdivided by channel size for a comparative study of Nusselt number for bend and channel. The next two subsections are for channel 1 and channel 2 respectively, comparing global (at the channel level) and local (at the bend level) heat transfer enhancements.

5.1 Results for Channel 1

Figure 16 shows the velocity magnitude for all the 9 cases summarized in table 6 for Reynolds number 5 and outer radius of the channel $2w_0$ (which is referred to as channel 1), when α is set to 45° . The fifth case shown in **Figure 16**, is where there is no current flowing through the wires, and hence is the reference case. It is observed from the velocity magnitude plots that

there is almost identical behavior exhibited by cases 1 & 9, cases 2 & 8, cases 3 & 7 and cases 4 & 6. This is contrary to what was observed in the previous chapter, while analyzing the mixing enhancement problem. This can be attributed to the absence of the external circuit which allowed for an additional inlet magnetization to be imposed on the ferrofluid. Hence, the 9 cases are reduced ultimately into 5 including one reference case. This observation is manifested in the plots of the Nusselt number for channel and bend as shown in **Figure 17**. The cases 1&9, 2&8, 3&7 and 4&6 overlap completely.

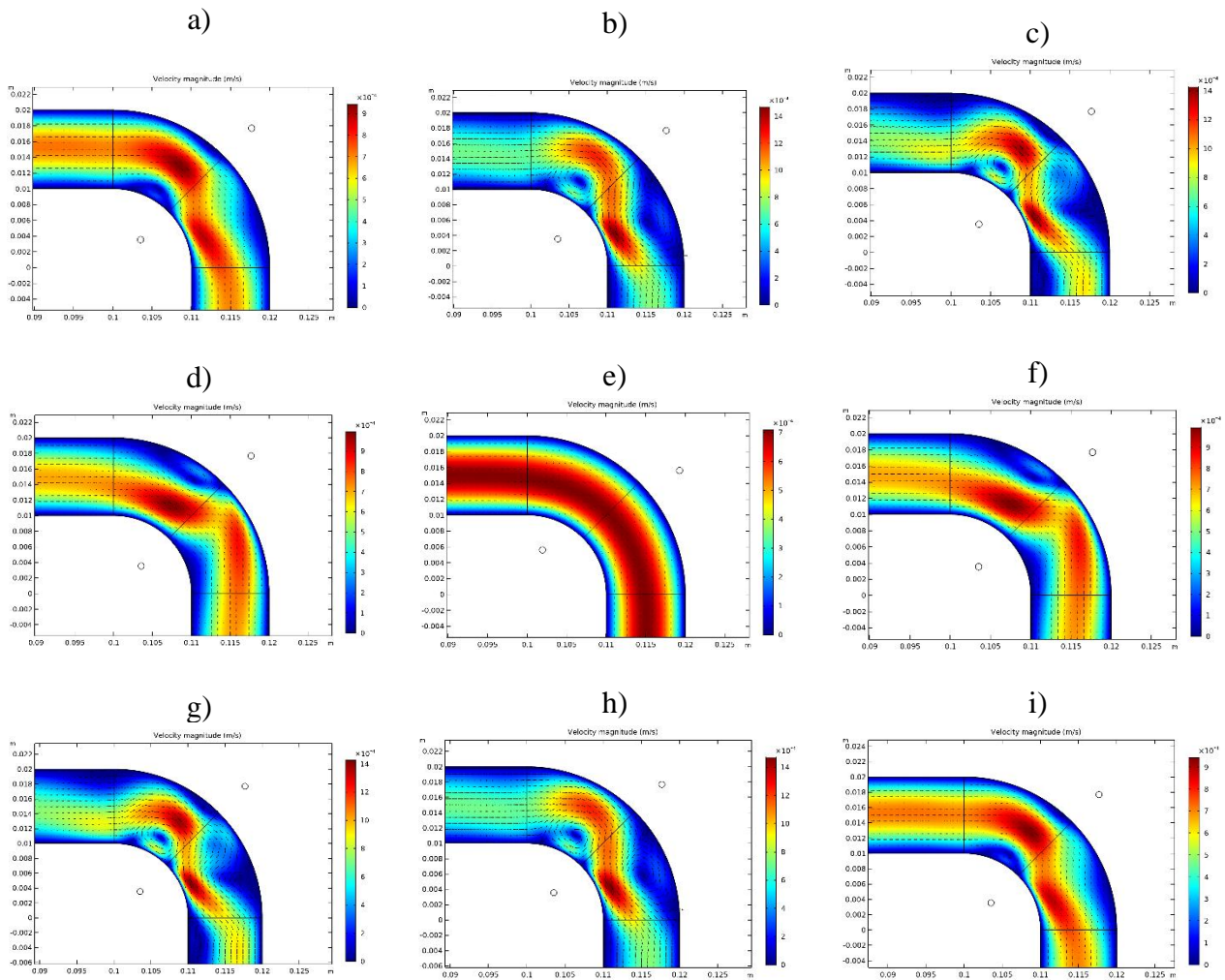


Figure 16 Velocity magnitude plot for $2w_0$ channel for $\alpha = 45^\circ$ for $Re = 5$ for a) Case 1 b) Case 2 c) Case 3 d) Case 4 e) Case 5 f) Case 6 g) Case 7 h) Case 8 i) Case 9

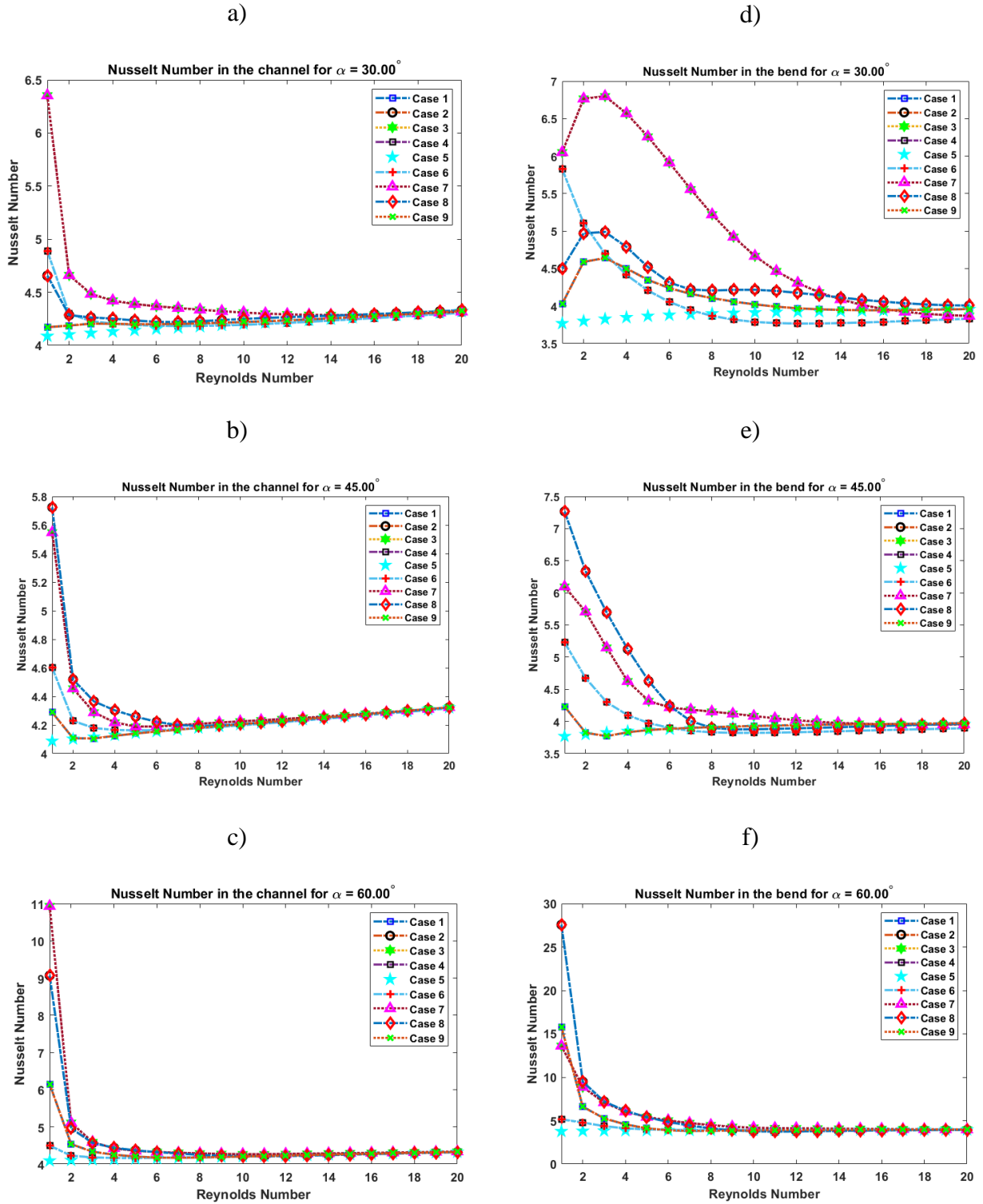


Figure 17 Nusselt number for $2w_0$ channel for a) Channel with $\alpha = 30^\circ$ b) Channel with $\alpha = 45^\circ$ c) Channel with $\alpha = 60^\circ$ d) Bend with $\alpha = 30^\circ$ e) Bend with $\alpha = 45^\circ$ f) Bend with $\alpha = 60^\circ$

Velocity scales of approximately two times that of the reference case are observed in cases 2,3,7 & 8 above. This is attributed to the magnetic field generated by the wires. It must be noted that the 4 sets of cases cited above are anti-symmetric to each other with respect to the direction of current. For instance, for case 2 I_1 is into the plane and I_2 is zero, and for case 8, which is equivalent to case 2, I_1 is out of the plane and I_2 is zero. Hence, the directionality of the current does not produce any significant change to the magnetic field such that it impacts the system. This can be attributed to the inherently symmetric positioning of the wires with respect to the channel center. This was not the case in previous section, because the magnetization of the ferrofluid was skewed in one direction. Hence, the magnetic boundary conditions are of very high significance.

Figure 17 shows the Nusselt number in the channel and the whole bend for all the three angle values (i.e. 30, 45 and 60°) for channel 1. It is observed that the highest Nusselt number for both channel and the whole bend is achieved when $\alpha = 60^\circ$. The Nusselt number very significantly drops as the Reynolds number increases and achieves the reference case value at Reynolds number 20. This is very similar to what was observed with mixing enhancement. The magnetic force that induces the vortical structures is overpowered by inertia, which forces the system achieve its normal state as the Reynolds number increases. **Figure 18** presents the % increase in Nusselt number over the reference case (case 5) for all the other cases. Here the highest increase is seen for $\alpha = 60^\circ$ for both the channel and for the whole bend. It is also observed that case 2&8 and case 7&3 achieve the highest increase for all three angles ($\alpha = 30^\circ, 45^\circ$ and 60°). Cases 1&9 and 4&6 have the lowest percentage increase for both the channel and bend. Both these cases have current flowing through wire 2 but none through wire 1. Hence, it can be inferred that wire 2 has a lower impact on the heat transfer enhancement, as compared to wire 1. Furthermore, for $\alpha = 45^\circ$ & 60° the Nusselt number increase in the whole bend exhibits similar behavior for all

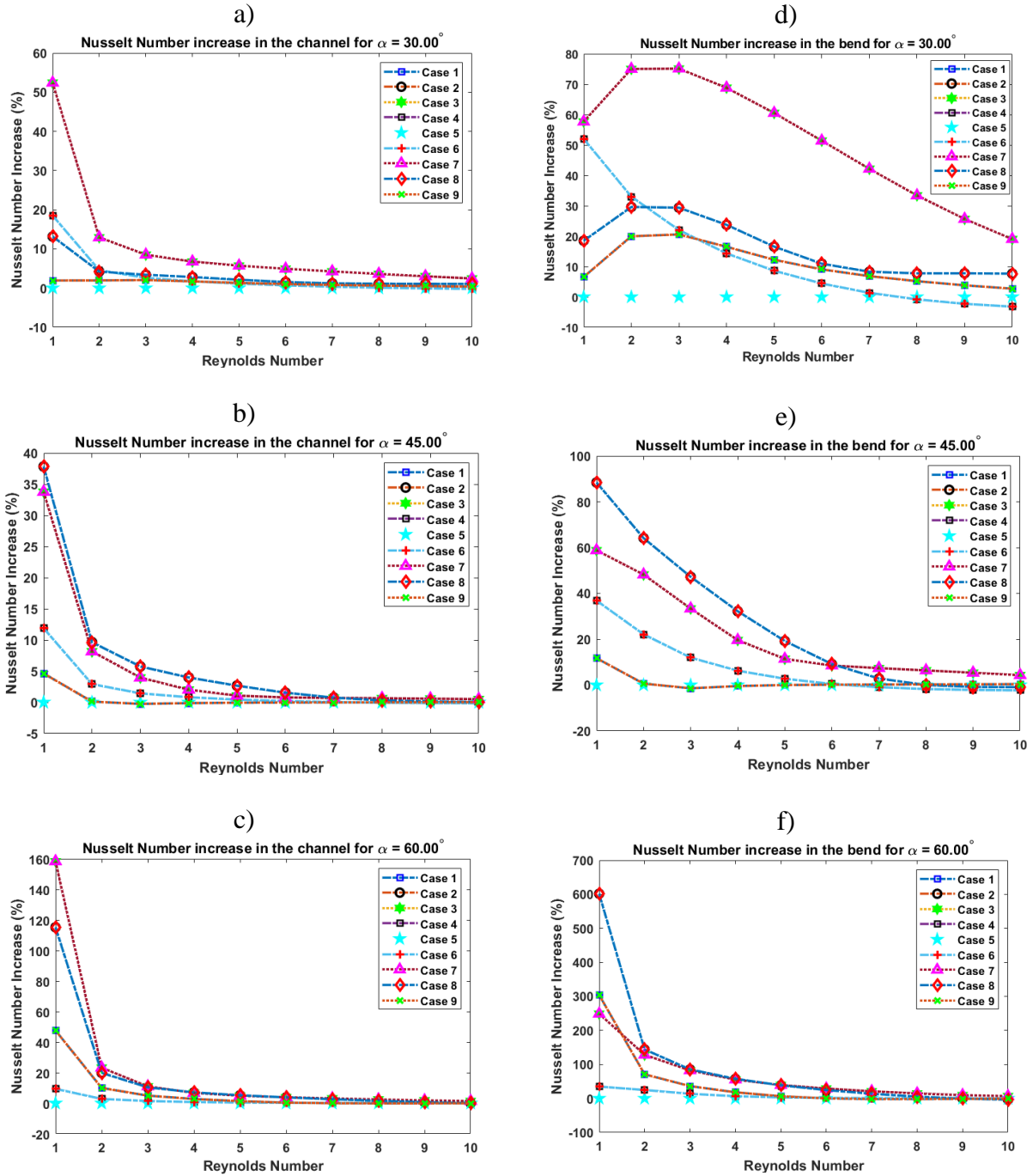


Figure 18 % increase in Nusselt number for $2w_0$ channel for a) Channel with $\alpha = 30^\circ$ b) Channel with $\alpha = 45^\circ$ c) Channel with $\alpha = 60^\circ$ d) Bend with $\alpha = 30^\circ$ e) Bend with $\alpha = 45^\circ$ f) Bend with $\alpha = 60^\circ$

the cases, however, this is not observed for $\alpha = 30^\circ$, because of the skewed magnetic field produced with respect to the channel. It is observed that case 7, case 8, and case 4 undergoes a transformation in which the Nusselt number in the bend increases first with the Reynolds number

and then starts decreasing. Since, this behavior is not exhibited by the other two angular configurations, it must be the effect of the magnetic field generated by the wires at this angle. Finally, within the bend there is a significant increase in the Nusselt number in the bend, even for higher Reynolds numbers. The highest increase is 600% in the bend for $\alpha = 60^\circ$. This decreases very quickly as the Reynolds number increases from 1 to 2, at which point the % increase in the Nusselt number in the bend is between 100 & 200 %, which is still a very significant increase in the heat transfer.

5.2 Results for Channel 2

Figure 19 shows that similar to the channel 1, there is exact congruence between the 4 pairs of two cases i.e. cases 1 & 9, cases 2 & 8, cases 3 & 7 and cases 4 & 6 for channel 2. Since channel 2 has twice the outer radius as compared to channel 1, the bend area is much larger than that of channel 1. Hence, the magnetic field generated by the wires must cover more area in order to obtain same heat transfer enhancement as in channel 1. Since, the current magnitude is not altered it is expected that the heat transfer enhancement for channel 2 must be less than that in channel 1.

Figure 20 quantifies the % increase in the Nusselt numbers for the whole channel and for the whole bend of channel 2. It is observed that the highest heat transfer enhancement is for $\alpha = 60^\circ$ for the whole bend, and for the channel. However, the magnitude of the % increase is less than half the value found for channel 1. The Nusselt number profiles shown in **Figure 19** are much smoother as compared to those for channel 1, which is a consequence of the increased area. Similarly, cases 7 & 8 have the highest overall increases for the whole bend and the channel for $\alpha = 60^\circ$. However, for $\alpha = 30^\circ$ and 45° case 6 & 4 gain over case 7. This again can be attributed to the increased area of the bend and the displacement of wires with respect to the walls of the channel. Finally, all the observations are similar to that of channel 1 for heat transfer enhancement,

where with the increase Reynolds number, the system moves away from the influence of the magnetic field, and slowly returns to its normal state.

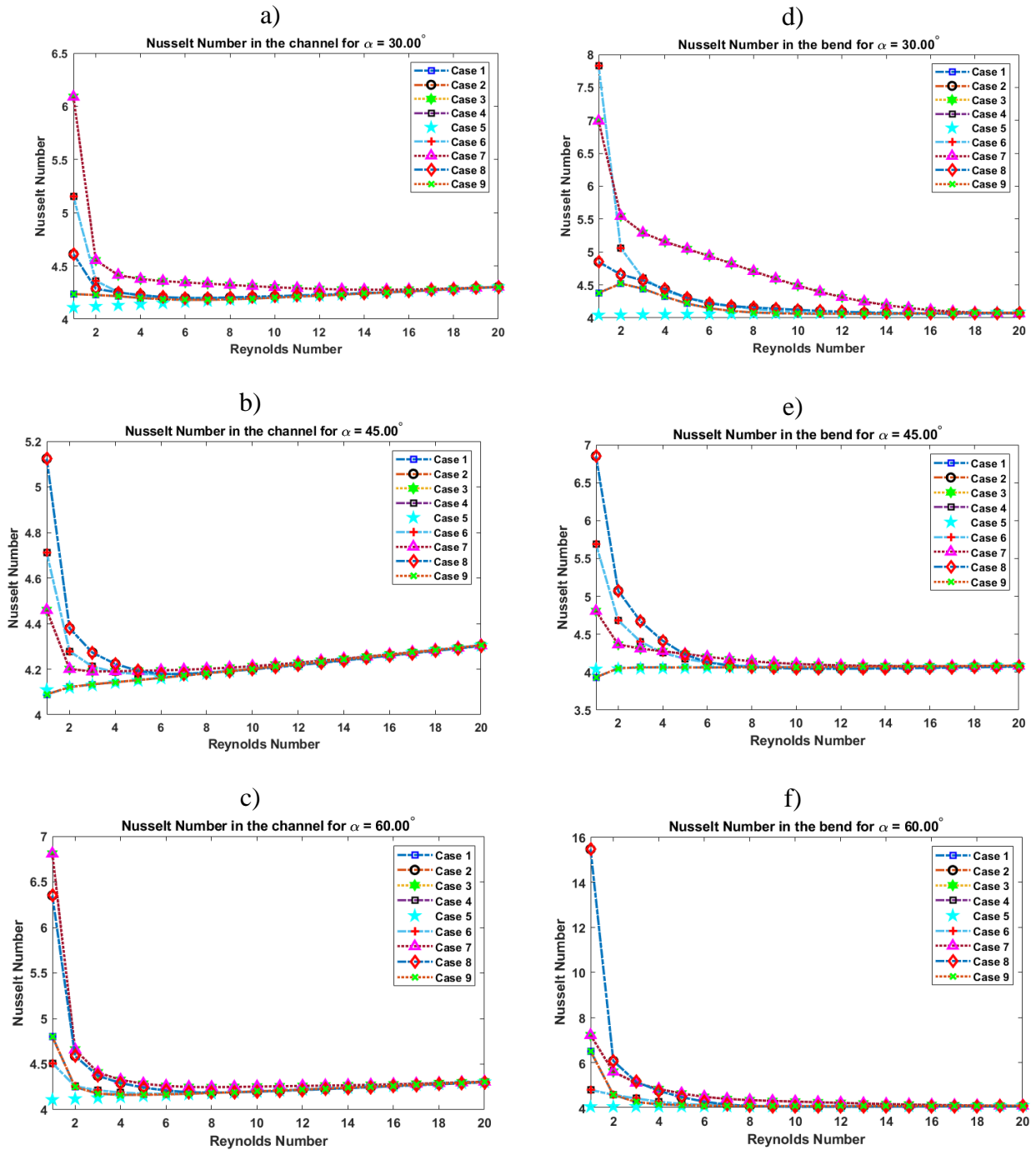


Figure 19 Nusselt number for $4w_0$ case for a) Channel with $\alpha = 30^\circ$ b) Channel with $\alpha = 45^\circ$ c) Channel with $\alpha = 60^\circ$ d) Bend with $\alpha = 30^\circ$ e) Bend with $\alpha = 45^\circ$ f) Bend with $\alpha = 60^\circ$

It must also be noted that, in the formulation for the Nusselt number as state in equation (15), the Nusselt number is inversely proportional to temperature difference.

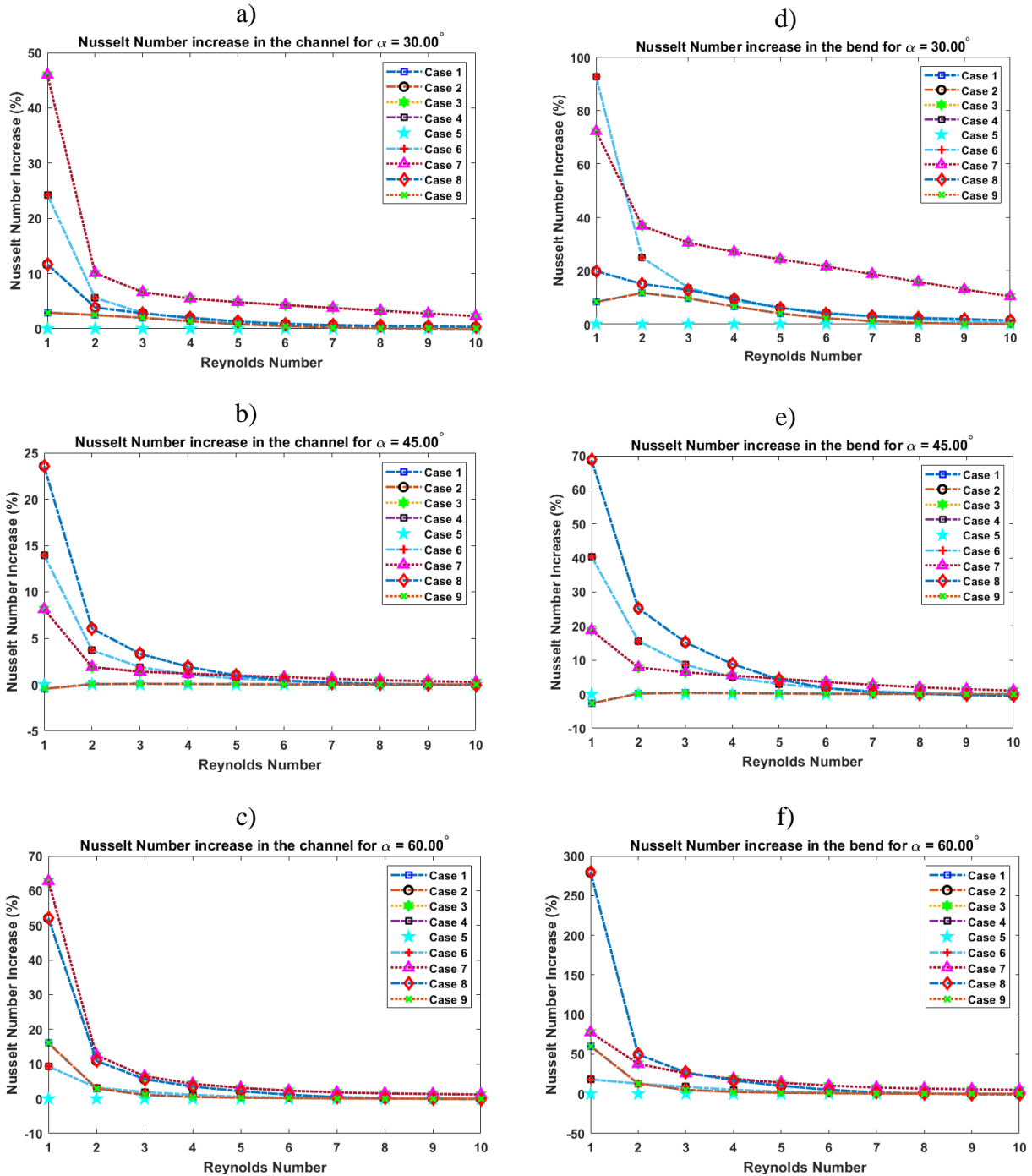


Figure 20 (%) increase in Nusselt number for $4w_0$ case for a) Channel with $\alpha=30^\circ$ b) Channel with $\alpha=45^\circ$ c) Channel with $\alpha=60^\circ$ d) Bend with $\alpha=30^\circ$ e) Bend with $\alpha=45^\circ$ f) Bend with $\alpha=60^\circ$

Hence, the Nusselt number must increase as the temperature difference decreases, which happens for higher Reynolds number in Laminar flow. This is a consistent observation seen in case 5 (no current case) for both the channels and for the bends of these channels.

6. Conclusions

In this chapter ferrofluid flow through two 90° elbow channels are numerically studied. The ferrofluid is subjected to a non-uniform magnetic field which is generated by two parametrically placed current carrying wires. These wires are radially placed at a fixed distance from the channel center but are displaced angularly at particular angles, around the channel center. This produces a unique configuration in which the angular displacement of the current carrying wires (or magnetic field producing system) can preferentially alter the flow field inside the channel. Three angular displacements were studied, namely $\alpha = 30^\circ, 45^\circ$ and 60° . For these three angular displacements, there are 9 cases for the wires, in which the wires can either carry no current, or carry 5 [A] either into the plane or out of the plane.

A 600% increase in Nusselt number was achieved for channel 1, for the lowest Reynolds number value of 1. As the Reynolds number increased the Nusselt number values approached the reference values. This behavior with Reynolds Number is universal regardless of flow manipulation configuration. However, there are some significant new observations, which can render the design of such systems very useful for electronics cooling at microscales. The most important observation is that there is symmetry with respect to the current direction in the wires. This can be useful while providing non-uniform magnetic field to the channel through a current loop wound around a 3-D channel. Secondly, without adding a radial degree of freedom, the system can respond to higher demands of cooling through angular displacement of the wires, which can lead to the design of adaptive cooling systems.

PART III: Application of Ferrohydrodynamic Flows for Energy Harvesting

Chapter 1: Introduction

1. Energy Harvesting

Energy harvesting of different ambient sources of energy has become a major area of research. Energy harvesting is basically a process of converting ambient or unused energy into useful electrical energy, through a miniature transduction mechanism. It is used mainly in places where large energy conversion devices, like hydro/steam turbines, IC engines etc. cannot be used for converting energy. The goal of energy harvesting is to provide a sustainable power source to stand alone devices, like sensors, actuators etc., by utilizing ambient energy and without needing to store energy [72]–[74]. Energy harvesting devices have the potential to replace bulky batteries and deliver lightweight solutions for sensing and actuation and make them essentially wireless [75]–[77]. It is also helpful in increasing the efficiency of general energy conversion devices, like thermoelectric devices used for waste heat recovery.

Energy harvesting usually requires a transduction mechanism, to convert ambient/waste energy into a useful electric energy form [78]–[80]. **Figure 21** depicts the working of an energy harvesting device schematically.

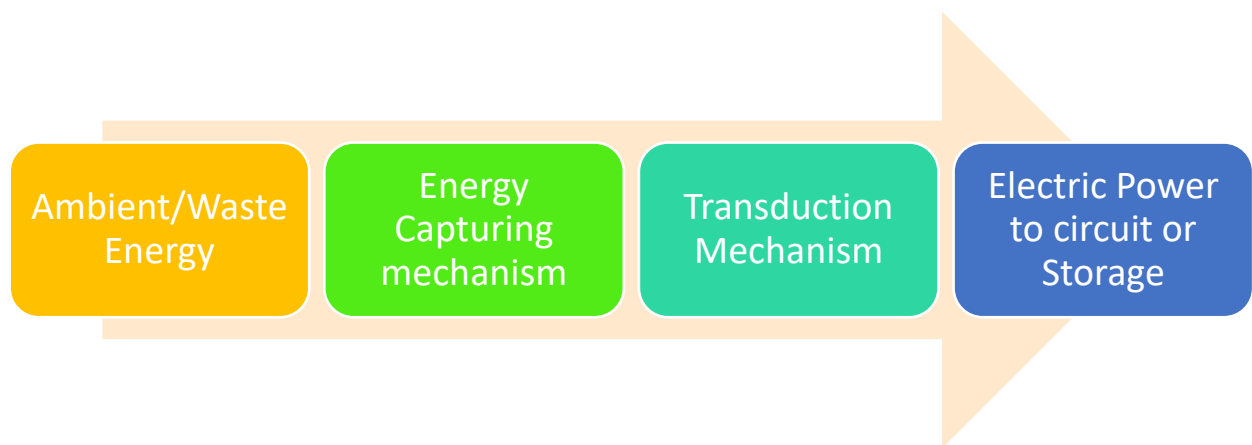


Figure 21 Schematic representation of an energy harvesting device

The energy harvesting device captures ambient or waste energy through an energy capturing mechanism, this captured energy is then used by a transduction mechanism which converts it into useful energy (which is electric power). The most general examples are thermoelectric devices, piezoelectric devices, ionic polymer metal composites, etc.[72], [73], [81]. However, recently there have been energy harvesters which use a liquid state transduction mechanism to obtain electric power, for example a ferrohydrodynamic vibration energy harvester [23], [82]. Fluid mechanics can be applied in energy harvesting by both solid and liquid state transducers. For solid state transducers fluid acts as the energy source for the forcing function required to deform part of the harvester, and in liquid state transducers, the fluid acts as both the energy carrier and deformed harvester. This is shown as a schematic in **Figure 22**. Solid state transduction mechanisms use any instability created in the flow field to excite the transduction element at a particular frequency (usually natural frequency of the structure), and harvest energy via inherent electromechanical coupling of the harvester.

In the following sections we will discuss harvesting energy from a fluid media by means of piezoelectric materials, ionic polymers, sonic crystals and ferrofluids.

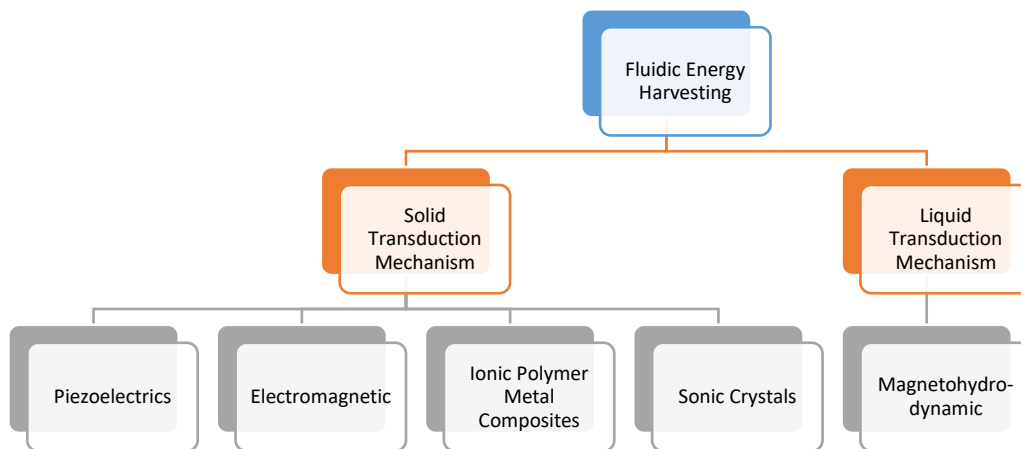


Figure 22 Classification of Fluidic Energy Harvesting methods

2. Fluidic Energy Harvesting through Solid State Transduction

Mechanisms

In hydrokinetic energy conversion, the fluid flow carries enough force and energy to rotate a wind turbine or a water turbine to generate electricity. However, there are various ways in which fluid flow can be utilized to create an input like a forcing function for a ‘solid state’ energy harvester. In general, any solid-state energy harvester used to generate electricity would require an unsteady force to deform the solid, thereby creating strain or motion. This strain or motion is then converted into electrical displacement, which would be time varying and hence would result in a current. Piezoelectric materials are the most widespread and most efficient solid-state energy harvesters [77], [79], [83]–[86].

2.1 Ionic Polymer Metal Composites

Ionic polymer metal composites (IPMC) are made up of a type of electro-active polymer, laden with free ions, which can be mobilized on applying deformation. The IPMCs is constructed using an electro-active ionic polymer, which is saturated with an electrolytic solution, sandwiched between two noble metal electrodes [87]–[90]. The electrodes are used to provide or pick-up voltage to or from the polymer, for transducer or energy harvesting operations, respectively. There can be many configurations in which an IPMC device can be used as a transduction mechanism for harvesting energy from a fluid flow. Usually these configurations are designed for three types of flow: steady, unsteady, or oscillatory.

a.) IPMC energy harvesting from flapping flags

For steady flows, the most common way is to use a deformable flag with an IPMC strip attached to it. As the fluid flows over the flag, it deforms and starts flapping [91], [92], and then

transmits this deformation onto the strip. Due to this deformation there is a flow of ions between the metal electrodes, generating current.

Figure 23 shows flag based steady flow IPMC energy harvester attached to a thin elastic flag of infinite extension in x direction, under a two-dimensional, incompressible, inviscid flow with a free stream velocity of U , density ρ , bending stiffness B_{flag} , length L_{flag} , width w_{flag} and mass m_{flag} . Using the Kirchhoff-Love plate model for the flag, three dimensionless groups are defined to map the performance of the device[91], [92]:

$$R_1 = \frac{m_{flag}}{\rho L_{flag} w_{flag}} = \frac{\text{mass of flag}}{\text{mass of surrounding fluid}}$$

$$R_2 = \frac{B_{flag}}{\rho U^2 L_{flag}^3} = \frac{\text{elastic force on the flag}}{\text{force applied by fluid on the flag}}$$

$$R_3 = \frac{TL_{flag}^2}{B_{flag}} = \frac{\text{Stiffening effect from Tension}}{\text{Bending stiffness of the flag}}$$

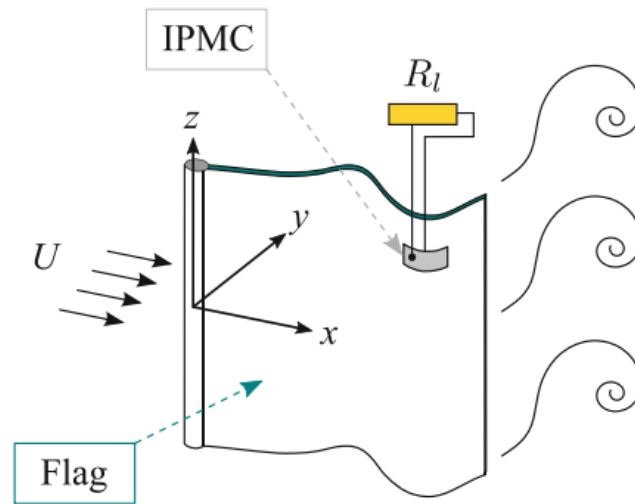


Figure 23 Energy harvesting from IPMC attached to a flapping flag [91]

The simulated and experimentally measured power output from the flag based IPMC energy harvester is in the range of nano to pico watts [91]. This is when the IPMC strip covers

only 2% of the flag area and contribute about 0.5% of weight [91]. The harvested power and efficiency is lower compared to a piezoelectric, but IPMCs work very well under water and has high inherent capacitance which makes it attractive for the purposes of harvesting and storing power simultaneously [93]–[95].

b.) IPMC energy harvesting from oscillating flow

Another way to generate a fluidic forcing function as a source of deformation for the IPMC can be from an oscillating flow of a fluid [96]–[98]. IPMCs work well under water, which makes them a natural choice for dense fluid energy harvesting, and one such experimental effort is shown in **Figure 24**.

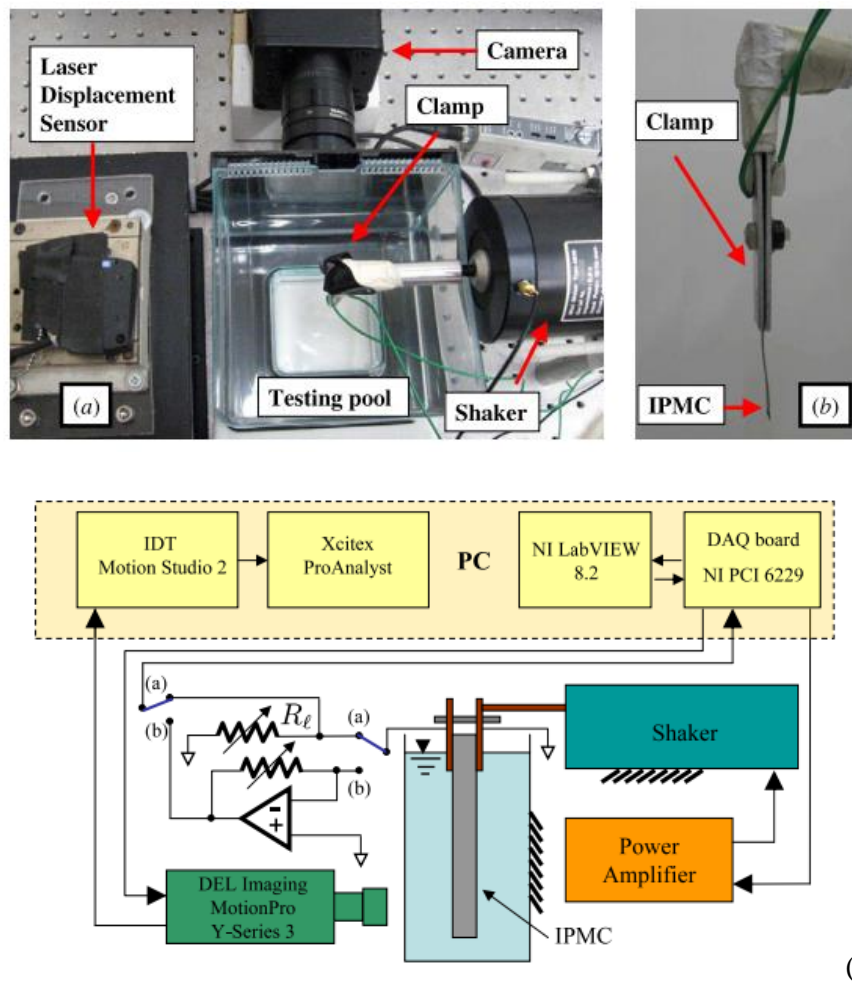


Figure 24 Energy harvesting from IPMC by the action of an oscillating fluid a) & b) experimental setup, c) schematics [99]

The experimental setup and schematic showed in **Figure 24** works similar to an oscillating fluid deforming the IPMC, however, the forcing function is directly applied on the IPMC, creating an oscillatory motion, thereby imparting the fluid with an oscillatory input. This moving fluid then deforms the IPMC at the opposite end from the shaker and produces current. It is to be noted that the shaker merely generates the conditions prevailing in an oscillatory fluid medium, and the actual working conditions of this IPMC energy harvester would use water waves, or sloshing water as an input[73], [91], [97], [98], [100]. It has been observed that the harvested power varies from $10^{-20} - 10^{-8} \frac{W}{mm^2}$, and monotonically increases with the excitation frequency of the shaker[91].

c.) Energy harvesting of vortex using IPMC

Of all the non-linearities in a fluid flow, perhaps the most potent for energy harvesting, would be the formation of vortices, which can be formed even in a quiescent fluid by a small modification in path of the flow, without disturbing the bulk of the flow[72], [73], [101].

The mechanics of energy transfer from a self-propagating vortex ring in a quiescent fluid, to an IPMC has been experimentally studied very extensively. Two such studies are shown in **Figure 25**, in which a piston in a cylinder is used to generate vortices which later goes ahead and impacts a cantilevered beam containing an IPMC. Due to the vortex field, the IPMC bends and generates power. The power generated depends on the inertia of the beam and the fluid, and the strength of the vortex formed by the plunger. Three dimensionless groups are identified to represent this interaction, and are given as:

$$\mu_1 = \frac{m}{\rho \omega L} = \frac{\text{mass of IPMC beam}}{\text{mass of the fluid surrounding the beam}}$$

$$\mu_2 = \frac{B}{\rho \Gamma^2 L} = \frac{\text{IPMC Beam stiffness}}{\text{force exerted by the vortex}}$$

$$\mu_3 = \frac{a}{L} = \frac{\text{length of the vortex ring}}{\text{length of the IPMC beam}}$$

The non-dimensional groups are very similar to those for the case of flapping flag. However, in the case of vortex generation the vortex ring length ratio is very important. Computations were performed using the above three groups, to ascertain the amount of energy that is transferred from the vortex to the beam. The range of this energy transfer is between 0.5% and 1.5% [102].

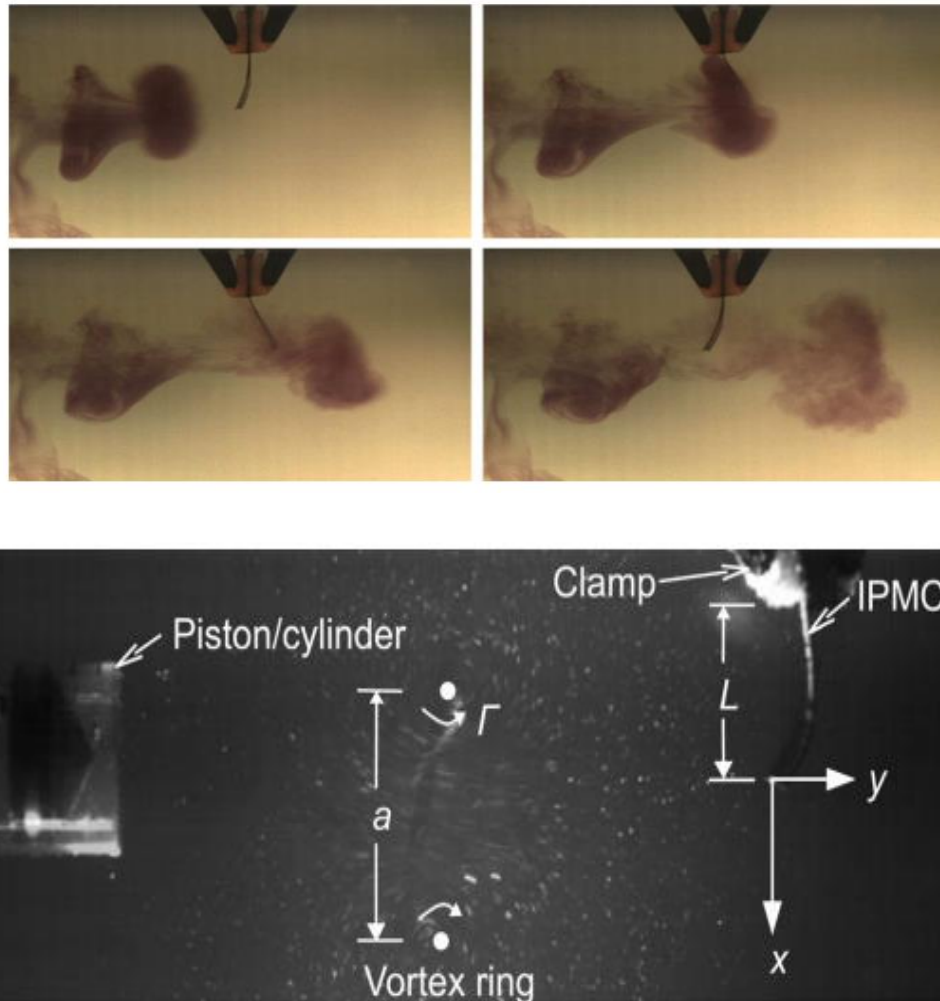


Figure 25 Energy harvesting from IPMC energy harvester by action of vortex induced deformation [102], [103]

2.2 Piezoelectric Energy Harvesting Using Flow Induced Vibrations

Piezoelectric materials are a class of multi-functional materials, which exhibit an electromechanical coupling. This coupling exhibits itself when a mechanical stress is applied to

the material, which thereby produces an electric displacement, resulting in electric current. The reverse of this is also exhibited, as the piezoelectric material produces strain when an electric field is applied. For energy harvesting, the forward electromechanical coupling is necessary, as it delivers current [104]. To harvest ambient energy in the form of stress, piezoelectric materials are generally attached to cantilevered beams, which oscillate when an ambient energy source is available. This oscillation serves as the stress in the piezo, which produces current. Flow fields can be modified to create spatial and temporal disturbances in the field, which can act as a source of stress for a piezoelectric.

Before discussing the configuration, it is imperative that the force field couplings in these aero-elastic energy exchanges is discussed. A schematic of the coupling is shown in **Figure 26**, where the fluid flow field is coupled to the solid deformation field, which in turn is coupled to the electric field generation in the piezo, and further ahead to the electric conditioning stage where this electric current is harvested in the form of power [75]. This coupling can be depicted in the form of an efficiency coupling, given as:

$$\eta_t = \eta_{ae} \times \eta_{em} \times \eta_{ec}$$

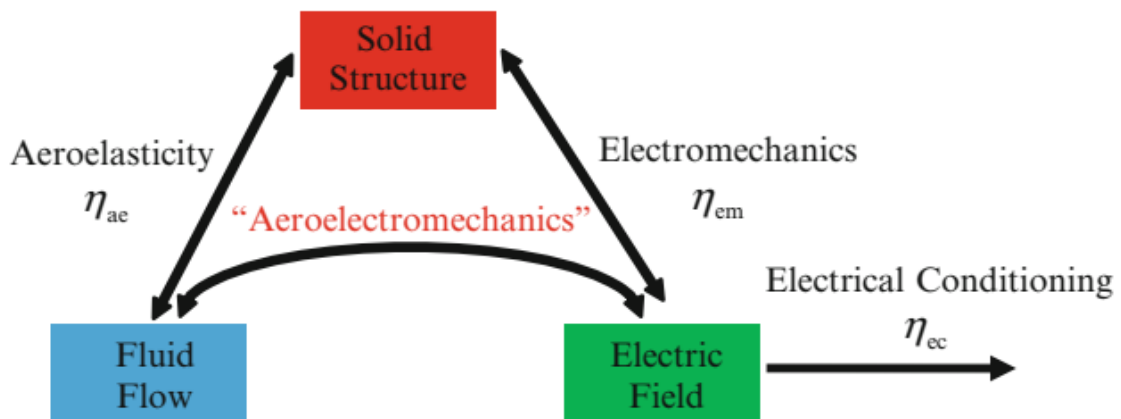


Figure 26 Aeroelectromechanical coupling in flow based piezoelectric energy harvesters [75]

Where, η_t is the total energy harvesting efficiency, η_{ae} is the ‘aeroelastic efficiency’, which depicts the conversion of the kinetic energy of the fluid flow (vortex) into the time-dependent strain energy of the piezo harvester through the flow induced vibrations of the beam, η_{em} is the ‘electromechanical efficiency’ which is the conversion of the piezo strain energy into AC electrical energy, and finally the η_{ec} ‘electrical conditioning efficiency’ which deals with the conversion of this AC electrical energy into final realizable electric power, by means of various devices like rectifiers, boosters, batteries, etc. For the purpose of fluid mechanics and energy harvesting only the first two are relevant and are very useful in order to optimize the configuration.

As discussed above, in the case of IPMC energy harvester, in which a vortex was created in a quiescent fluid using a piston and cylinder arrangement [102], [105]. A similar concept is applied to a piezoelectric energy harvester, where a bluff body is used to create vortices in its wake, which impinge on the piezoelectric beam, as shown in **Figure 27**.

In **Figure 27** a configuration with a cylindrical bluff body producing ‘Karman Vortices’ is shown. These vortices then impinge on the piezoelectric beam and generates strain in the piezo material. These vortices are periodically shed from the top and bottom of the cylinder and keep deflecting the beam. Since piezoelectric device is a solid structure, it has a set of natural frequencies, which are not closely spaced, but when the beam vibration frequency reaches any one of these, then high-power outputs and strain are realized. The frequency of the beam vibration is equal to the frequency of vortex shedding from the bluff body, and is given by[106], [107]:

$$f_s = St \frac{U_\infty}{d_c}, St - \text{Strouhal Number, and } d_c - \text{diameter of cylinder}$$

The Strouhal number depends upon the Reynolds number Re as. Vortex shedding begins once $Re \geq 40$. The Strouhal number, $St = 0.1$ for $40 < Re < 300$ and reaches a value of 0.2 for $300 < Re < 20000$. After Reynolds number goes above 100,000, a turbulent boundary layer is formed

around the bluff body and turbulent vortex shedding starts, and then the Strouhal number monotonically increases with Re [108], [109]. The harvested power depends upon the distance of the beam from the bluff body and the free stream velocity. The maximum power extracted is in the range of micro watts.

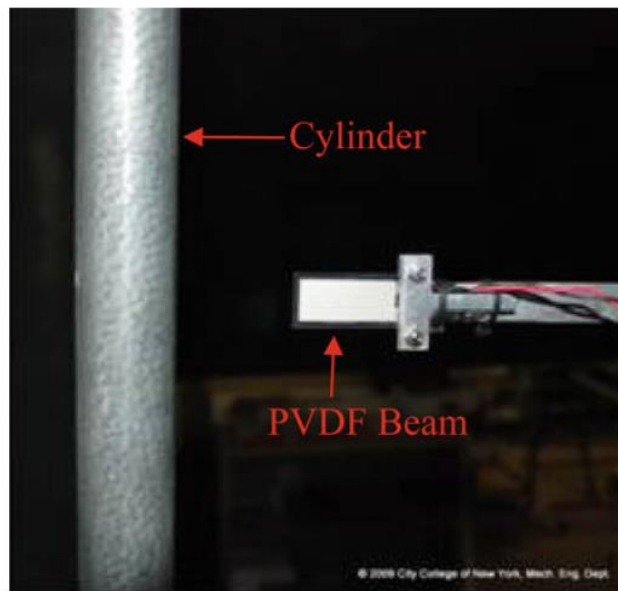
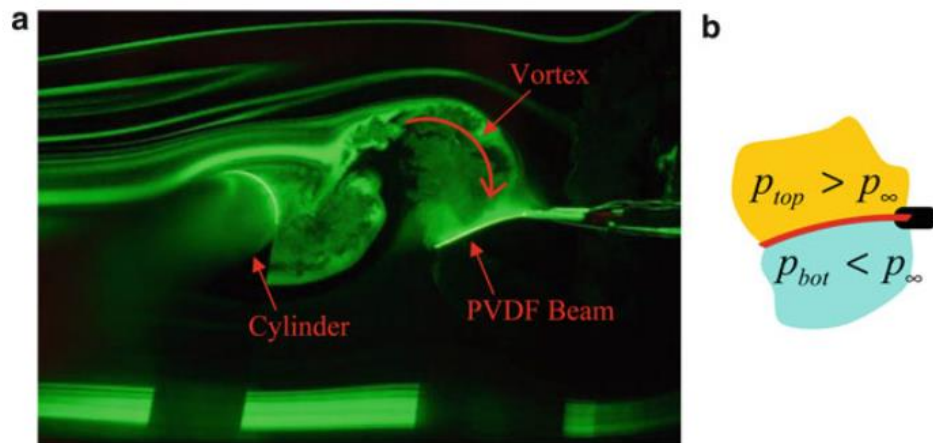


Figure 27 Piezoelectric in the wake of a bluff body a, b- side view of vortex interacting with a PVDF beam a PIV image , c- top view of the experimental setup [107], [110]

Figure 28 shows a modified configuration between a bluff body and a piezoelectric bimorph cantilever beam. Here instead of the beam being separate from the bluff body, the beam

is attached to the bluff body and clamped at the other end [74], [85], [111], [112]. This is done in order to take advantage of the lift, drag and aerodynamic moment forces acting on the bluff body. When the bluff body is joined to the beam, the lift, drag and aeroelastic moments all act on the beam, and by extension on the piezoelectric bimorph. This naturally increases the applied stress on the piezo, thereby increasing the power harvested. The highest power harvested is around 0.1 mW, which is almost 3 orders of magnitude higher than that with the unattached beam, in configuration 1. The reason for this variation can be ascertained by calculating the individual efficiencies, and checking which configuration has a significantly higher, individual efficiency. This is done through computational simulations in Ansys, using the Navier Stokes equations and a lumped mass system actuator and sensor equations[73], [110], [112], [113].

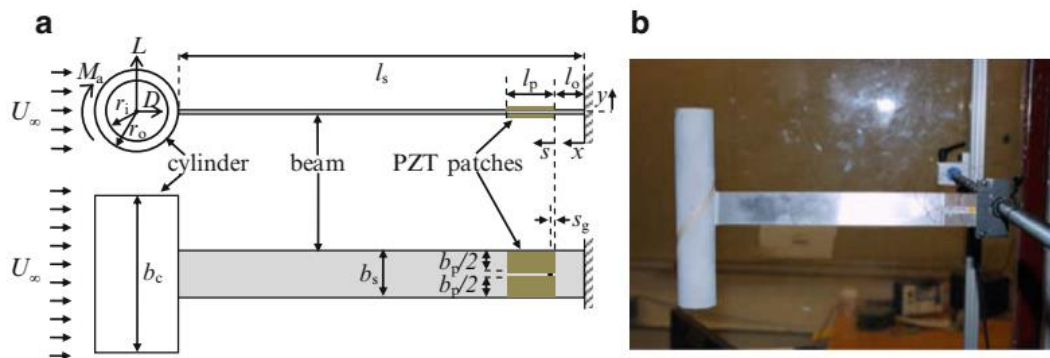


Figure 28 a) Schematic top and side view of the bluff body attached harvester and b) Experimental setup

The most notable result is the aeroelastic efficiencies of the two configurations, which is two orders of magnitude larger for configuration 1 i.e. with the unattached beam, than for configuration 2, i.e. with the attached beam. Hence, configuration 2 is much more efficient at capturing the energy from fluid flow, than configuration 1.

2.3 Piezoelectric Energy Harvesting Using Airfoil Fluttering

Piezoelectrics can also be used in airfoil-based energy harvesting, like flapping flags, flutter etc. [81], [114]–[116]. Fluttering of an airfoil is a source of linear and non-linear vibrations, which can be used for energy harvesting via piezoelectric or electromagnetic induction [116]–[118]. These vibrations are generally non-linear Limit Cycle Oscillations (LCOs), which can occur in two modes of airfoil operation, supercritical and subcritical, with respect to the linear flutter speed. These fluttering oscillations are an ideal source of vibration for a piezoelectric beam. These oscillations can also be used in electromagnetic-induction based energy harvesting. **Figure 30** below shows the piezo aeroelastic and electromagnetic induction, fluttering wing energy harvesters.

The working mechanism of both of these is very simple and can be solved by a 2-degree of freedom (Pitch and Plunge) lumped mass system of equations. In the piezo aeroelastic system, the fluttering oscillations are transferred to the torsional spring, which exerts a stress on the piezo beam. This general system is represented in **Figure 29**.

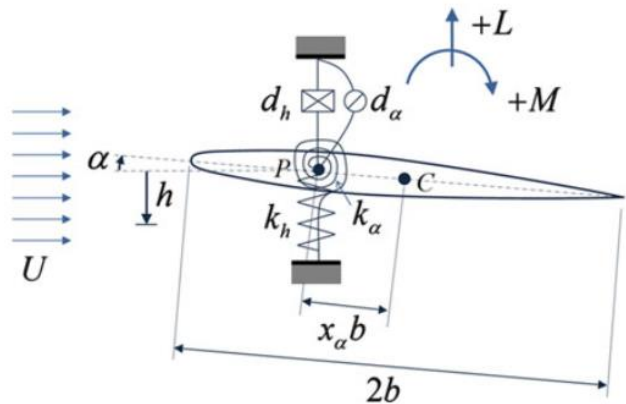


Figure 29 A general 2 DOF aero elastic energy harvester configuration [74], [81]

The governing equations are:

$$(m + m_e)\ddot{h} + mbx_\alpha\ddot{\alpha} + d_h\dot{h} + k_h h - \frac{\theta}{l} v = -L$$

$$mbx_{\alpha} \ddot{h} + I_{\alpha} \ddot{\alpha} + d_{\alpha} \dot{\alpha} + k_{\alpha} \alpha = M$$

$$C_p \dot{v} + \frac{v}{R_l} + \theta \dot{h} = 0$$

Where, l is the span length, R_l is the electric load resistance, v is the voltage across the resistive load, C_p is the equivalent capacitance of the piezo ceramic layer, and θ is the electromechanical coupling. L is the lift force and M is the moment on point P.

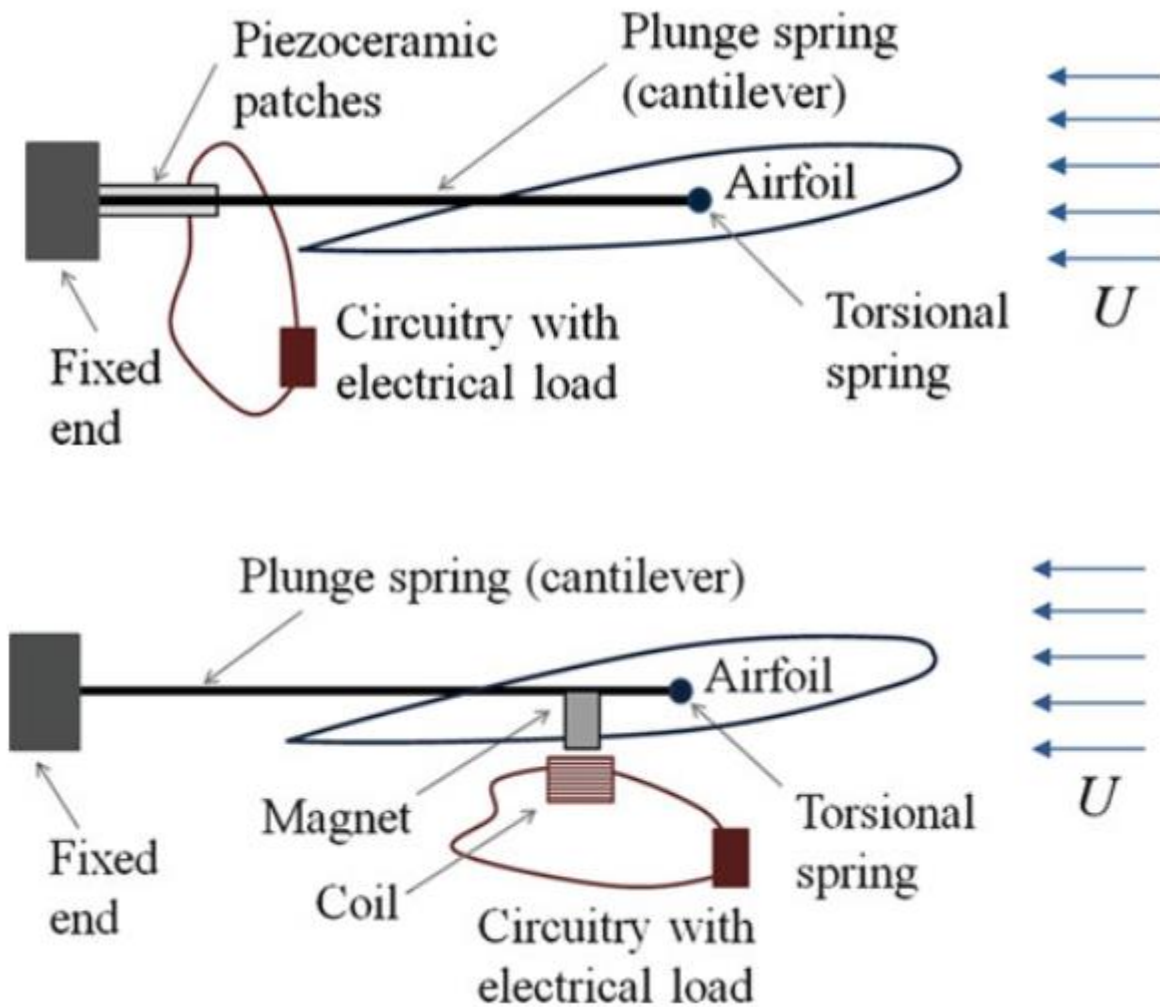


Figure 30 Airfoil based energy harvesters a) Piezo aeroelastic b) Electromagnetic Induction based [81], [119]

Similarly, the governing equations for electromagnetic induction configurations are:

$$(m + m_e)\ddot{h} + mbx_\alpha\ddot{\alpha} + d_h\dot{h} + k_h h - \frac{B_l}{l} I = -L$$

$$mbx_\alpha \ddot{h} + I_\alpha\ddot{\alpha} + d_\alpha\dot{\alpha} + k_\alpha\alpha = M$$

$$L_c\dot{I} + (R_e + R_l)I + B_l\dot{h} = 0$$

where, l is the span length, R_l is the electric load resistance, R_c is the internal resistance of the coil I is the induced electric current, L_c is the coil inductance, and B_l is the electromagnetic coupling.

These two energy harvesters were simulated and experimentally tested, and the power output was measured to be around 13 mW for linear fluttering, and around 40 mW for non-linear fluttering (Free play and other non-linearities). The power harvested is the highest amongst the energy harvester configurations discussed so far, which are due to the high stresses induced in the piezoelectric material through the airfoil [115]–[117].

2.4 Acoustic Energy Harvesting Using Sonic Crystals and Piezoelectric Beam

Sonic crystals (shown below in Figure 31) are periodic composite materials, with special acoustic characteristics.

The propagations of acoustic waves through them can create special effects, which can be used in making acoustic filters, noise control etc. [120], [121]. It is made up of solid cylindrical rods equidistant from each other, one of which is removed in order to create a cavity. This defect in the sonic crystal, in the form of a cavity, can create resonance, when an acoustic wave which has the same frequency as the resonance frequency of the crystal passes through it. **Figure 31** shows a schematic arrangement of sonic crystal with a cavity and a piezoelectric beam placed in the cavity. The purpose of this is to impart a stress wave to the piezo, by creating a pressure difference across the piezo beam, which is achieved by the propagation of the acoustic wave through the cavity[122]–[124].

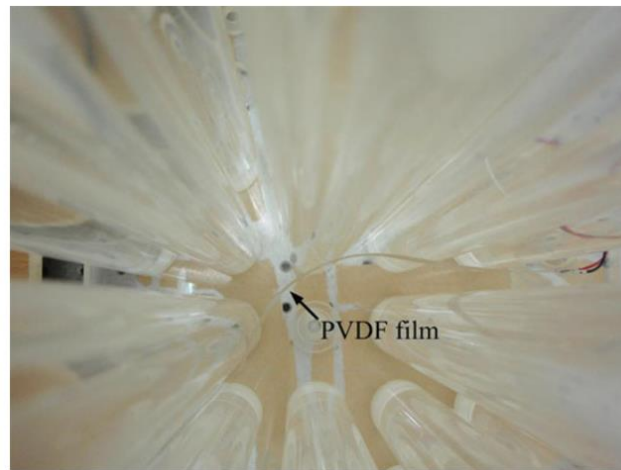
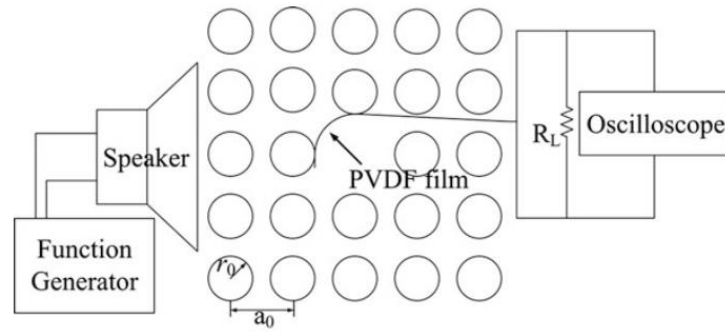


Figure 31 Energy harvesting from acoustic waves by using sonic crystals a) schematic representation and b) experimental setup

In the experimental setup shown in **Figure 31**, a curved PVDF beam is placed in the cavity, and the acoustic wave is created by a wave generator (speaker). The peak harvested power for the device is in the range of nano watts, which is very low compared to piezoelectric devices.

3. Energy Harvesting Through Liquid State Transduction

Mechanism

In the second classification of fluidic energy harvesters, these types of energy harvesters have a liquid state energy capturing and energy transduction mechanism. The most common example is a ferrofluid sloshing based energy harvester [23], [43], [125], which is a special fluid

exhibiting super paramagnetism which allows the fluid to have a net magnetic moment in the presence of a strong magnetic field [126].

3.1 Ferrofluid Sloshing Based Energy Harvester

In recent years, there has been a push towards sustainable energy use and energy harvesting through micro-power generators, using waste energy from the environment. One approach to harvest energy is to convert the mechanical energy of ambient vibration into electrical energy by using various devices. This kind of vibration energy harvesting has been mainly done through solid state devices like the piezo-electrics, magneto-resistive materials, etc. Electromagnetic generators (EMG's) and Triboelectric Nano Generators (TENG's) are among the two most efficient solid-state energy harvesting techniques. EMG's work on Faraday's law of electromagnetic induction, while TENG's utilize the coupling of triboelectrification and electrostatic induction and are comparatively very new (i.e. 2012). There is however a growing curiosity for utilizing fluid-state energy harvesters, mainly the ones based on ferrofluids. These devices like EMG's are also based on Faraday's law of electromagnetic induction. As per Faraday's law, the change in magnetic flux produces a current in the coil

$$\varepsilon = -\frac{d\varphi_B}{dt} = \dot{B}$$

which can then be channeled into an electric load, where ε is the electromotive force and φ_B is the magnetic flux. The solid-state nature of the transduction mechanism in current vibration energy harvesters can place limitations on their capabilities especially in terms of conformability to different shapes and sensitivity to a broadband of external excitations.

However, due to their un-restricted modal frequencies, and because of the ability of ferrofluids (in general any fluid) to have closely packed modal frequencies, ferrofluid based vibration energy harvesting has become attractive [127]. Ferrofluids consist of stable ferrous nanoparticles

in colloidal suspension forming nanoscale permanent magnetic dipoles[9], [11] once they are subjected to an external magnetic field. Each magnetic dipole is coated with a surfactant such that, in the absence of an external magnetic field, the magnetic dipoles are randomly oriented in the carrier fluid, and do not coagulate due to the fields generated by the ferromagnetic cores. However, when an external magnetic field is applied, the average direction of the fluid magnetization becomes parallel to the magnetic field lines. As shown in **Figure 32**, the orientation of the magnetic dipoles, (which is quite analogous to that of a piezoelectric, in which we see a rotation of electric dipoles with electric field) relative to the magnetic flux lines depends on the strength of the applied magnetic field.

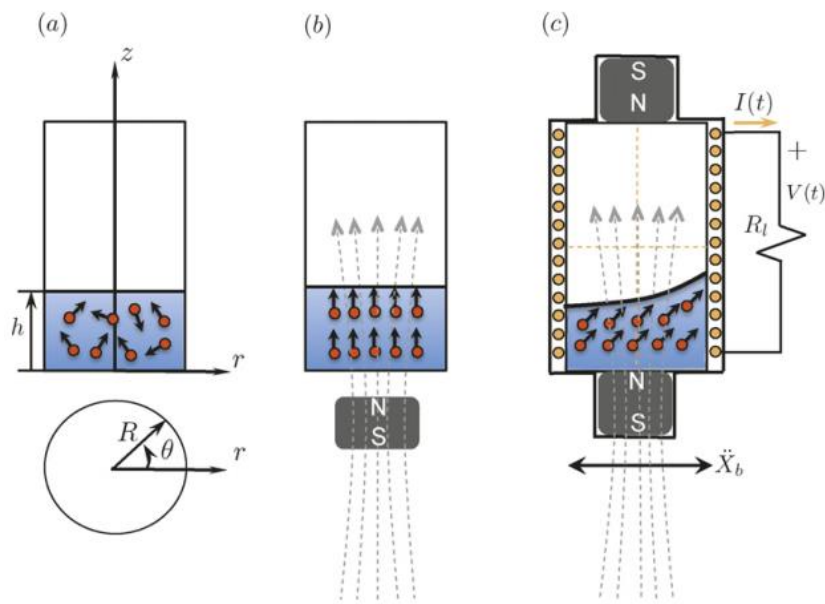


Figure 32 A Cylindrical Ferrofluid based Vibration Energy Harvester [23]

Thus, in a weak magnetization (M) region (low field strength, although magnetization also depends upon susceptibility χ), the magnetic field has little influence on the direction of the dipoles, whereas, within the highly-magnetized regions, the dipoles are strongly coupled to the applied field, and, are hence very difficult to rotate against the high magnetic force. Hence, there needs to be a stable enough external magnetic field which orients the dipoles but does not hold

them too tightly so that they do not rotate when external vibrations are applied. When the magnetized fluid is subjected to external excitations with a frequency that matches one of the infinite modal frequencies of the fluid column (resonance condition), large amplitude surface waves, both horizontal and rotational, can be excited. The motion of the sloshing liquid creates a time-varying magnetic flux which can then be used to induce an electromotive force in a coil adjacent to the container. This process generates an electric current, and therewith, transduces external vibrations into electric energy[128].

Figure 32 illustrates one such ferro-fluid based vibration energy harvester, which has a cylindrical container subject to base excitations, and a pick-up coil wrapped around it to induce the time varying magnetic field created at the surface into electric energy. A similar configuration is investigated in this project, where a rectangular container is subject to base excitations and the subsequent sloshing motion of ferrofluid is used to generate electricity. The authors of the cylindrical container harvester whose work is investigated further here, developed an analytical vibration-based solution, obtained through perturbation method, as a mathematical model for solving the liquid sloshing and the subsequent non-linear coupling between the modes[25], [128].

However, a Navier-Stokes equation-based approach would be much more suitable for this purpose, as it captures all the relevant forces in the domain with very high detail. A schematic representation of another such investigated configuration is presented in **Figure 33**.

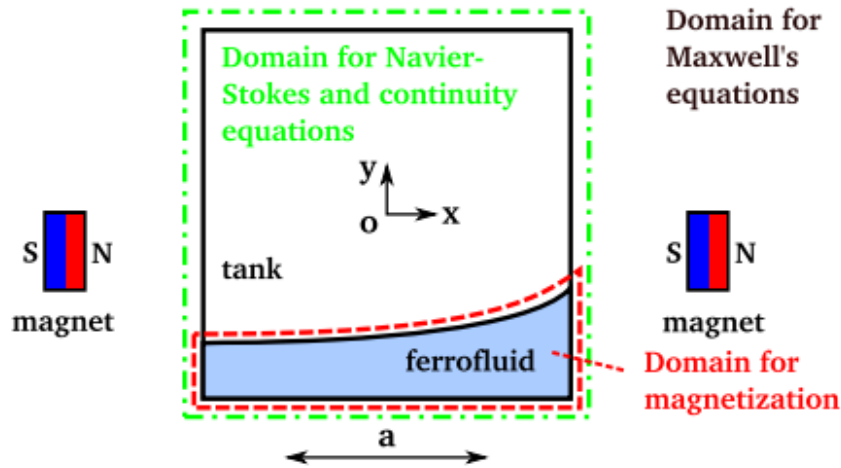


Figure 33 Schematic representation of a rectangular Ferrofluid sloshing tank for vibration energy harvesting [24]

The Navier Stokes equations are coupled with the Maxwell's equations, which determines the force exerted by the magnetic field on the fluid. In this work a Navier-Stokes equation-based approach is taken to solve for the sloshing dynamics.

In this part (part III) two different ferrofluid sloshing vibration energy harvesters are numerically modeled. The first configuration is that of a harvester with 4 magnets, placed symmetrically around the harvester, and the variation of efficiency of such a harvester is studied as a function of the significant length scale of the harvester and the polarity of the fixed magnets. The second configuration that is numerically modeled is that of a unique hybrid ferrofluid-piezoelectric sloshing-fluid structure interaction vibration energy harvester. Here the idea is to exploit the ferrofluid motion for two purposes, one is to harvest energy from ferrofluid motion by applying a non-uniform magnetic field, given an external excitation, and second to utilize the kinetic energy of the ferrofluid to impart stresses on an internal fixed piezoelectric bimorph which would in-turn generate power on its own. However, this study only includes a feasibility analysis and not an optimization of the system.

Chapter 2: Analysis of a Symmetrical Ferrofluid

Sloshing Vibration Energy Harvester

1. Introduction

Sloshing refers to the movement of liquids inside partially filled containers, by virtue of external excitation[129], [130]. It is characterized as an internal free surface flow. Sloshing has normally been an area of interest for the shipping industry, the automobile industry and intergalactic rocketry[129]. Most of these applications have tried to mitigate the effects of sloshing, because at large scales a sloshing fluid can cause significant structural damage to the container[131]. Therefore, most research pertaining to sloshing has been done to mitigate the effects of sloshing by use of baffles etc.,

However, recently a new use for sloshing has been developed, as mentioned in the previous chapter. Ferrofluid sloshing has been used for generating power from external oscillations. Performance characteristics of one such energy harvesting configuration was conducted and a plethora of knowledge regarding design rules for such a configuration were proposed[132].

In this chapter, a unique configuration for a ferrofluid vibration energy harvester (VEH) is proposed, which exploits the two symmetry planes of the harvester and introduces 4 symmetrically placed powerful magnets to generate 16 unique combinations of magnetic fields. The idea with symmetrical placement is that, it becomes easy to manufacture if the structures are symmetric. This can also make it a wearable energy harvester, which can serve the needs of growing power supply to the Internet of Things or other wearable devices.

Finally, the level-set method is introduced to capture the movement of the free surface. Although the level-set method has been used to perform numerical studies on ferrofluid droplets[133], [134], but it is believed that this is the first endeavor using level-set method for ferrofluid sloshing. The following chapters explain the proposed configuration and its performance in detail.

2. Geometry and setup

Figure 34 represents the configuration with four magnets symmetrically placed at the center planes of the harvesting tank. The four magnets have length dimensions in terms of the significant length scale (i.e. the length of the tank). The thickness of the magnets is a tenth that of the tank, and their width is a fifth that of the tank. Such a formulation helps in scaling the system with the actual length of the configuration.

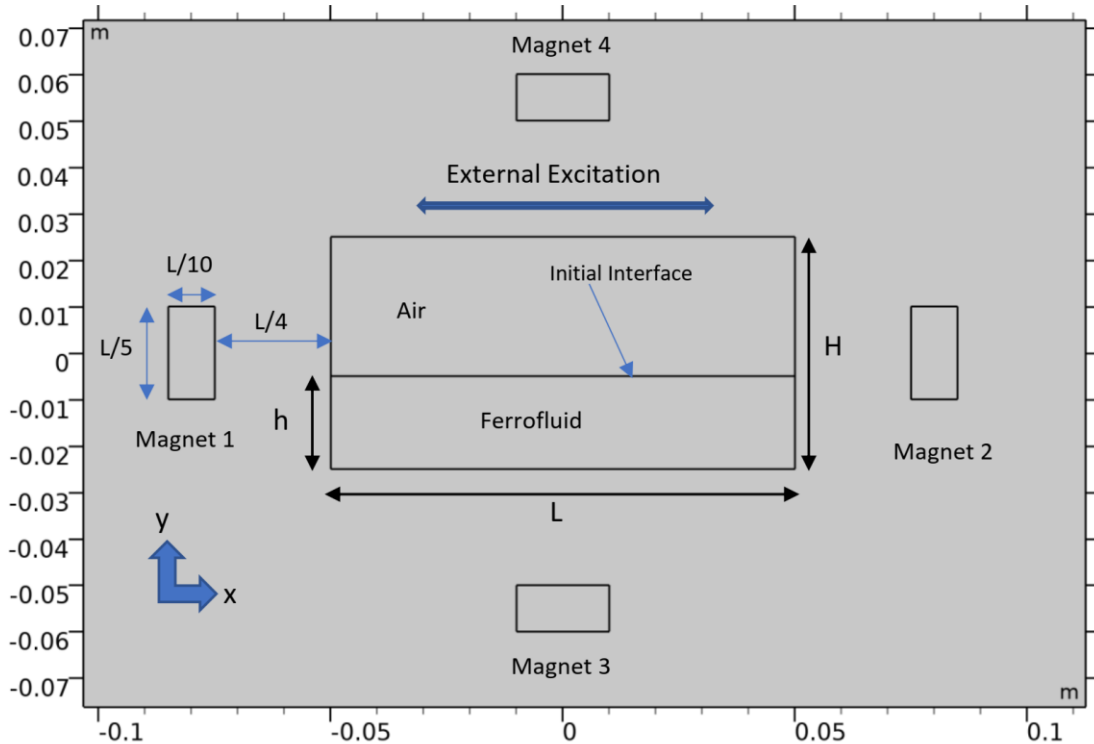


Figure 34 Schematic representation of the proposed harvester configuration

The magnets are placed at a distance of $L/4$ from their adjacent tank wall. The height of the tank (H) is half of its length, and the fill level of the ferrofluid in the tank is h . The magnets are labelled from 1 through 4.

In order for convergence of the magnetic field, a large domain is created around the harvester. This is shown in **Figure 35**, where the domain is 10 times larger than the length scale of the harvester. The harvester receives an external excitation which is periodic in nature and causes the ferrofluid to slosh inside.

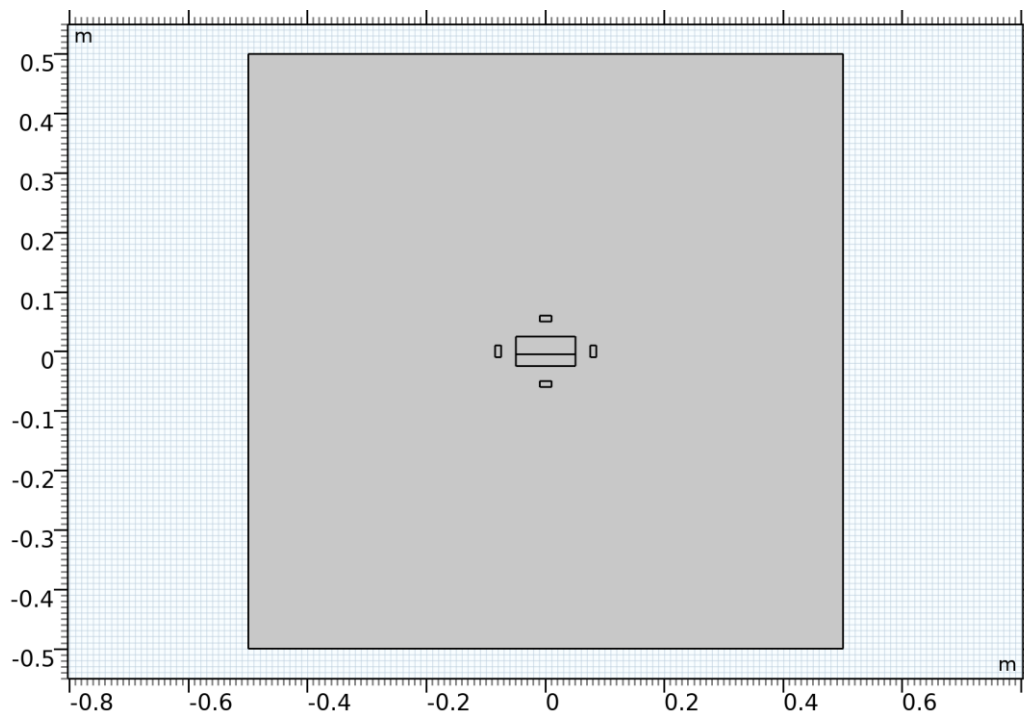


Figure 35 Harvester and the large domain surrounding it

3. Governing Equations

The flow inside the domain is governed by Navier Stokes equations and Maxwell's equations. The Navier-Stokes equations are as follows

Continuity:

$$\rho \nabla \cdot \vec{V} = 0 \quad (1)$$

Momentum:

$$\rho \frac{\partial \vec{V}}{\partial t} + \rho(\vec{V} \cdot \nabla)\vec{V} = -\nabla p + \mu \nabla^2 \vec{V} + \vec{F}_m + \rho \vec{g} + \vec{F}_{st} \quad (2)$$

where, \vec{V} is the velocity vector, \vec{F}_m is the magnetic force, \vec{g} is the external acceleration on the system which consists of the external excitation and the acceleration due to gravity, and \vec{F}_{st} is the force of the surface tension.

Here the external excitation is given as:

$$x = X_0 \sin(\omega t) \quad (3)$$

where X_0 is the amplitude of external excitation and ω the angular frequency, which is related to the excitation frequency f as, $2\pi f$. In this study f is varied such that the set of frequencies contain the first modal frequency. This makes the acceleration to be:

$$a_0 = -X_0 \omega^2 \sin(\omega t) \quad (4)$$

Since the flow is a separated two-phase flow, with an interface separating the two, the properties of the fluids will vary sharply across the interface. This needs to be accounted for by using an interface tracking method, which will keep the boundary between the fluids intact, and also allow the interface to advect with changing flow field. This requires a separate computation step and separate mathematical treatment/modeling of the moving interface. Several methods are very effective in performing interface tracking computationally, for instance, the Volume of Fluid method, the Level-set method, the phase field method etc.[135]. These methods usually work based on conservation of some physical or attributed numerical quantity, usually the mass or the area under the surface, or the gradient of the distance function etc. in order to characterize the free-surface. This then is used to derive a partial differential equation form of the conserved quantity and is solved with the N-S equations to yield the profile of the moving interface. One such method mentioned above is the level-set method[136]. In the level set method, the interface is defined as

a signed distance function, and is tracked as a higher dimensional field applied to the flow field, which in turn defines how the flow moves[137]–[139]. However, the level set method proposed initially[138] did not conserve mass or the area correctly, especially in fluid dynamics problems. This prompted further research into conservative level set methods which conserve the mass exactly. In this work one such method is used where the mass is conserved exactly, and the surface is expressed as a constant level set[140], [141]. Although, level set methods are inherently well suited for representing complex topologies, they become even more effective in tracking sharp interfaces with a conservative level-set formulation[142]–[144]. The mathematical formulation of this sharp-interface, conservative level-set method is shown below.

Level-set equations for interface tracking:

$$\frac{\partial \phi}{\partial t} + \vec{V} \cdot \nabla \phi = \gamma \nabla \cdot \left(\epsilon_{ls} \nabla \phi - \phi(1 - \phi) \frac{\nabla \phi}{|\nabla \phi|} \right) \quad (5)$$

where, ϕ is the level set variable, γ is the re-initialization parameter and ϵ_{ls} is the parameter which controls the thickness of the fluid-air interface. In this work the value of the re-initialization parameter is set to $X_0 \omega$ which is a characteristic velocity scale for the sloshing setup. The separating surface is given by $\phi = \phi_0 = 0.5$, i.e. a set of all surfaces where the level set function $\phi = 0.5$. This means that the first fluid is from $\phi = 0$ to $\phi = 0.5$ and the second fluid from $\phi = 0.5$ to $\phi = 1$. This level-set variable creates a higher dimensional field over the flow field and describes all the properties of the two fluids in its terms, in order to represent the separation between the two fluids as a sharp interface. All fluid properties must be represented in terms of the level set variable, in order to fully couple the flow field with the level-set field. Similarly, all interfacial forces must be expressed in terms of the level-set variable.

The surface tension force is expressed in terms of the level-set variable as follows:

$$\vec{F}_{st} = \sigma_m \delta \kappa \mathbf{n}_i + \delta \nabla_s \sigma_m \quad (6)$$

where, σ_m is the surface tension coefficient, δ is a Dirac delta function located at the interface, κ is the curvature of the surface, \mathbf{n}_i is the normal vector of the liquid-gas interface, and ∇_s is the surface gradient operator.

The interface normal is given by:

$$\mathbf{n}_i = \frac{\nabla\phi}{|\nabla\phi|} \quad (7)$$

The Dirac delta function is given by:

$$\delta = 6 |\nabla\phi| |\phi(1 - \phi)| \quad (8)$$

The curvature of the surface is given by:

$$\kappa = -\nabla \cdot \mathbf{n}_i \quad (9)$$

The surface gradient operator is given by:

$$\nabla_s = (I - \mathbf{n}_i \mathbf{n}_i^T) \nabla \quad (10)$$

Also, the angle that the fluid makes with the wall while wetting is assumed to be 90° . This is a standard assumption for solving sloshing flows[25].

For the fluid domain inside the tank the properties must be expressed in terms of the level set variable. Density is given as:

$$\rho = \rho_1 + (\rho_2 - \rho_1)\phi \quad (11)$$

Viscosity is given as:

$$\mu = \mu_1 + (\mu_2 - \mu_1)\phi \quad (12)$$

where the indices 1 and 2 denote fluid 1 and fluid 2, which in our case is the ferrofluid and air, respectively. Similarly, to calculate the Kelvin body force, the magnetic properties of the fluids must be expressed in terms of the level set variable:

$$\vec{F}_m = \vec{M} \cdot \nabla \vec{H} \quad (13)$$

where, \vec{H} is the magnetic field, and the magnetization \vec{M} is given by the constitutive relation:

$$\vec{M} = \chi_m \vec{H} \quad (14)$$

where, χ_m is the magnetic susceptibility and is obtained from the level set function for the whole domain as:

$$\chi_m = \chi_{m1} + (\chi_{m2} - \chi_{m1})\phi \quad (15)$$

Maxwell's conservation laws for the system are[11]:

$$\nabla \cdot \vec{B} = 0 \quad (16)$$

$$\nabla \times \vec{H} = 0 \quad (17)$$

$$\nabla \times \vec{E} = -\frac{\partial \vec{B}}{\partial t} \quad (18)$$

also, the magnetic field can be written as:

$$\vec{H} = -\nabla V_m \quad (19)$$

where, V_m is the magnetic scalar potential.

The boundary conditions for the domain are the no flux boundary condition for the ends of the domain surrounding the harvester. The magnets are such that they have a uniform magnetization of 400 kA/m. The following are the constitutive relations for different regions:

$$\vec{B} = \mu_0 \vec{H} \text{ (for air)}; \vec{B} = \mu_0(\vec{H} + \vec{M}_s) \text{ (for the magnets)} \& \vec{B} = (1 + \chi_m)\vec{H} \text{ for sloshing}$$

The electromotive force from sloshing is picked up by an external coil with N turns (which are varied in order to optimize power harvested). The electromotive force is given as:

$$\epsilon = -N \frac{d\Phi}{dt} \quad (20)$$

where, Φ is the magnetic flux, obtained by integrating the magnetic flux density over the area.

The electromotive force due to the changing magnetic field inside the harvester is picked up by an external coil, which can be wound either along the length of the harvester and gets pitched in the y direction, or it can be wound either along the height of the tank while pitched along the x

direction. Equation 21 represents the expression of Inductance of one such rectangle, where μ_r is the relative permeability of the material enclosed in the coil.

$$L_{rect} = N^2 \frac{\mu_0 \mu_r}{\pi} \left[-2(W + H) + 2\sqrt{H^2 + W^2} - H \ln \left(\frac{H + \sqrt{H^2 + W^2}}{W} \right) - W \ln \left(\frac{W + \sqrt{H^2 + W^2}}{H} \right) + H \ln \left(\frac{2H}{d} \right) + W \ln \left(\frac{2W}{d} \right) \right] \quad (21)$$

The current in the wound coil can be found by the series L-R circuit equation:

$$L_c \frac{di}{dt} + i (R_L + R_c) = V \quad (22)$$

where R_L is the load resistance and R_c the coil resistance, through which the power output of the harvester is measured, $L_c = L_{rect}$ is the inductance of the wound coil, and V is the electromotive force obtained from sloshing. Finally, it is assumed that if a coil is wound along the length (i.e. horizontally wound) the number of turns would be half that of when it is wound along the height (i.e. vertically wound coil). It must be noted that for vertical winding (along height) the x component of the magnetic flux would be used, and for horizontal winding (along length) the y component of the magnetic flux would be used for calculation of the electromotive force.

4. Numerical Modeling and Validation

In this chapter the numerical modeling details are discussed. The combined Navier-Stokes and Maxwell equations are solved in COMSOL Multiphysics using its inbuilt multiphysics capacity. As discussed earlier, COMSOL is a finite element-based software, which solves partial differential equations using the weak form and shape functions. For computational fluid dynamics applications, especially where Navier Stokes Equations are involved, finite element-based codes need to account for stability errors in the cross wind and streamline direction due to numerical

dispersion. This is especially significant when velocity and pressure fields are resolved by same order of elements. These stabilizations are inbuilt in COMSOL and are based on Streamline upwinding methods for both pressure and velocity fields[145], [146]. Further, as the problem is unsteady, the solution must be marched in time, to obtain the state of the system at each time of interest during the simulation. For this an implicit adaptive time stepping scheme is used.

The solution is advanced by solving segregated steps at each time step when the tolerance level (which is set to be $1e-4$) is reached. This convergence criteria is for both solution and the residual. The following segregated steps of dependent variables are solved in the following order:

- a) Level set variable
- b) Velocity and pressure
- c) Magnetic scalar potential.

In order to simplify and streamline the computations, first order discretization is used for the pressure and velocity fields. Similarly, for the level set variable linear elements are used. For the magnetic scalar potential, the element order is maintained at 2 everywhere in the domain.

Grid convergence studies and adaptive time step control studies were performed on two magnet configurations, and it was found that the mesh inside the sloshing domain is both, accurate and efficient for a grid size of 0.001 and for a maximum time step value of 2 milliseconds.

To validate COMSOL and the level set method used in the computations, a comparative study was run replicating the published experimental and computational results by Liu et al[24]. The combination 1H is simulated and the results are compared in **Figure 36**. The predictions from the numerical scheme adapted in the present work match very closely to the reported computational and experimental data in [24] as shown in **Figure 36 b) and a)** respectively. The peak voltage near the resonance frequency almost matches perfectly with the experimental data. However, since the

spectrum of frequencies in the frequency sweep performed in present work is not as closely spaced as reported by Liu et al, the internal energy pump, which occurs at around 1.5 Hz is not as prominent in our simulation of their configuration as shown in **Figure 36 b)**.

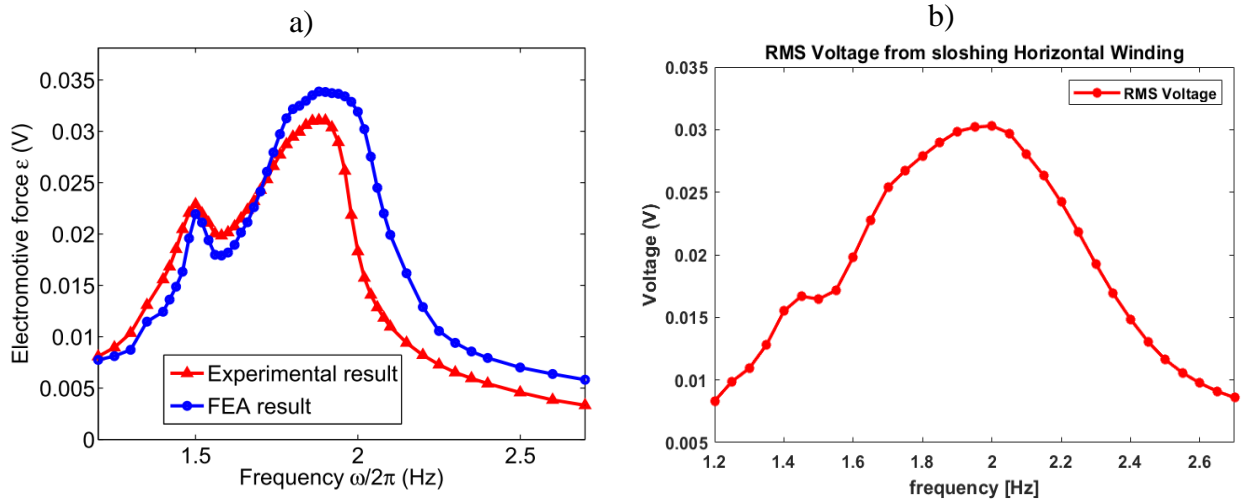


Figure 36 Comparison between a) 1H configuration of Liu[24] and b) present work

Based on this validation, it is inferred that the level-set formulation and the solvers chosen are capable of simulating the complexities involved in this flow. To advance the work on ferrofluid VEH a new tank design is proposed in this work, as mentioned in previous sections. This configuration is then subjected to a frequency sweep, with an array of combinations between the four fixed magnets, in which the north and south poles of one or more magnets are flipped to generate a new magnetic field distribution.

Table 7 lists all the 16 cases which may arise with different combinations of north and south pole orientations of the magnets. The table lists South/North labels for the magnets, which depicts which pole of the magnet is facing the tank.

Two tanks are studied, one where L is 10 cm and other where L is 5 cm. The fill level is a fraction of the length scale and is set to be L/5. For the two tanks the frequency sweep is performed in such a way that the first resonance frequency is captured within the sweep.

Finally, to maintain energy application parity across tank sizes and frequencies, the external acceleration (a) is kept as constant, equal to 1 m/s^2 .

i.e. $a = X_0\omega^2 = 1$.

Hence when the frequency changes, the amplitude is adjusted in order to keep the acceleration constant.

Table 7 Cases for Magnet orientation

Case	Magnet 1	Magnet 2	Magnet 3	Magnet 4
1	South (k1=-1)	North (k2 = -1)	South (k3 = -1)	North (k4 =-1)
2	South (k1=-1)	North (k2 = -1)	South (k3 = -1)	South (k4 =1)
3	South (k1=-1)	North (k2 = -1)	North (k3 = 1)	North (k4 =-1)
4	South (k1=-1)	North (k2 = -1)	North (k3 = 1)	South (k4 =1)
5	South (k1=-1)	South (k2 = 1)	South (k3 = -1)	North (k4 =-1)
6	South (k1=-1)	South (k2 = 1)	South (k3 = -1)	South (k4 =1)
7	South (k1=-1)	South (k2 = 1)	North (k3 = 1)	North (k4 =-1)
8	South (k1=-1)	South (k2 = 1)	North (k3 = 1)	South (k4 =1)
9	North (k1=1)	North (k2 = -1)	South (k3 = -1)	North (k4 =-1)
10	North (k1=1)	North (k2 = -1)	South (k3 = -1)	South (k4 =1)
11	North (k1=1)	North (k2 = -1)	North (k3 = 1)	North (k4 =-1)
12	North (k1=1)	North (k2 = -1)	North (k3 = 1)	South (k4 =1)
13	North (k1=1)	South (k2 = 1)	South (k3 = -1)	North (k4 =-1)
14	North (k1=1)	South (k2 = 1)	South (k3 = -1)	South (k4 =1)
15	North (k1=1)	South (k2 = 1)	North (k3 = 1)	North (k4 =-1)
16	North (k1=1)	South (k2 = 1)	North (k3 = 1)	South (k4 =1)

5. Results and Discussion

In this section, simulation results and the performance of the two energy harvesters are discussed. The two combinations are subjected to an impedance matching as well by solving equation 22. Matching impedance allows for the calculation of the maximum power that can be achieved in form of a resistive load on the system. The next two subsections deal with the two tanks.

5.1 Analysis of output from L = 10 cm tank

Figure 37 shows how the ferrofluid moves inside the tank at near the resonance frequency, for the magnet combination case 1. The rest of the 15 cases are displayed in Appendix A.

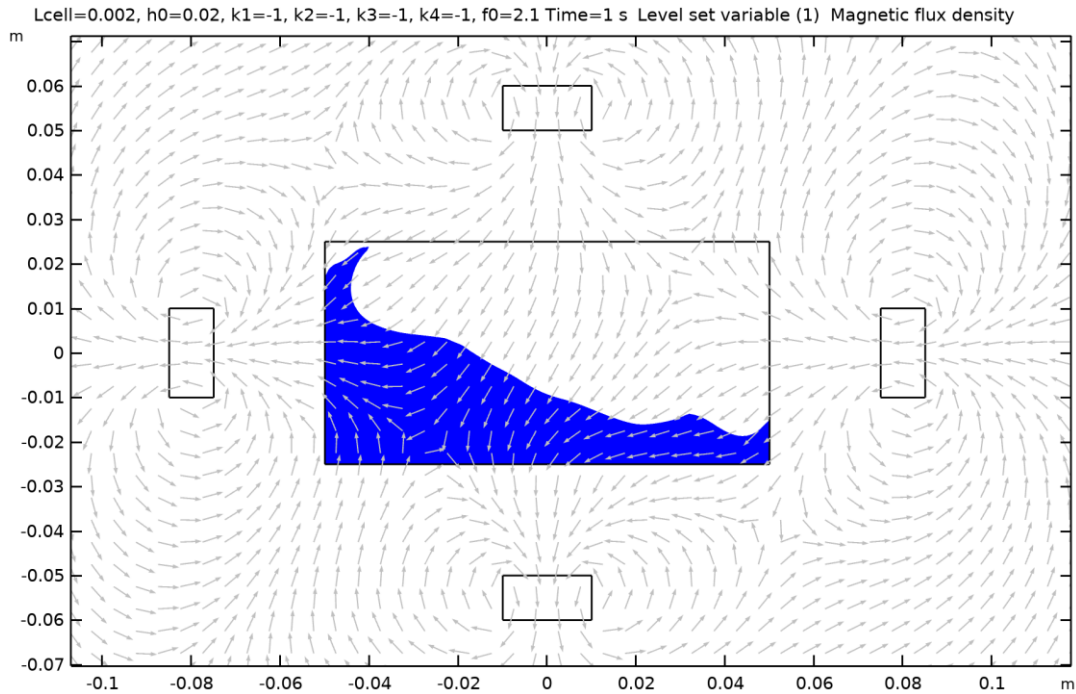


Figure 37 Surface evolution and magnetic flux density arrow surface for case 1, near resonance frequency for L=10 cm tank

The arrows in the above plot depicts the magnetic flux lines. The flux lines in a magnet originate from the north pole and terminate into the south pole. In the above plot, magnet 1's south pole is facing the harvester, while magnet 2's north, magnet 3's south and magnet 4's north, face the harvester. Now, for each of these 16 cases of magnet arrangement, a frequency sweep is performed. Each frequency sweep produces a voltage signal from the harvester. This is then transformed into RMS voltage, in order to quantify the performance characteristics of the harvester. Now in order to study the maximum performance that the harvester is capable of, nine coils are modeled with different number of turns. Also, the power harvested from the harvester cannot be the power that goes directly to the pick-up coil. A load resistor is attached to the circuit,

and the power through the load resistance is calculated in order to measure the performance of the harvester. This forms a series L-R circuit, and equation (20)-(22) are used to model this circuit. Secondly, in order to check the maximum power output in the load resistor for the same temporal variation in magnetic flux density, 25 load resistors are modeled. These resistors combined with 9 coils are used to estimate peak voltage (RMS) and peak power output (RMS). These two outputs are not necessarily linked to each other, as in, the peak power may or may not correspond to the peak voltage reported. This is done in order to analyze the voltage and power output potential from the two tanks separately. Of course, the ultimate performance can only be analyzed through the power output from the system, however, that is also a function of the kind of circuit one builds to harvest the energy from the system. In our case it is a series L-R circuit represented by equation 22. The calculation of the coil resistance is based on the number of turns the pickup coil has. The coil material is chosen to be Copper. **Table 8** summarizes the properties of the pick-up coils modeled for $L = 10\text{cm}$ tank.

Table 8 Summary of properties of coils for $L = 10\text{ cm}$ tank

Coil number	Number of turns	Resistance of horizontal coil (ohm)	Resistance of vertical coil (ohm)	Inductance of horizontal coil (H)	Inductance of vertical coil (H)
1	100	3.422	0.64	0.0083	0.0050
2	200	27.38	5.13	0.038	0.023
3	400	219.04	41.07	0.17	0.10
4	500	427.81	80.21	0.27	0.17
5	800	1752.30	328.55	0.75	0.47
6	1000	3422.47	641.71	1.20	0.77
7	1200	5914.02	1108.88	1.77	1.14
8	1500	11550.83	2165.78	2.85	1.84
9	2000	27379.74	5133.70	5.25	3.42

The coil properties are calculated by assuming that the tank depth is 10 cm and both the coils envelop the length along the winding direction completely. This gives the coil diameter for

the horizontal coil as $\frac{H}{N}$ and for the vertical coil as $\frac{L}{N}$, where H is the height of the tank and L is the length of the tank. The tank depth is maintained to be equal to the largest dimension of the tank, in order to discount 3-D effects on the 2-D simulation performed in this study. In order to calculate the inductance of the coil from equation (21) the relative permeability is calculated by taking a weighted average of the relative permeabilities of the ferrofluid and the air. This comes out to be 2, considering air as 1 and ferrofluid as 4.52 ($1 + \chi_m$). Finally, to check the power output performance of each coil 25 load resistors (R_L) are used, which is usually known as impedance matching. The load resistances are varied from 1 to 10^5 ohms, with an increment of $10^{0.25}$ ohms. This covers the total range of coil resistances shown in Table 8.

From **Figure 38** the performance as measured by max RMS voltage output is displayed

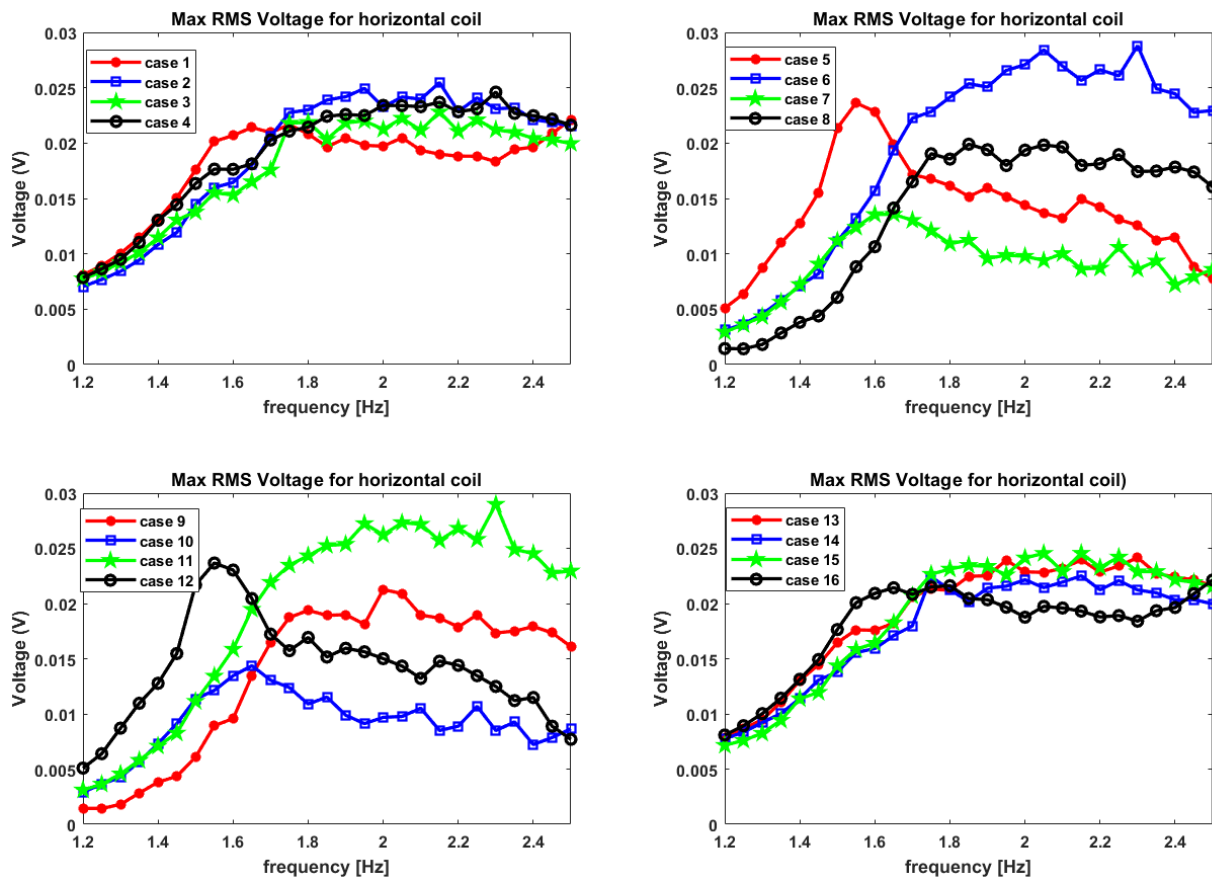


Figure 38 RMS voltage plots for Cases 1-16 while considering horizontally wound coil for $L = 10$ cm tank

when a horizontally wound coil is used for voltage pickup from the tank. These plots are for all the 16 magnet configurations, and almost all the cases have low voltages, and have almost the same range. The max voltage noted is around 0.03 V and it is from magnet case 6 and magnet case 11, both seem identical. It must be noted that the cases seem to be symmetric in their behavior, hence making a pair of 8 cases, which must be true for an oscillatory motion. The RMS voltages are calculated after the first two time periods have elapsed, at which point it is assumed that the system has equilibrated from the initial jerk which propels the system in an oscillatory motion. The simulations were run for 5 time periods, and hence the RMS quantities used are from the last 3 time periods.

For, vertical winding the RMS voltages are shown in **Figure 39**. They are an order of

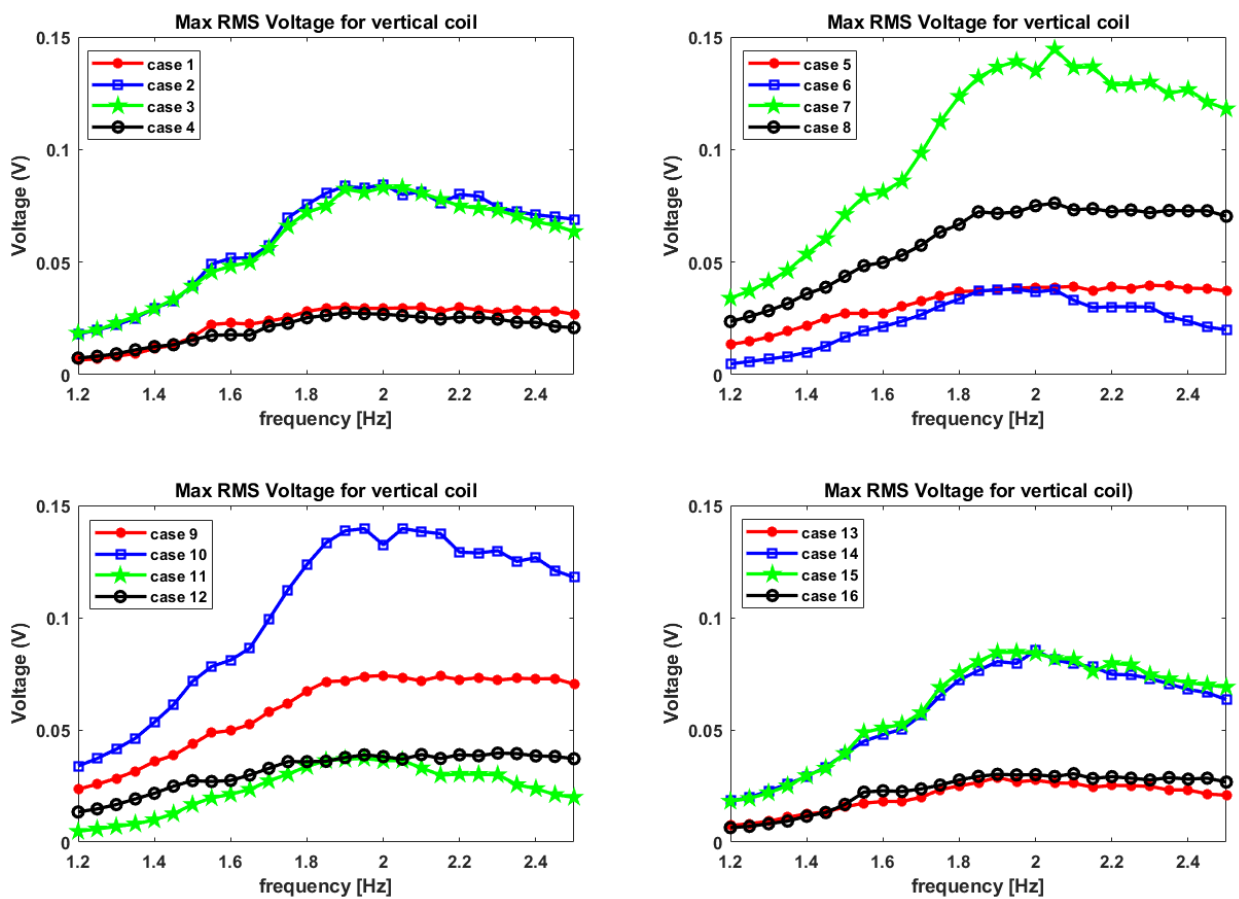


Figure 39 RMS voltage plots for Cases 1-16 while considering vertically wound coil for L=10 cm tank

magnitude higher than the horizontal ones. Cases 7 & 10 achieved the highest RMS voltage output of around 0.15V. Upon close observation cases 7 & 10 look very similar to each other solely from the point of view of the placement of magnets. This is similar to what was observed for max RMS voltages for horizontal coil. This can be attributed to symmetric magnet placement in cases 7 & 10, and all the other pairs of cases. The symmetric magnet placement gives rise to magnetic field profiles inside the tank which are mirror images of each other, which can be deduced from the direction of the magnetic flux lines for these two cases. Secondly, it is observed that there is a secondary peak near 1.5 Hz in for both the horizontal and vertical windings. This is due to the internal coupling between modes, generating a non-linear internal energy pump[25], [128]. The peak is smeared off because the frequencies in our sweep are equidistant from each other.

In order to determine the power through the load resistor the RMS current is calculated by solving for instantaneous current from equation (22) for all the 9 coils and 25 load resistors. Then the RMS value of this current is taken and power through the load resistance is calculated using $I_{rms}^2 \times R_L$ using the value of rms current pertaining to that particular load resistor and that particular coil. Then the maxima of the power output for the above 225 cases (i.e. 9 coils and 25 load resistors) is taken for each of the 16 cases of magnet arrangements and all the 27 frequencies. In **Figure 40** the maximum power through the horizontal winding for all the 16 cases and all the 27 frequencies is plotted. The maximum power obtained is 0.15 micro-watts (μW) or $0.015 \left(\frac{\mu W}{g} \right)$ for case 6 and case 11. Here too the symmetry observed for the max voltages is evident. The maximum power value is obtained for a frequency of 2.3 Hz, which points towards the shifting of peak from the first modal frequency of 2.0865 Hz. This can be attributed to the magnetic body force exerted on the fluid in the y direction, and since the magnetic field in the y direction is considered for electromotive force through the horizontal winding, the shift in the occurrence of

the peak power output from the modal frequency is very evident. Hence the frequency for peak power shifts to the right of the modal frequency for the horizontal winding.

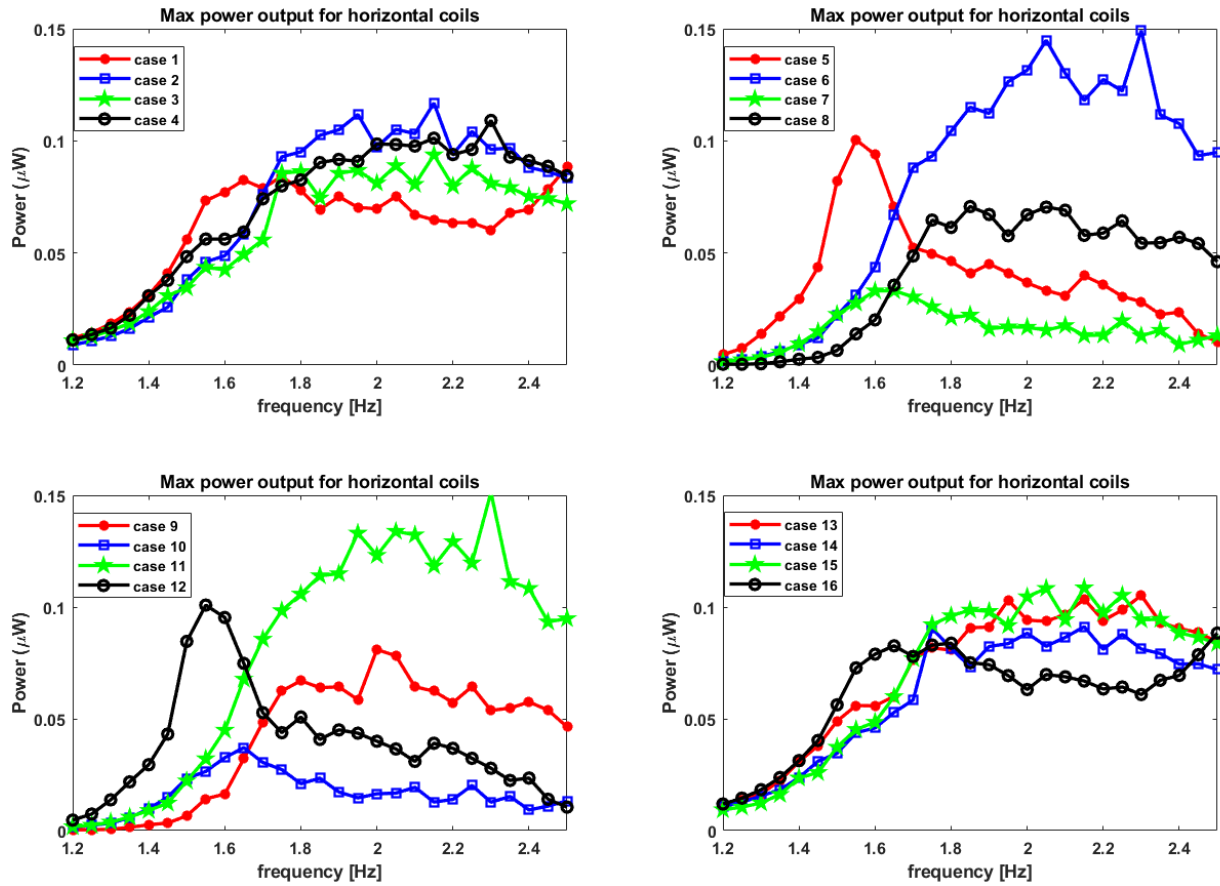


Figure 40 Maximum power output from horizontal coil for $L = 10$ cm tank

For the vertical coil, the max RMS power is for all the 27 frequencies and 16 magnet cases is plotted in **Figure 41**. The maximum power is obtained at 2.05 Hz for case 7 and is almost near to 20 micro-watts (μW) or $2 \left(\frac{\mu\text{W}}{g} \right)$, which is two orders of magnitude higher than that from the horizontal coils. It must be noted that the frequency where the max power output is observed is almost near to the modal frequency of 2.0865 Hz. The shift in the peak occurs towards the left from the modal frequency and is very small as compared to that in the horizontal winding case. This can be attributed to the fact that the output voltage for the vertical coil is a function of the magnetic field in the x direction. The range of the max power extracted using different magnet

configurations is very high. The max power out is as low as a $0.5 \text{ } (\mu\text{W})$ to the peak of $20 \text{ } (\mu\text{W})$. This indicates that placing magnets around the tank in a certain way facilitates the power output. It must be restated that the position of the magnets relative to the tank does not change, only the polarity changes. With that change almost two orders of magnitude of difference is observed in the max power harvested from the vertical winding of the device. This is also true for the horizontal winding case, but the gap between the lowest and highest max powers extracted is not as high as in the case of vertical winding. This provided additional design rules, to harness this work into enhancing designs for ferrofluid sloshing vibration energy harvesting systems.

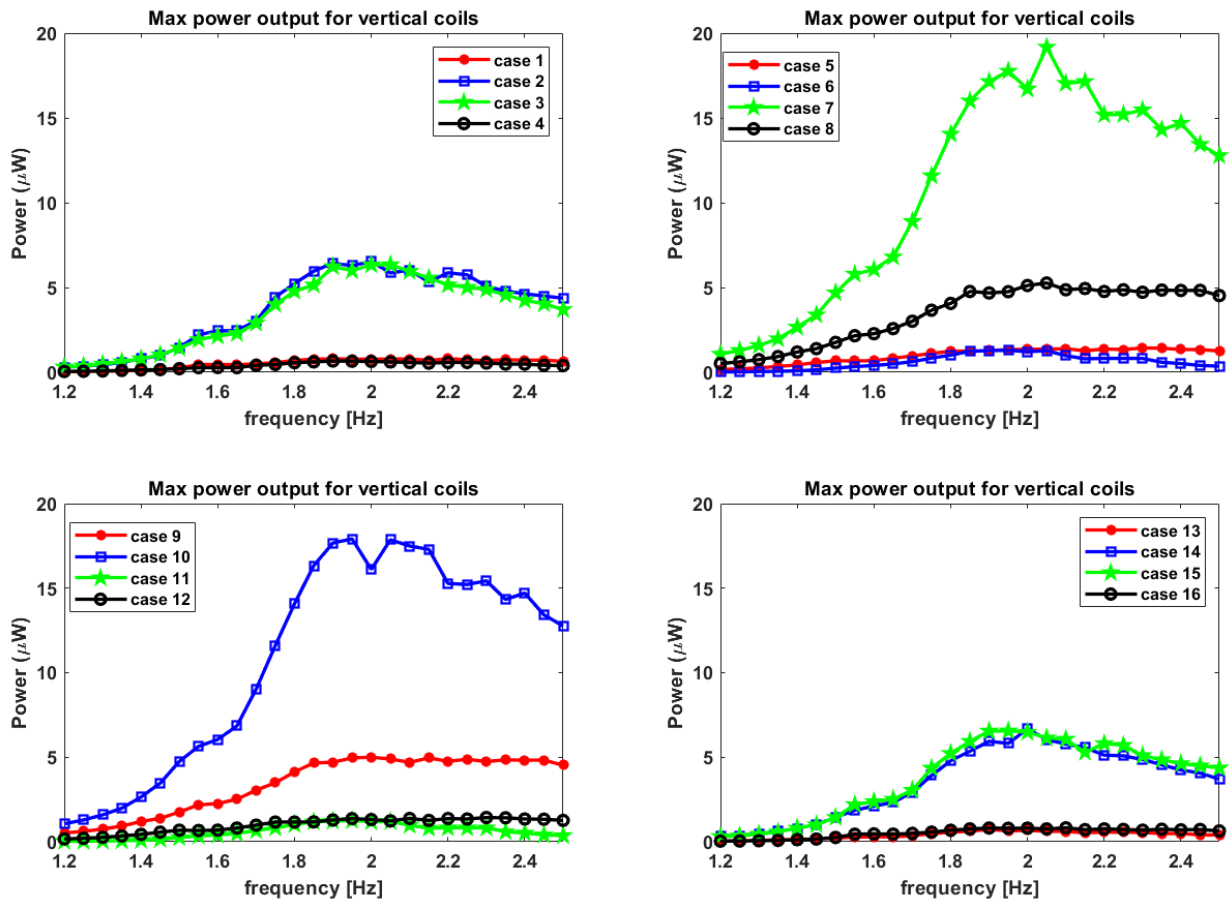


Figure 41 Maximum power output from vertical coil for $L = 10 \text{ cm}$ tank

5.2 Analysis of Output from $L = 5$ cm tank

In this subsection, the tank which is half the length of the previously discussed tank is studied. For this tank, the frequencies are varied from 2.2 Hz to 3.5 Hz, which passes through the first modal frequency of 2.96 Hz. The 16 cases of magnet configuration as mentioned in orientation remain the same. Since, all the dimensions on the system are parametrized by the length scale L , the length of the whole system becomes half of what it was for the tank studied earlier. This way the present system becomes identical to the previous tank but with change in the significant length scale. **Figure 42** illustrates the surface evolution of the ferrofluid for case 1, for frequency nearest to resonant frequency. For case 1, the north face of magnet 2 and 4 face the tank while the south face of magnet 1 and 3 face the tank. The plots for other 15 cases are placed in Appendix A.

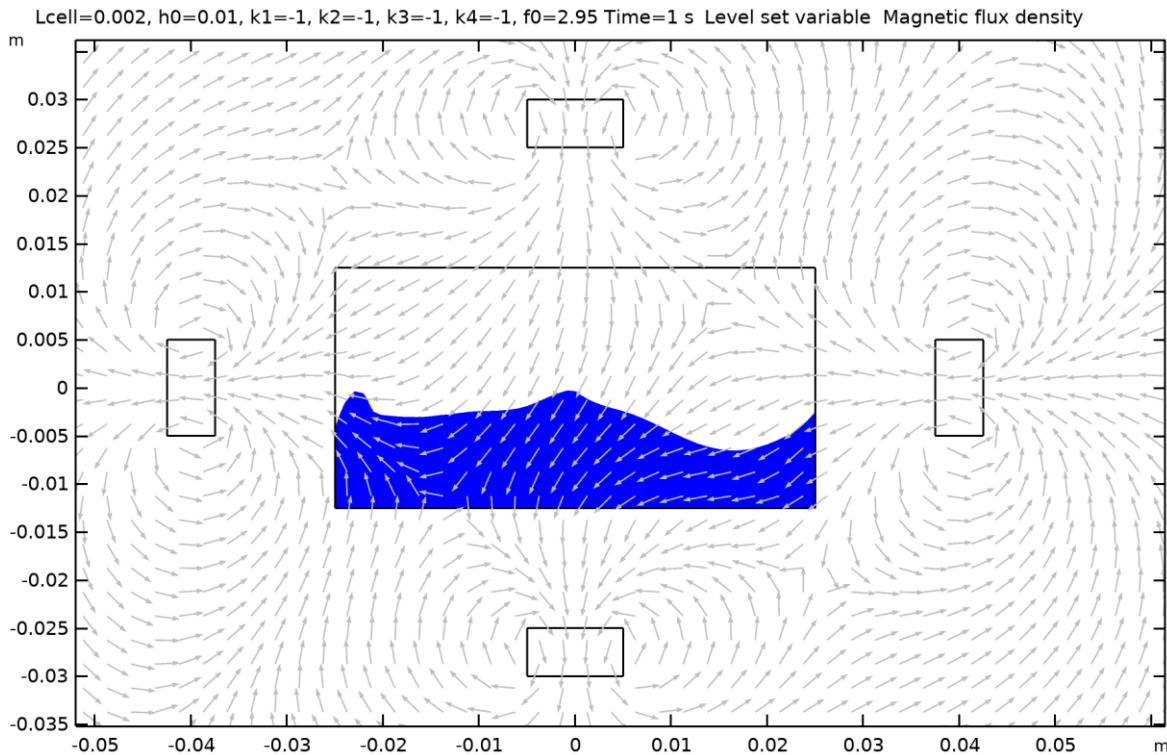


Figure 42 Surface evolution and magnetic flux density arrow surface for case 1, near resonance frequency for $L = 5$ cm tank

Now, for each of these 16 cases of magnet arrangement, a frequency sweep is performed. Each frequency sweep produces a voltage signal from the harvester. This is then transformed into RMS voltage, in order to quantify the performance characteristics of the harvester. Now in order to study the maximum performance that the harvester is capable of, nine coils are modeled with different number of turns. Also, the power harvested from the harvester cannot be the power that goes directly to the pick-up coil. A load resistor is attached to the circuit, and the power through the load resistance is calculated in order to measure the performance of the harvester. This forms a series L-R circuit, and equation (20)-(22) are used to model this circuit. Secondly, in order to check the maximum power output in the load resistor for the same temporal variation in magnetic flux density, 25 load resistors are modeled. These resistors combined with 9 coils are used to estimate peak voltage (RMS) and peak power output (RMS). These two outputs are not necessarily linked to each other, as in, the peak power may or may not correspond to the peak voltage reported. This is done in order to analyze the voltage and power output potential from the two tanks separately. Of course, the ultimate performance can only be analyzed through the power output from the system, however, that is also a function of the kind of circuit one builds to harvest the energy from the system. In our case it is a series L-R circuit represented by equation 22. The calculation of the coil resistance is based on the number of turns the pickup coil has. The coil material is chosen to be Copper. **Table 9** summarizes the properties of the pick-up coils modeled for $L = 5$ cm tank. Since, the dimension of the tank is halved, the resistance values and the inductance values of the 9 coils will also change. The only constants here is the number of turns in the coils and the properties of the magnets used. The coil properties are calculated by assuming that the tank depth is 5 cm, i.e. equal to the length (same as for $L = 10$ cm tank) and both the coils (Horizontal and Vertical) envelop the length along the winding direction completely. This gives

the coil diameter for the horizontal coil as $\frac{H}{N}$ and for the vertical coil as $\frac{L}{N}$, where H is the height of the tank and L is the length of the tank. In order to calculate the inductance of the coil from equation (21) the relative permeability is calculated by taking a weighted average of the relative permeabilities of the ferrofluid and the air. This comes out to be 2, considering air as 1 and ferrofluid as 4.52 ($1 + \chi_m$). Finally, to check the power output performance of each coil 25 load resistors (R_L) are used, which is usually known as impedance matching. The load resistances are varied from 1 to 10^5 ohms, with an increment of $10^{0.25}$ ohms.

Table 9 Summary of properties of coils for $L = 5$ cm tank

Coil number	Number of turns	Resistance of horizontal coil (ohm)	Resistance of vertical coil (ohm)	Inductance of horizontal coil (H)	Inductance of vertical coil (H)
1	100	6.84	1.28	0.0042	0.0025
2	200	54.76	10.27	0.019	0.012
3	400	438.07	82.14	0.084	0.053
4	500	855.62	160.43	0.13	0.086
5	800	3504.61	657.11	0.37	0.24
6	1000	6844.93	1283.43	0.60	0.39
7	1200	11828.05	2217.76	0.89	0.57
8	1500	23101.66	4331.56	1.43	0.92
9	2000	54759.48	10267.40	2.63	1.71

From **Figure 43** the performance as measured by max RMS voltage output is displayed when a horizontally wound coil is used for voltage pickup from the tank. These plots are for all the 16 magnet configurations, and almost all the cases have low voltages, and have almost the same range. The max voltage noted is around 0.008 V and it is from magnet case 6 and magnet case 11, like in the case of $L = 10$ cm tank. However, the harvested voltage is an order of magnitude smaller as compared to the previous tank. It must be noted that the cases seem to be symmetric in their behavior, hence making a pair of 8 cases, as was observed in the previous tank. The RMS voltages are calculated after the first two time periods have elapsed, at which point it is assumed that the

system has equilibrated from the initial jerk which propels the system in an oscillatory motion. The simulations were run for 5 time periods, and hence the RMS quantities used are from the last 3 time periods.

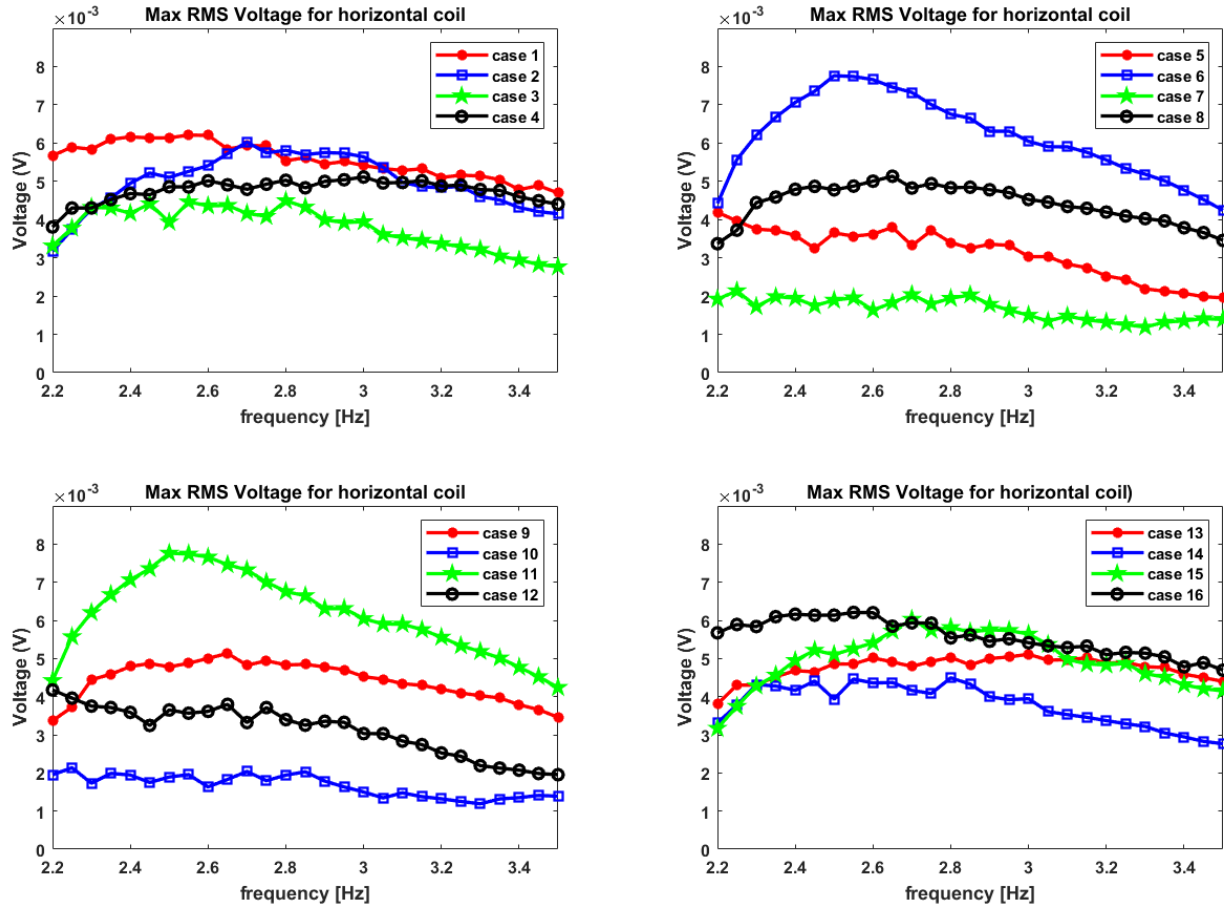


Figure 43 RMS voltage plots for Cases 1-16 while considering horizontally wound coil for L=5 cm tank

For, vertical winding the RMS voltages are shown in **Figure 44**. They are an order of magnitude higher than the max RMS voltage for horizontal coil, as was observed for L = 10 cm tank. Cases 7 & 10 achieved the highest RMS voltage output of around 0.038 V. The symmetric magnet placement in cases 7 & 10 causes for the max RMS voltage observed to be identical. As mentioned in the previous sub-section the symmetric magnet placement gives rise to magnetic field profiles inside the tank which are mirror images of each other, which can be deduced from the direction of the magnetic flux lines for these two cases. Similarly, this applies to other 14

configurations as well, where it can be observed from the plots of the voltages and power, that there are 8 pairs of cases which show identical behavior. This would be true for any such system subjected to oscillatory external excitation.

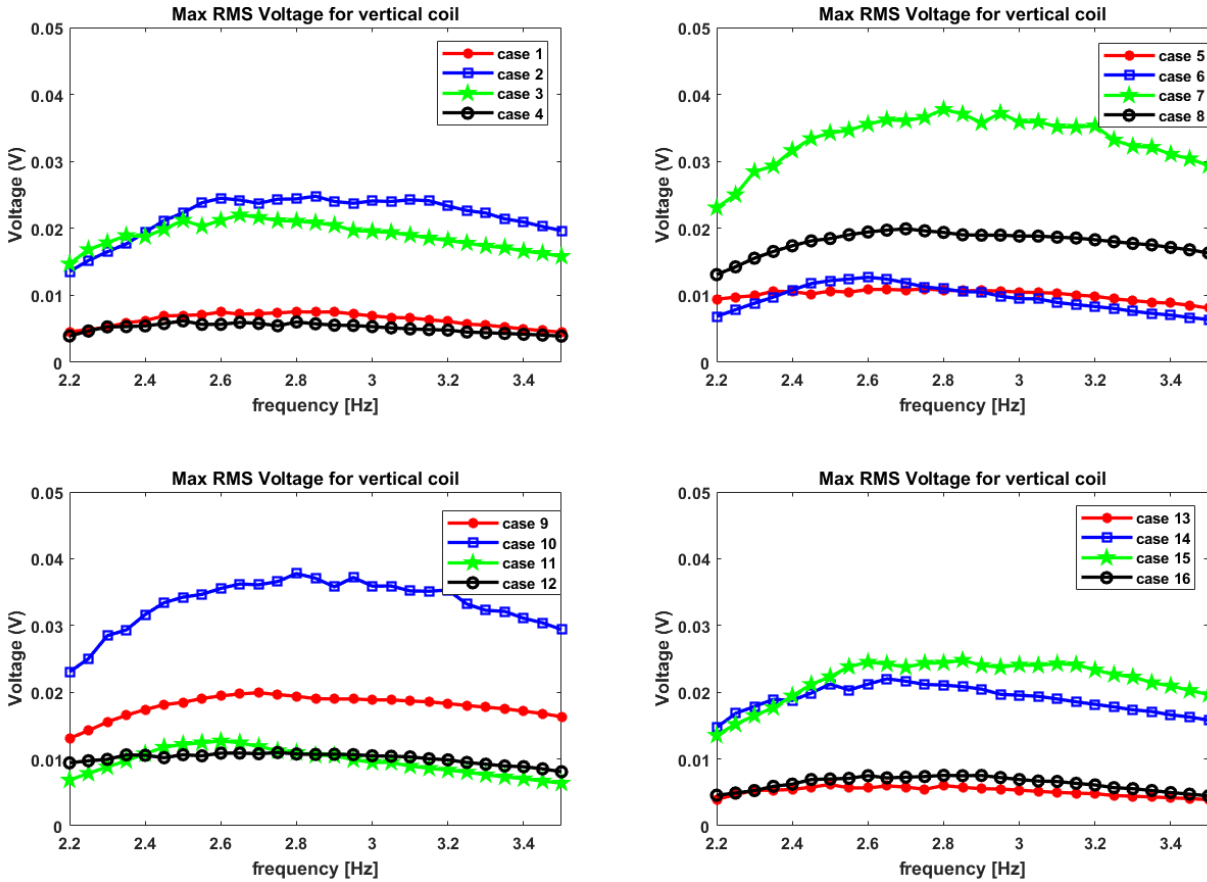


Figure 44 RMS voltage plots for Cases 1-16 while considering vertically wound coil for L=5 cm tank

Secondly, it is observed that there is a secondary peak that was observed for L=10 cm tank near 1.5 Hz in for both the horizontal and vertical windings, does not seem to appear for L=5cm tank. This might be due to the inexistence of any non-linear coupling between the sloshing modes of the system, perhaps due to the reduction in size and the increase in the modal frequency from 2 Hz (for L = 10 cm tank) to 3 Hz (for L = 5 cm tank).

In order to determine the power through the load resistor the RMS current is calculated by solving for instantaneous current from equation (22) for all the 9 coils and 25 load resistors. Then

the RMS value of this current is taken and power through the load resistance is calculated using $I_{rms}^2 \times R_L$ using the value of rms current pertaining to that particular load resistor and that particular coil. Then the maxima of the power output for the above 225 cases (i.e. 9 coils and 25 load resistors) is taken for each of the 16 cases of magnet arrangements and all the 27 frequencies. In **Figure 45** the maximum power through the horizontal winding for all the 16 cases and all the 27 frequencies is plotted.

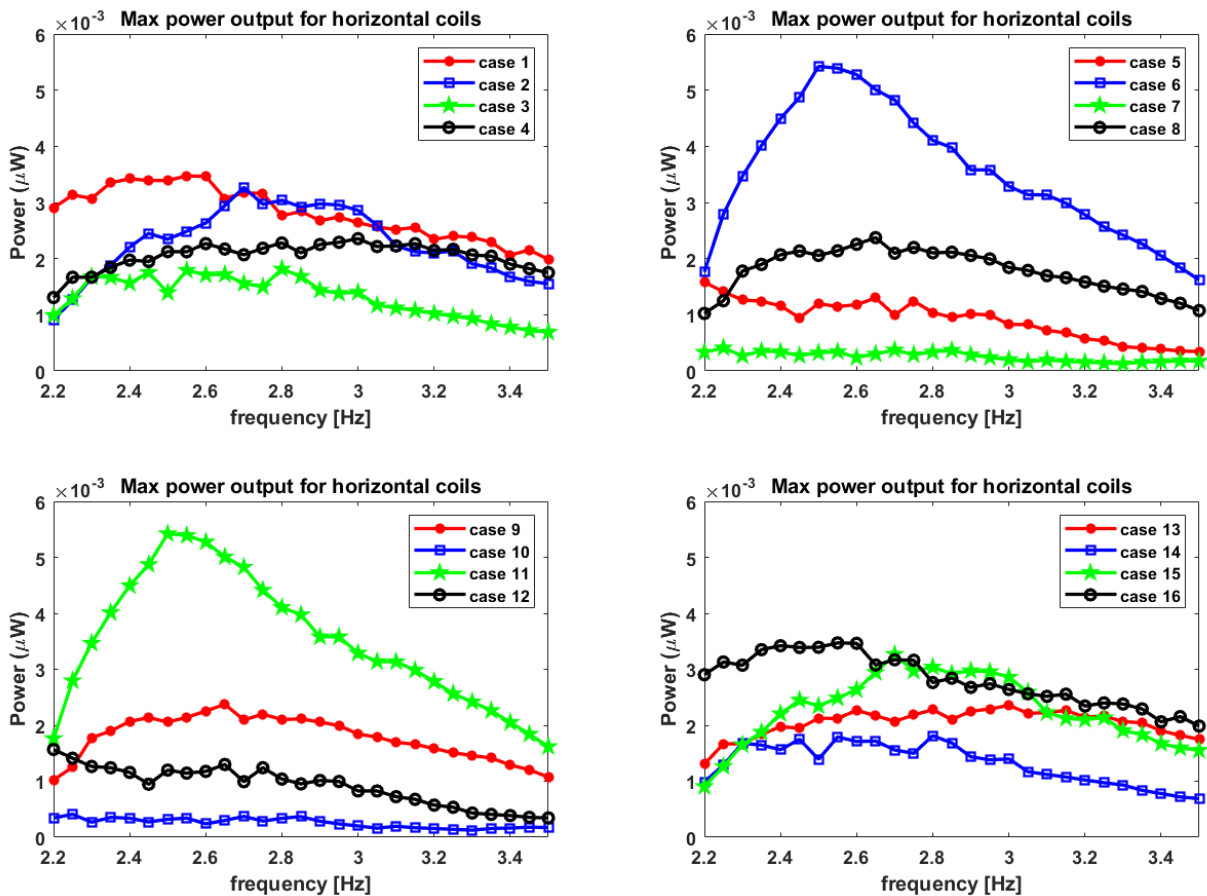


Figure 45 Maximum power output from Horizontal winding for L = 5cm tank

The maximum power obtained is 0.005 micro-watts (μW) or $0.5 \left(\frac{nW}{g} \right)$ for case 6 and case 11. Here too the symmetry observed for the max voltages is evident. The maximum power value is obtained for a frequency of 2.5 Hz, which points towards the shifting of peak from the first

modal frequency of 2.96 Hz. This again can be attributed to the magnetic body force exerted on the fluid in the y direction. Here the frequency for peak power shifts to the left of the modal frequency for the horizontal winding, unlike the case of L=10 cm tank where the frequency shifted towards the right.

For the vertical coil, the max RMS power for all the 27 frequencies and 16 magnet cases is plotted in **Figure 46**. The maximum power is obtained at 2.8 Hz for case 7 (and case 10) and is almost near to 0.7 micro-watts (μW) or $70 \left(\frac{nW}{g}\right)$, which is two orders of magnitude higher than that from the horizontal coils. It must be noted that the frequency where the max power output is observed is nearer to the modal frequency of 2.95 Hz, as compared to the horizontal coils. The shift in the peak occurs towards the left from the modal frequency and is very small as compared to that in the horizontal winding case. This can be attributed to the fact that the output voltage for the vertical coil is a function of the magnetic field in the x direction. The range of the max power extracted using different magnet configurations is very high for the vertical winding, as was observed for L = 10 cm case. With that change almost two orders of magnitude of difference is observed in the max power harvested from the vertical winding of the device. This can also be attributed to the fact that the excitation provided to the system is in the x direction. This coupled with the gravity in the y direction, makes the harvesting of energy from changes in magnetic field in the y direction unattractive. This also makes the power harvested from horizontal windings from all the 16 cases of magnet arrangements, to have a narrow variance. This can be useful while designing systems which have both x and y excitations or perhaps angular excitation or a combination of all the three.

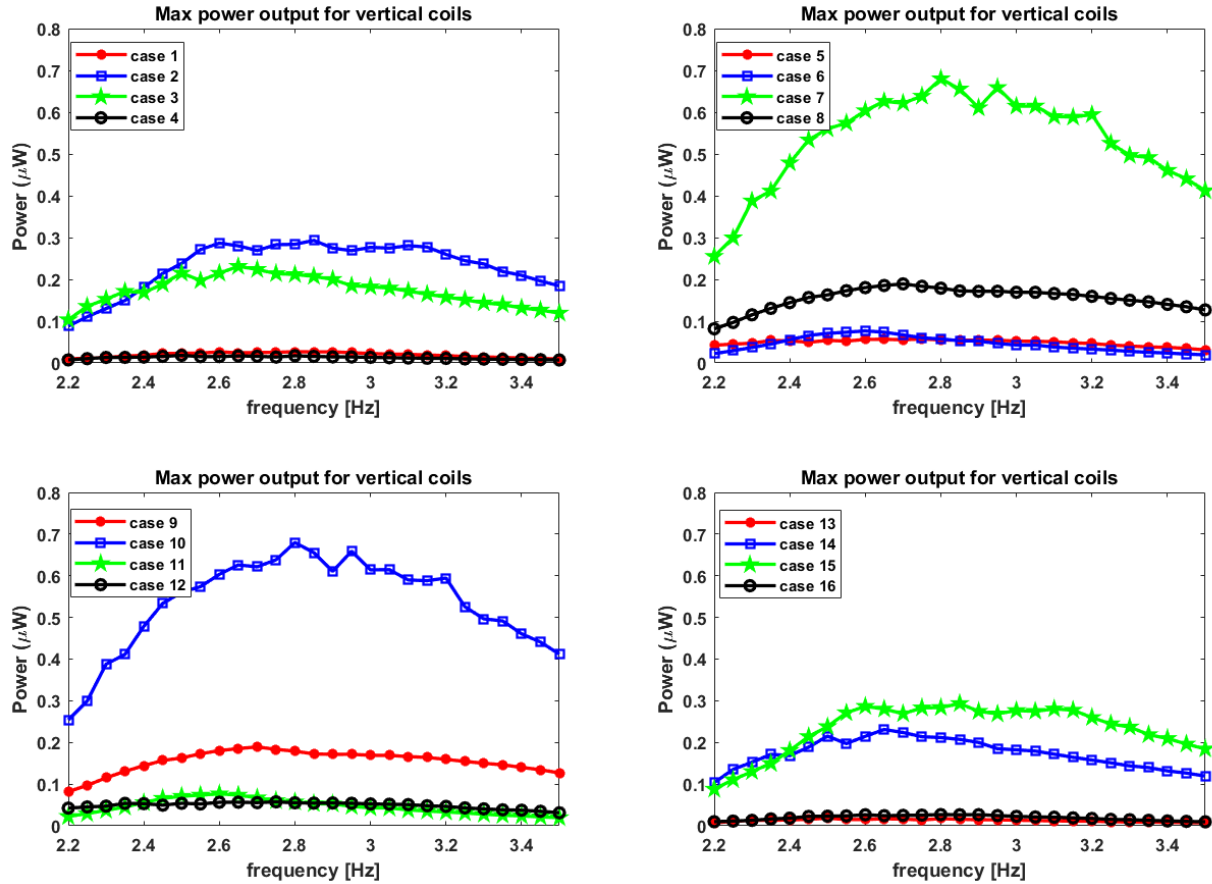


Figure 46 Maximum power output from Vertical winding for L = 5cm tank

6. Conclusion

A completely new design for a ferrofluid sloshing vibration energy harvester is introduced in this work. The design is inherently symmetric, because the purpose of the design is to exploit symmetry which can be easy to manufacture. Two tanks one of length 10 cm and one of length 5 cm are observed by providing a constant external acceleration of 1 m/s^2 . The tanks are then subjected to a frequency sweep for 16 different combinations of the 4 magnets, simply by changing their polarity.

The most important results are observed:

- a) The maximum RMS voltages harvested reached almost 0.15 V

- b) The maximum power after impedance matching was obtained from 10 cm tank, which is around a value of $20 \mu\text{W}$ or $2 \left(\frac{\mu\text{W}}{g}\right)$.
- c) For a 5cm tank, the highest power output was $0.7 \mu\text{W}$ which is higher than what was obtained from the horizontal winding for $L = 10$ cm tank.

These observations will have a huge impact on the future design of Ferrofluid sloshing VEH's. Usually sloshing motion decreases with the decrease in the significant length scale. At low scales, the flow converts into capillary flow. Hence, miniaturizing these sloshing energy harvesting systems after a particular extent would involve huge trade-offs. However, from the third observation, it can be concluded that miniaturization can still lead to good performance if done within the limits and the magnets are oriented properly, to yield highest result. Finally, these observations pave way for future research into miniaturizing the systems. Perhaps a regime like the 'high frequency low amplitude' etc. might be suitable for harvesting energy from miniaturized Ferrofluid VEH's. Finally, it is also to be noted that for maintaining the viability of the 2-D simulation as an exact representation of a 3-D tank the depth of the tank was assumed to be equal to the longest edge of the tank. This increased the length of the wire used in winding around the tank as a coil, and hence reduced the harvested power. The power harvested can be increased significantly when the coil is optimized, or when a different 'pick-up' mechanism is used which is more efficient than an inductive circuit. Hence, an optimization into the electrical conditioning efficiency of such systems would be necessary for future studies, in order to arrive at the most optimal designs for the harvesters.

Chapter 3: Feasibility Study of a Hybrid Solid – Liquid Vibration Energy Harvester

1. Introduction

Vibration energy harvesting (VEH) systems convert ambient vibrations into electric power. The primary purpose of the VEH systems is to provide seamless power and eventually replace the need for batteries in electronic devices. Most VEH systems consist of an external excitation coupled to a transduction mechanism, which then supplies power to an external circuit. In most cases the transduction mechanism includes a solid-state transducer, which transforms the deformations into electric charge, for example piezoelectric devices, electro active polymers, etc. [147]–[149]. These solid-state VEH systems however have a major disadvantage; the energy harvesting potential is very narrow-band (i.e. the highest output from these devices is achieved at or around resonant frequency modes). The incongruity between ambient vibrations, which usually are very wide-band, and the resonant modes, further exacerbates the deficiencies in energy harvesting realized versus the potential. Recently, a novel VEH system was introduced with a ferrofluid as a liquid-state transduction mechanism[23], which was discussed in earlier sections. This system has a significant advantage over solid-state VEH systems, as the resonant modes for ‘sloshing’ are very tightly distributed, thus, it is more suited for harvesting energy from wide-band ambient vibrations[128], [150]. However, the power output from such a system depends heavily upon magnetic parameters[24] and thus can have limitations on their power output. In this chapter a combined sloshing and piezoelectric transduction vibration energy harvester is postulated. This system is then studied numerically to assess its feasibility. The principle behind such postulation

is to utilize the kinetic energy of the ferrofluid not only just as a liquid state transduction mechanism, but also as a liquid-solid coupled system with a piezoelectric as an additional transduction mechanism. In the next section the setup of the hybrid energy harvester is discussed and the third section presents details about governing equations and physical properties of the materials. In the fourth section the numerical modeling details are presented and fifth section discusses the results of the numerical analysis of the system.

2. Problem setup

Figure 47 shows the schematic representation of the hybrid energy harvester design used in this study. The design consists of a tank of length L and height H partially filled with a ferrofluid to a height h . On the top wall of the tank a piezoelectric bimorph is affixed. The bimorph has piezoelectric beams of thickness t_p and height h_p attached to the base end of a steel beam of thickness t_b and height h_b . The midplane of the bimorph coincides with the midplane of the tank. The piezoelectric bimorph has two piezoelectric patches of smaller length than the central beam attached at the base. The central beam is of structural steel and is used as a terminal for voltage produced in the piezo material.

Similarly, for the ferrofluid the electromotive force generated is assumed to be picked-up by an external pick-up coil with 2000 turns. For simplification it is assumed that the applied magnetic field over the harvester area is unidirectional in x-direction [25]. This system is excited through a lateral external excitation which is periodic in nature.

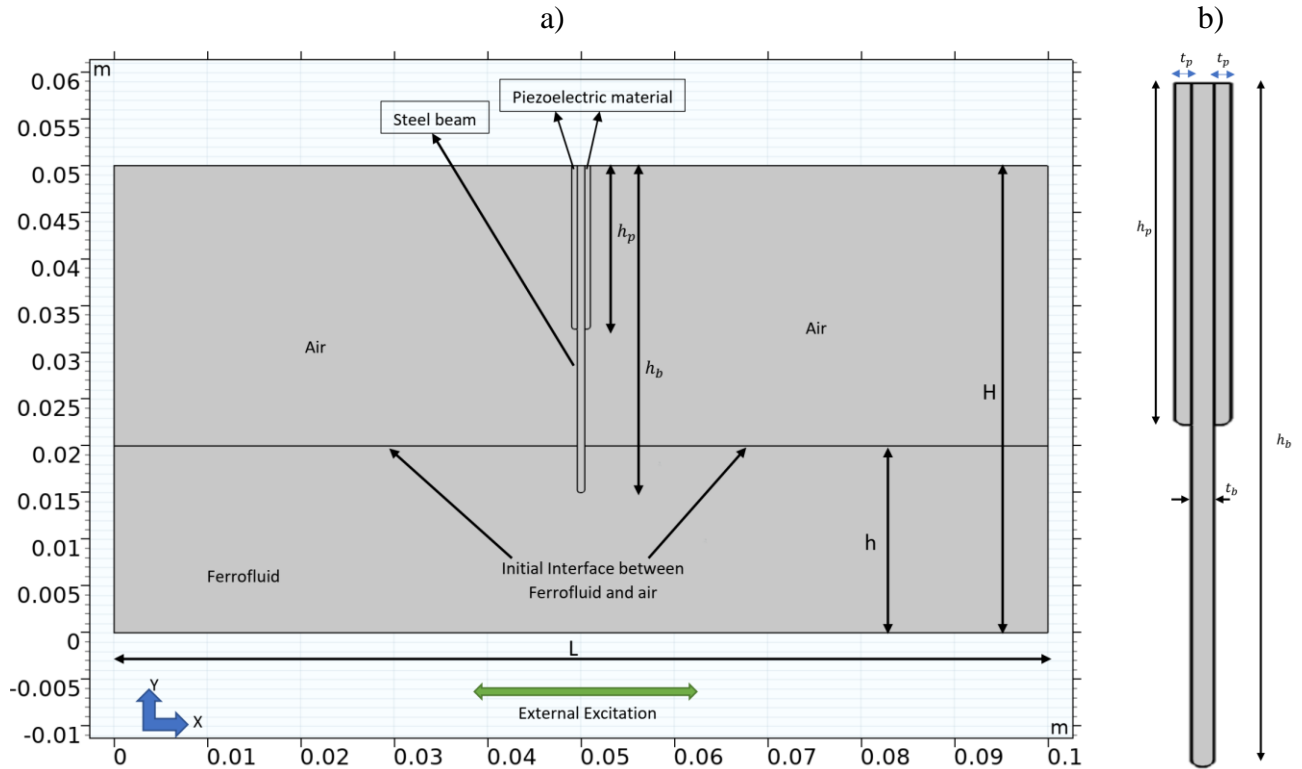


Figure 47 Configuration of the hybrid VEH system a) the tank and piezo bimorph and b) close-up of the piezo bimorph

The applied magnetic field applied to the harvester is shown in **Figure 48**.

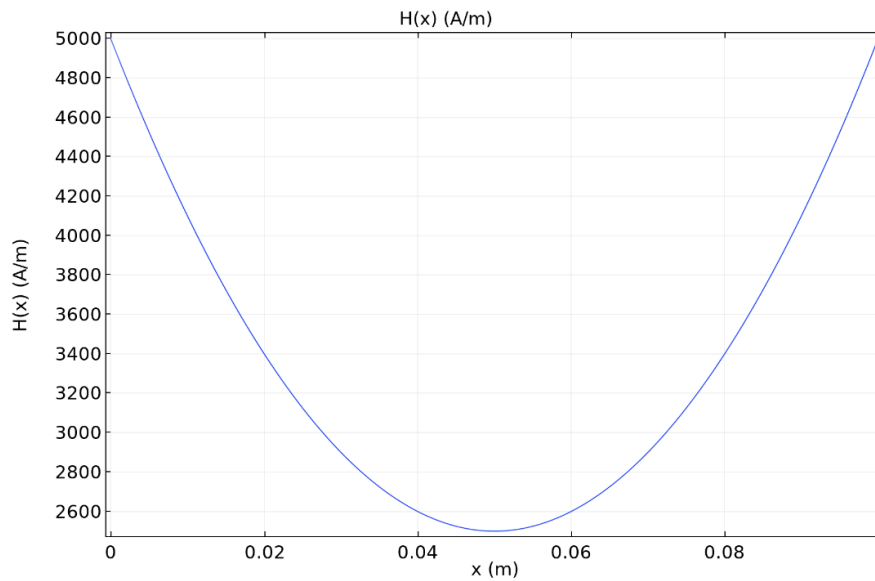


Figure 48 Magnetic Field function

3. Governing Equations

The proposed system in the previous section would be governed by different physical phenomena inter-twined with each other. This makes the above system a multiphysics system. The following phenomena are observed:

- 1) Fluid mechanics (Navier-Stokes)
- 2) Free surface flow (Surface tension – Level set)
- 3) Wall wetting (Contact angle [151])
- 4) Fluid structure interaction
- 5) Ferrohydrodynamics (Maxwell's equations)
- 6) Electrodynamics in piezoelectric (Maxwell's equations), and
- 7) Finally, to track the deformation of the bimorph a moving mesh interface is used.

Here, the fluid mechanics of the ferrofluid is influenced by the Kelvin body force exerted by the magnetic field (or magnets like in previous chapter) on the ferrofluid. Secondly, the fluid flow interacts with the piezoelectric bimorph and displaces the beam, which in-turn influences the flow (fully-coupled). Thirdly, the free surface changes form, hence the interface between the air and the fluid keeps moving and needs to be tracked in order to obtain the correct distribution of force fields inside the harvester. Fourthly, the stresses induced in the bimorph transforms into strains in the piezoelectric material, which gives rise to charge displacement and hence a voltage/current. Finally, the ferrofluid wets the wall and inner surfaces, and hence the surface tension force changes. Wetting involves complicated physics and needs to be properly accounted for in order to define correct surface profile between ferrofluid and air. The governing equations pertaining to the above physical phenomena and their couplings are defined in the equations below.

a) Fluid Mechanics

Continuity:

$$\rho \nabla \cdot \vec{V} = 0 \quad (1)$$

Momentum:

$$\rho \frac{\partial \vec{V}}{\partial t} + \rho (\vec{V} \cdot \nabla) \vec{V} = -\nabla p + \mu \nabla^2 \vec{V} + \vec{F}_m + \rho \vec{g} + \vec{F}_{st} + \vec{F}_{FSI} \quad (2)$$

where, \vec{V} is the velocity vector, \vec{F}_m is the magnetic force, \vec{g} is the external acceleration on the system including the external excitation, \vec{F}_{st} is the force of the surface tension, and \vec{F}_{FSI} is the force applied by the piezoelectric bimorph beam on the fluid elements.

Here the external excitation is given as:

$$x = X_0 \sin(\omega t) \quad (4)$$

where X_0 is the amplitude of external excitation and ω the angular frequency, which is related to the excitation frequency f as, $2\pi f$. In this study this f is varied from 0.8 to 1.2 Hz, to simulate low frequency high amplitude excitation.

b) Level-set equations for interface tracking:

$$\frac{\partial \phi}{\partial t} + \vec{V} \cdot \nabla \phi = \gamma \nabla \cdot \left(\epsilon_{ls} \nabla \phi - \phi (1 - \phi) \frac{\nabla \phi}{|\nabla \phi|} \right) \quad (5)$$

where, ϕ is the level set variable, γ is the re-initialization parameter and ϵ_{ls} is the parameter which controls the thickness of the fluid-air interface.

c) The equations for flow coupling of magnetic force and surface tension force are as follows

$$\vec{F}_{st} = \sigma_m \delta \kappa \mathbf{n}_i + \delta \nabla_s \sigma_m \quad (6)$$

where, σ_m is the surface tension coefficient, δ is a Dirac delta function located at the interface, κ is the curvature of the surface, and \mathbf{n}_i is the normal vector of the liquid-gas interface and ∇_s is the surface gradient operator.

The interface normal is given by:

$$\mathbf{n}_i = \frac{\nabla\phi}{|\nabla\phi|} \quad (7)$$

The Dirac delta function is given by:

$$\delta = 6 |\nabla\phi| |\phi(1 - \phi)| \quad (8)$$

The curvature of the surface is given by:

$$\kappa = -\nabla \cdot \mathbf{n}_i \quad (9)$$

The surface gradient operator is given by:

$$\nabla_s = (I - \mathbf{n}_i \mathbf{n}_i^T) \nabla \quad (10)$$

Also, the angle that the fluid makes with the wall while wetting is assumed to be 90° . This is a standard assumption, while solving sloshing flows[25].

For the fluid domain inside the tank the properties must be expressed in terms of the level set variable. Density is given as:

$$\rho = \rho_1 + (\rho_2 - \rho_1)\phi \quad (11)$$

Viscosity is given as:

$$\mu = \mu_1 + (\mu_2 - \mu_1)\phi \quad (12)$$

where indices 1 and 2 denotes fluid 1 and fluid 2, which in our case is the ferrofluid and air, respectively. Similarly, to calculate the Kelvin body force, the magnetic properties of the fluids must be expressed in terms of the level set variable.

$$\vec{F}_m = \vec{M} \cdot \nabla \vec{H} \quad (13)$$

where, the magnetization \vec{M} is given by the constitutive relation:

$$\vec{M} = \chi_m \vec{H} \quad (14)$$

where, χ_m is the magnetic susceptibility and is obtained from the level set function for the whole domain as:

$$\chi_m = \chi_{m1} + (\chi_{m2} - \chi_{m1})\phi \quad (15)$$

The electromotive force from sloshing is picked up by an external coil with 2000 turns (N).

The electromotive force is given as:

$$\epsilon = -N \frac{d\Phi}{dt} \quad (16)$$

where, Φ is the magnetic flux, obtained by integrating the magnetic flux density over the area.

d) Structural mechanics and piezoelectric:

$$\rho \frac{\partial^2 u_{solid}}{\partial t^2} = \nabla \cdot \sigma + \overline{F}_V \quad (17)$$

where u_{solid} is the displacement of the piezoelectric bimorph, σ is the Cauchy stress tensor, and \overline{F}_V is the external volumetric body forces acting upon the beam. The fluid structure interaction stresses are caused by the reaction forces caused by the fluid on the bimorph. The force experienced by the fluid is calculated in similar way and is then accounted for in mesh displacement to capture the effect of the fluid structure interaction.

The strain on the bimorph causes electric displacement in the piezoelectric material and generates power. We have considered the piezo material 'z-x' or '3-1' as the material axis for our calculations. The piezoelectric interaction is described by the following equations:

$$S = s_E \sigma + d' E \quad (18)$$

$$D = d \sigma + \epsilon^T E \quad (19)$$

where, S is the strain tensor, s_E the elastic compliance matrix, d is the piezoelectric strain coefficient matrix, D is the electric displacement, ϵ the dielectric permittivity matrix, E the electric field and σ the stress tensor.

A commercially available ferrofluid developed by FerroTec Corporation, named **EFH – 3** is used in the study. The two piezoelectric materials used for the bimorph are PZT-7A and PVDF. The properties of the three materials are listed in Appendix C.

4. Numerical Modeling

The governing equations are solved in COMSOL Multiphysics using its inbuilt modules and coupling interfaces for fluid-structure interaction, separated two phase flow with level set, piezoelectric effect, and internal wetted wall. **Figure 49** illustrates the meshing scheme used in COMSOL. The beam is meshed with very fine elements in order to track the movement of the mesh and Laplace mesh smoothing is used to move the mesh according to the velocity profile of the solid[152].

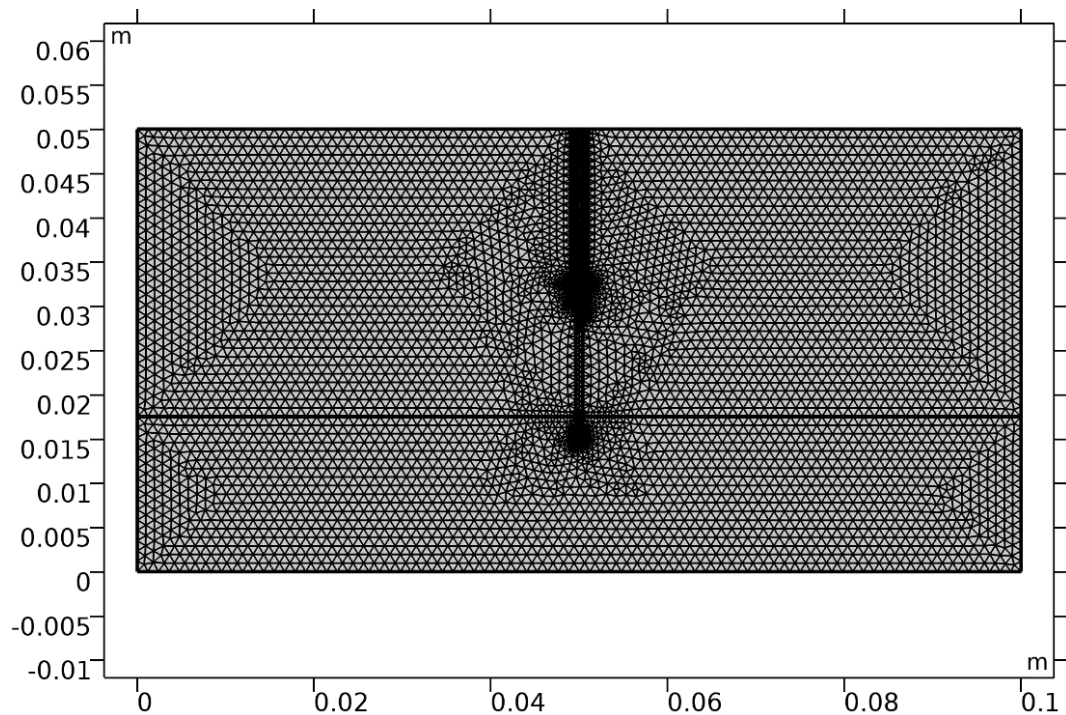


Figure 49 Meshing of the domain of Energy harvester

In order to analyze the performance of the hybrid energy harvester, a combination of 5 different parameters are varied, as shown in **Table 10**. For all these geometrical parameters, the

harvester is subjected to a frequency sweep at low frequencies, i.e. from 0.8 Hz to 1.2 Hz. The open circuit voltages are calculated using piezoelectric and sloshing equations.

Table 10 Simulation cases for energy harvester

Case	PVDF	PZT-7A
1	$X_0 = L, H = \frac{L}{2}, \frac{h}{H} = 0.35, \frac{h_b}{L} = 0.7, h_p = \frac{h_b}{4}$	$X_0 = L, H = \frac{L}{2}, \frac{h}{H} = 0.35, \frac{h_b}{L} = 0.7, h_p = \frac{h_b}{4}$
2	$X_0 = L, H = \frac{L}{2}, \frac{h}{H} = 0.35, \frac{h_b}{L} = 0.7, h_p = \frac{h_b}{2}$	$X_0 = L, H = \frac{L}{2}, \frac{h}{H} = 0.35, \frac{h_b}{L} = 0.7, h_p = \frac{h_b}{2}$
3	$X_0 = L, H = \frac{L}{2}, \frac{h}{H} = 0.4, \frac{h_b}{L} = 0.7, h_p = \frac{h_b}{4}$	$X_0 = L, H = \frac{L}{2}, \frac{h}{H} = 0.4, \frac{h_b}{L} = 0.7, h_p = \frac{h_b}{4}$
4	$X_0 = L, H = \frac{L}{2}, \frac{h}{H} = 0.4, \frac{h_b}{L} = 0.7, h_p = \frac{h_b}{2}$	$X_0 = L, H = \frac{L}{2}, \frac{h}{H} = 0.4, \frac{h_b}{L} = 0.7, h_p = \frac{h_b}{2}$

The different physics interfaces are handled in COMSOL, using a single segregated iteration, with different steps solving for the dependent variables which are present in the step. The steps have the following dependent variables and are executed in this sequential order for each time step:

- a) Velocity and pressure
- b) Level-set variable
- c) Displacement field for the solid
- d) Moving mesh
- e) Piezoelectric voltage and charge

These equations are solved using the in-built Streamline Upwind Petrov Galerkin (SUPG) method, which takes care of the stability of the solution[153]. Since this is an unsteady problem, the algorithm needs to solve for time marching of these variables and not just a steady-state solution. Hence, in order for the solution to progress all of the above steps need to be solved at each time step, and once the residual goes below the set tolerance, the solution converges at that

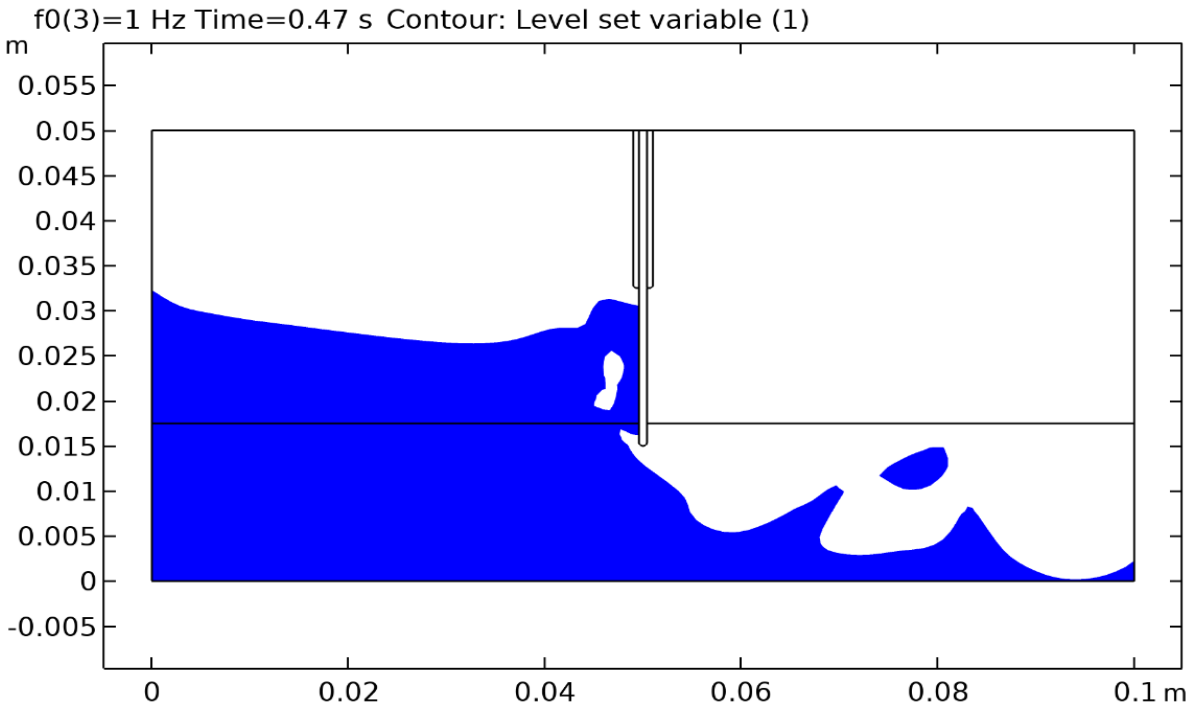
particular time. Furthermore, the time-stepping used is implicit adaptive time stepping, which adapts the time-step according to the non-linearity faced in each time step. The time marching method used here, is the backward differencing formula (BDF) of order 2 or 1. Since, the solver is implicit and adaptive, in order to obtain time step convergence, the maximum time step parameter is changed. A parameter of 0.005 sec was used as it was stable and much less expensive than a smaller time step.

Moreover, the PARDISO and MUMPS direct solvers are used to solve each segregated step, to obtain convergence at each time step. Finally, grid convergence studies were also performed, by altering the meshing parameter. In this case the maximum mesh dimension was altered, and a significantly fine mesh was generated in order to capture the physics correctly.

5. Results & Discussion

Figure 50 represents a flow solution for the two piezos with an excitation frequency of 1 Hz at time equals 0.47 seconds. These results are for case 2, where the piezoelectric material covers half the substrate. The RMS voltages from the two configurations for all four cases are shown in **Figure 51**. The piezoelectric energy harvesting circuit and the ferrofluid sloshing energy harvesting circuit are considered to be separate from each other. This approach was used to understand the true potential of the proposed system and obtain design guidelines to transform into practical designs. The observed voltages from the piezos are different from each other. The voltage from PZT 7A is approximately half of that from PVDF. This can be attributed to the order of magnitude lower stiffness of PVDF. Also, the simulations are run for 4 time periods, and the RMS voltage is calculated from the last three time periods (or cycles) data for the voltage.

A)



B)

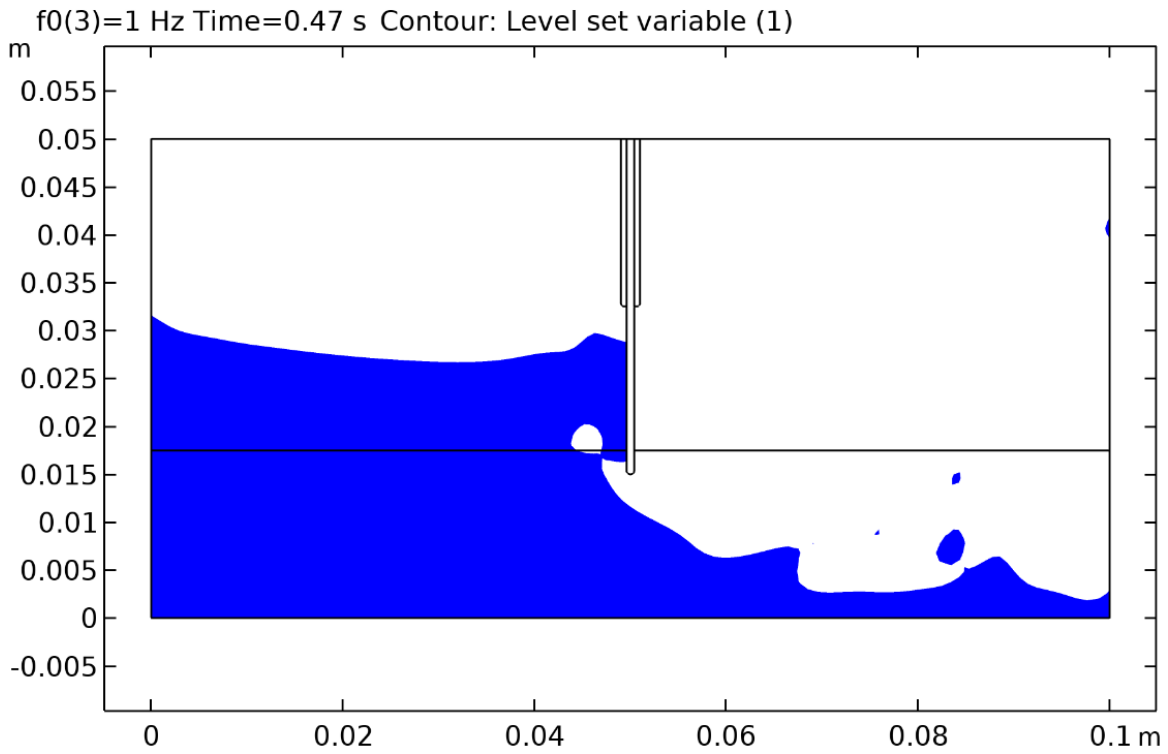


Figure 50 Flow Evolution for a) PZT7A and b) PVDF for $f = 1$ Hz at $t = 0.47$ sec

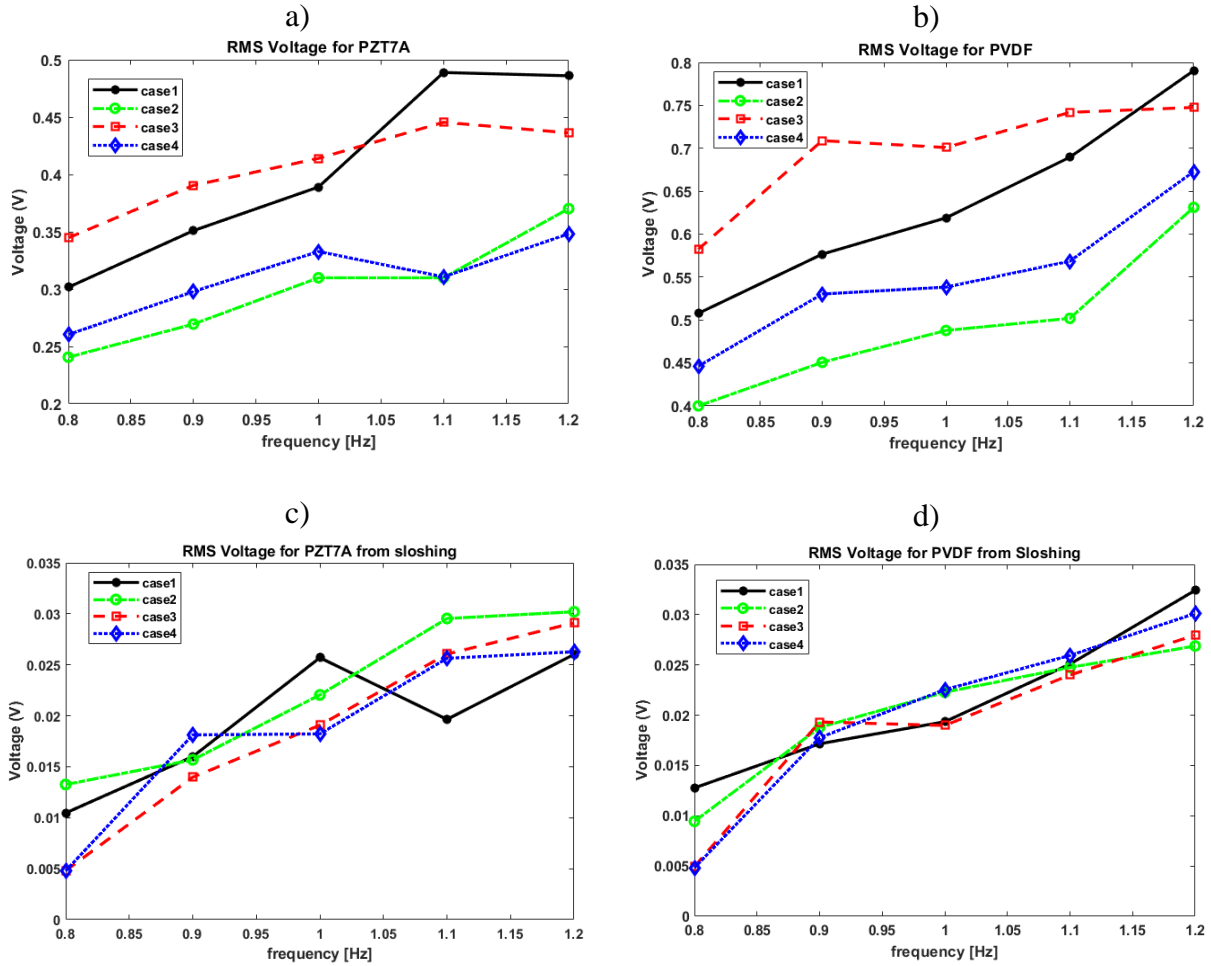
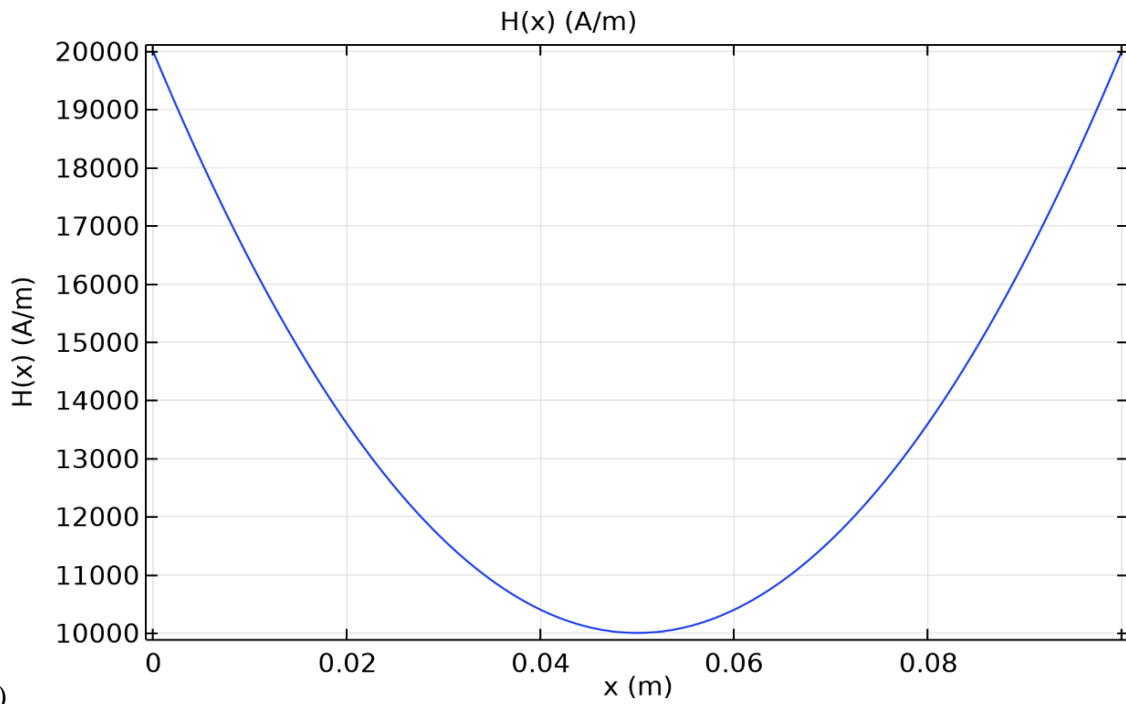


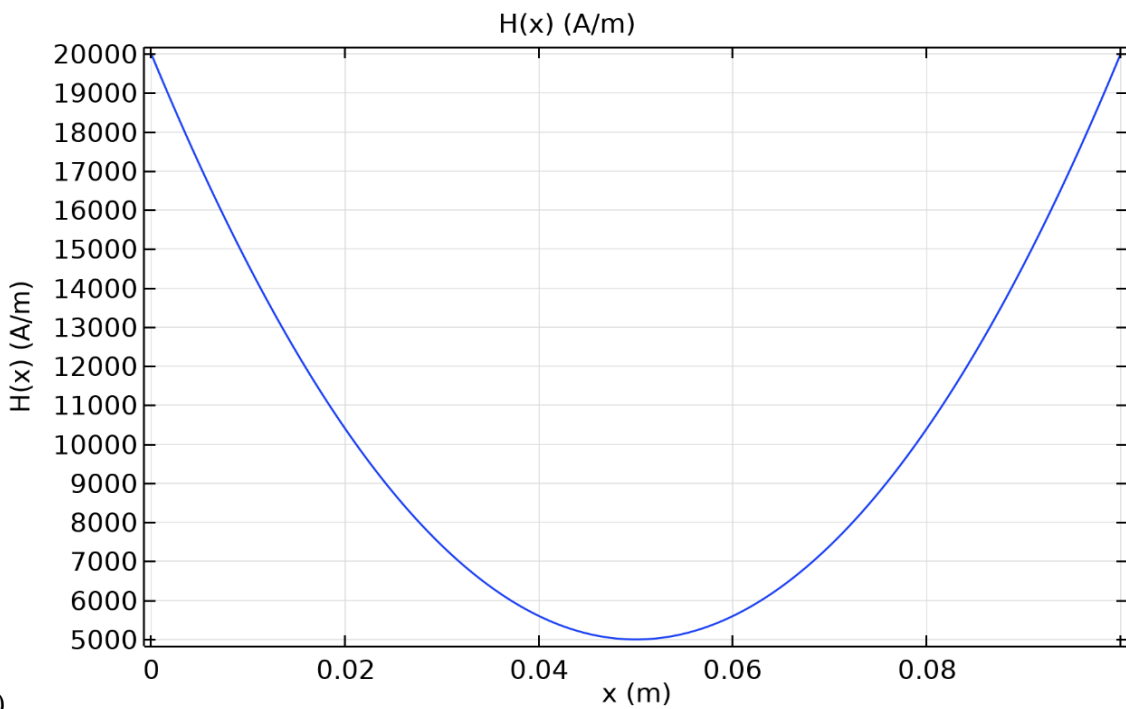
Figure 51 RMS total voltage for a) PZT-7A and b) PVDF and Voltage from sloshing from c) PZT-7A and d) PVDF

The voltage evolution plots for all the cases and for both the piezoelectric materials is shown in Appendix B. It must be observed that just like the external excitation function, the voltage also evolves as a periodic function.

Since, the voltages from sloshing are very low, and PVDF produced the highest voltage, two more magnetic field functions are introduced. Case 1 using the PVDF is repeated with these two new magnetic field functions for five values of maximum magnetic field, varying from 10 kA/m to 24 kA/m. The two magnetic field functions are shown in **Figure 52**.



A)



B)

Figure 52 Graph for a) Magnetic field function 1 and b) Magnetic field function 2, for $H_{\text{max}} = 20$ [kA/m]

The RMS voltages from both the magnetic field functions for case 1 are shown in **Figure 53**. The RMS voltage for PVDF is highest for the 10 kA/m case for both magnetic field functions. This can be attributed to an increase in the magnitude of the Kelvin body force, which by virtue of the two function shapes, will try to attract the ferrofluid towards the walls. Additionally, the voltage generated from sloshing increases with increasing maximum magnetic field.

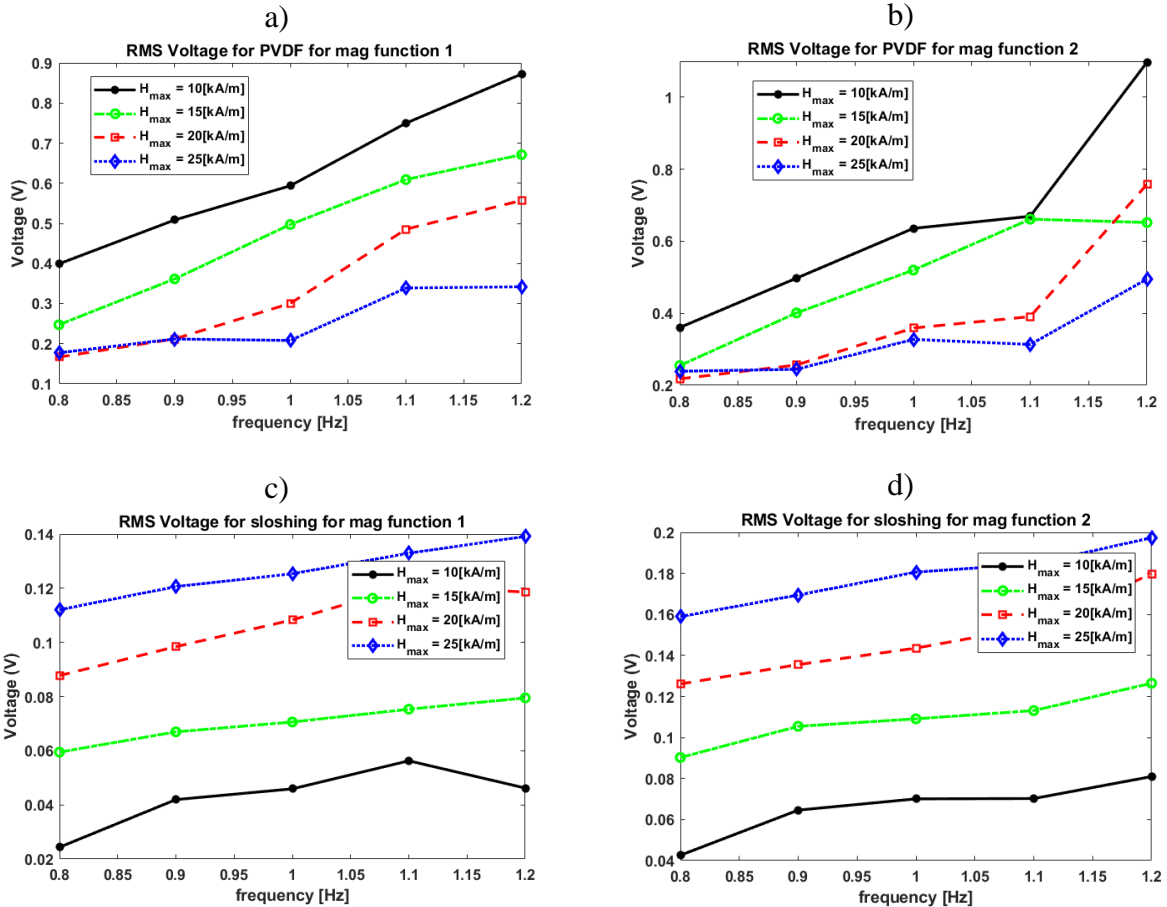


Figure 53 Total RMS voltage for PVDF for a) Magnetic function 1 b) magnetic function 2 and sloshing voltage for PVDF for a) magnetic function 1 and b) magnetic function 2

Finally, in order to define the feasibility of the system, the output power must be optimized. In this chapter the output power from the piezo is prioritized in the sense that the parameters controlling the output power from piezo are embedded in the structure of the bimorph. Since, the simulation of the piezo was assumed to have very low coupling, the optimal impedance or

resistance can be obtained by considering a simple AC circuit, where the optimal resistance value is given as[154]–[156]:

$$R_{opt} = \frac{1}{C_0\omega}$$

where, C_0 is the parasitic capacitance of the piezoelectric and is given by:

$$C_0 = \frac{\epsilon_{33}^s A}{L}$$

where A is the area of the piezo and L the length of the piezo. Area is given as:

$$A = t_p W$$

where, W is the width of the piezoelectric material. Calculating this from the material properties of PVDF and PZT-7A, the power comes out to be in nanowatts. This is because, the natural frequency of vibration of the bimorph is very high as compared to the excitation frequency used here.

6. Conclusion

A feasibility study is presented with regards to the design of a hybrid piezoelectric-ferrofluid VEH. In order to simplify the analysis a number of factors were relaxed. Notably, the magnetic field was imposed as a simple function rather than a defined magnetic field through the placement of external magnets. Also, the bimorph was assumed to be thick enough to not disrupt the flow field, and hence fluid loading on the structure becomes more significant. These factors helped establish the feasibility of a hybrid system such as this. However, an optimized system could not be established (i.e. the power output from the bimorph is very low). However, it can still be utilized for some applications which require low power. It must be noted that the present system has the capability to be established as a new alternative for renewable and seamless power. However, to achieve that extensive optimization studies need to be performed and the optimized system capabilities need to be established.

REFERENCES

- [1] J. H. Spurk and N. Aksel, *Fluid Mechanics*, Second. Springer, 2008.
- [2] H. Yamaguchi, *Engineering Fluid Mechanics*. 2008.
- [3] H. Song, *Engineering Fluid Mechanics*. Springer, 2018.
- [4] S. Lee, C. Park, D. Kulkarni, S. Tamanna, and T. Knox, “Heat and mass transfer in a permeable fabric system under hot air jet impingement,” *2010 14th Int. Heat Transf. Conf. IHTC 14*, vol. 5, pp. 619–628, 2010.
- [5] A. Bar-Cohen, M. Arik, and M. Ohadi, “Direct liquid cooling of high flux micro and nano electronic components,” *Proc. IEEE*, vol. 94, no. 8, pp. 1549–1570, 2006.
- [6] D. C. Rennels and H. M. Hudson, *Pipe Flow: A Practical and Comprehensive Guide*. 2012.
- [7] H. Rim, D. Jin, J. Ryou, and Y. Seok, “Ferrohydrodynamic energy harvesting based on air droplet movement,” *Nano Energy*, vol. 11, pp. 171–178, 2015.
- [8] V. M. Job and S. R. Gunakala, “Mixed convective ferrofluid flow through a corrugated channel with wall-mounted porous blocks under an alternating magnetic field,” *Int. J. Mech. Sci.*, vol. 144, no. September 2017, pp. 357–381, 2018.
- [9] R. J. Hosking and R. L. Dewar, *Fundamental fluid mechanics and magnetohydrodynamics*. 2016.
- [10] H. Rahman and S. A. Suslov, “Thermomagnetic convection in a layer of ferrofluid placed in a uniform oblique external magnetic field,” *J. Fluid Mech.*, vol. 764, pp. 316–348, 2015.
- [11] R. E. Rosensweig, *Ferrohydrodynamics*. Dover Publications (February 20, 2014), 1970.
- [12] S. Odenbach, “Ferrofluids - Magnetically controlled suspensions,” in *Colloids and*

- Surfaces A: Physicochemical and Engineering Aspects*, 2003, vol. 217, no. 1–3, pp. 171–178.
- [13] S. Odenbach, *Colloidal magnetic fluids : basics, development and application of ferrofluids*, no. 763. 2009.
- [14] J. Popplewell, “Technological Applications of Ferrofluids,” *Phys. Technol.*, vol. 15, 1984.
- [15] M. Hejazian and N. T. Nguyen, “A rapid magnetofluidic micromixer using diluted ferrofluid,” *Micromachines*, vol. 8, no. 2, 2017.
- [16] N. T. Nguyen, “Micro-magnetofluidics: Interactions between magnetism and fluid flow on the microscale,” *Microfluidics and Nanofluidics*, vol. 12, no. 1–4. pp. 1–16, 2012.
- [17] E. Kurtoğlu *et al.*, “Ferrofluid actuation with varying magnetic fields for micropumping applications,” *Microfluid. Nanofluidics*, vol. 13, no. 4, pp. 683–694, 2012.
- [18] C. Rinaldi, A. Chaves, S. Elborai, X. He, and M. Zahn, “Magnetic fluid rheology and flows,” *Current Opinion in Colloid and Interface Science*, vol. 10, no. 3–4. pp. 141–157, 2005.
- [19] H. Coles and S. Greenberg, “Direct Liquid Cooling for Electronic Equipment,” 2014.
- [20] S. Banerjee, A. Mukhopadhyay, S. Sen, and R. Ganguly, “Optimizing thermomagnetic convection for electronics cooling,” *Numer. Heat Transf. Part A Appl.*, vol. 53, no. 11, pp. 1231–1255, 2008.
- [21] F. Larachi and D. Desvigne, “Ferrofluid induced-field effects in inhomogeneous porous media under linear-gradient dc magnetic fields,” *Chem. Eng. Process. Process Intensif.*, vol. 46, no. 8, pp. 729–735, 2007.
- [22] M. Mokhtari, S. Hariri, M. Barzegar Gerdroodbary, and R. Yeganeh, “Effect of non-uniform magnetic field on heat transfer of swirling ferrofluid flow inside tube with twisted

- tapes,” *Chem. Eng. Process. Process Intensif.*, vol. 117, no. January, pp. 70–79, 2017.
- [23] A. Bibo, R. Masana, A. King, G. Li, and M. F. Daqaq, “Electromagnetic ferrofluid-based energy harvester,” *Phys. Lett. Sect. A Gen. At. Solid State Phys.*, vol. 376, no. 32, pp. 2163–2166, 2012.
- [24] Q. Liu, S. F. Alazemi, M. F. Daqaq, and G. Li, “A ferrofluid based energy harvester: Computational modeling, analysis, and experimental validation,” *J. Magn. Magn. Mater.*, vol. 449, pp. 105–118, 2018.
- [25] S. Alazmi, Y. Xu, and M. F. Daqaq, “Harvesting energy from the sloshing motion of ferrofluids in an externally excited container: Analytical modeling and experimental validation,” *Phys. Fluids*, vol. 28, no. 7, 2016.
- [26] L. Mao and H. Koser, “Towards ferrofluidics for μ -TAS and lab on-a-chip applications,” *Nanotechnology*, vol. 17, no. 4, 2006.
- [27] G. Zhu and N. Nguyen, “Rapid magnetofluidic mixing in a uniform magnetic field,” *Lab Chip*, vol. 12, pp. 4772–4780, 2012.
- [28] M. Hejazian and N. Nguyen, “A Rapid Magnetofluidic Micromixer Using Diluted Ferrofluid,” *Micromachines*, vol. 8, no. 37, 2017.
- [29] M. Liu, X. Han, Q. Cao, and L. Li, “Performance analysis of a microfluidic mixer based on high gradient magnetic separation principles,” *J. Phys. D. Appl. Phys.*, vol. 50, no. 36, 2017.
- [30] C. Walker, M. Simiano, R. Zboray, and H. M. Prasser, “Investigations on mixing phenomena in single-phase flow in a T-junction geometry,” *Nucl. Eng. Des.*, vol. 239, no. 1, pp. 116–126, 2009.
- [31] Y. Iwamoto, H. Yamaguchi, and X. Niu, “Journal of Magnetism and Magnetic Materials

- Magnetically-driven heat transport device using a binary temperature-sensitive magnetic fluid,” *J. Magn. Magn. Mater.*, vol. 323, no. 10, pp. 1378–1383, 2011.
- [32] M. Hangi, M. Bahiraei, and A. Rahbari, “Forced convection of a temperature-sensitive ferrofluid in presence of magnetic field of electrical current-carrying wire : A two-phase approach,” *Adv. Powder Technol.*, vol. 29, no. 9, pp. 2168–2175, 2018.
- [33] L. Mao and H. Koser, “Ferrohydrodynamic pumping in spatially traveling sinusoidally time-varying magnetic fields,” in *Journal of Magnetism and Magnetic Materials*, 2005, vol. 289, pp. 199–202.
- [34] R. Ganguly, S. Sen, and I. K. Puri, “Heat transfer augmentation using a magnetic fluid under the influence of a line dipole,” *J. Magn. Magn. Mater.*, vol. 271, no. 1, pp. 63–73, 2004.
- [35] P. L. Spedding, E. Benard, and G. M. McNally, “Fluid Flow through 90 Degree Bends,” *Asia-Pacific J. Chem. Eng.*, vol. 12, pp. 107–128, 2004.
- [36] P. Hajiani and F. Larachi, “Chemical Engineering and Processing : Process Intensification Magnetic-field assisted mixing of liquids using magnetic nanoparticles,” *Chem. Eng. Process. Process Intensif.*, vol. 84, pp. 31–37, 2014.
- [37] G. K. Moghaddam, “Applications of Thermomagnetic Convection in Thermal Management of Electronic Systems,” NCSU, 2014.
- [38] I. Nkurikiyimfura, Y. Wang, and Z. Pan, “Heat transfer enhancement by magnetic nanofluids — A review,” *Renew. Sustain. Energy Rev.*, vol. 21, pp. 548–561, 2013.
- [39] A. Bouhrour and D. Kalache, “Thermomagnetic convection of a magnetic nanofluid influenced by a magnetic field,” *Therm. Sci.*, vol. 21, no. 3, pp. 1261–1274, 2017.
- [40] M. Yang, R. O. Handley, and Z. Fang, “Modeling of Ferrofluid Passive Cooling System,”

- in *COMSOL Conference 2010 Boston*, 2010, no. 1.
- [41] S. Odenbach, “Ferrofluids - magnetically controlled suspensions,” *Colloids Surfaces A Physicochem. Eng. Asp.*, vol. 217, pp. 171–178, 2003.
- [42] M. Sheikholeslami, M. B. Gerdroodbary, S. V. Mousavi, D. D. Ganji, and R. Moradi, “Journal of Magnetism and Magnetic Materials Heat transfer enhancement of ferrofluid inside an 90 ° elbow channel by non-uniform magnetic field,” *J. Magn. Magn. Mater.*, vol. 460, pp. 302–311, 2018.
- [43] M. I. Shliomis, “Ferrohydrodynamics : Retrospective and Issues,” *Ferrofluids*, no. 3, pp. 85–111, 2002.
- [44] L. M. Pop, S. Odenbach, A. Wiedenmann, N. Matoussevitch, and H. Bönemann, “Microstructure and rheology of ferrofluids,” *J. Magn. Magn. Mater.*, vol. 289, pp. 303–306, 2005.
- [45] FerroTec, “EFH Series Educational Ferrofluid Type: EFH3,” *Ferrotec (USA) Corporation*, 2019. .
- [46] N. Anand and R. Gould, “Study of Enhanced Self Mixing in Ferrofluid Flow in an Elbow Channel Under the Influence of Non-Uniform Magnetic Field.” 28-Jul-2019.
- [47] COMSOL, “Platform Product: COMSOL MULTIPHYSICS®,” *COMSOL INC.*, 2019. .
- [48] Roger W. Pryor, *Multiphysics Modeling using COMSOL*. 2011.
- [49] Y. He, Q. Bi, and T. Chen, “Heat transfer of ferrofluids: A review,” in *Development of Research in Microscale and Nanoscale Thermal and Fluid Sciences*, vol. 5, 2016, pp. 129–152.
- [50] S. Afkhami and Y. Renardy, “Ferrofluids and magnetically guided superparamagnetic particles in flows: a review of simulations and modeling,” *J. Eng. Math.*, vol. 107, no. 1,

- pp. 231–251, 2017.
- [51] G. Karimi-Moghaddam, “Applications of thermomagnetic convection in thermal management of electronic systems,” 2014.
- [52] V. Chaudhary, Z. Wang, A. Ray, I. Sridhar, and R. V. Ramanujan, “Self pumping magnetic cooling,” *J. Phys. D. Appl. Phys.*, vol. 50, no. 3, 2017.
- [53] M. Petit, Y. Avenas, A. Kedous-Lebouc, W. Cherief, and E. Rullière, “Experimental study of a static system based on a magneto-thermal coupling in ferrofluids,” in *International Journal of Refrigeration*, 2014, vol. 37, no. 1, pp. 201–208.
- [54] R. J. Yang, H. H. Hou, Y. N. Wang, and L. M. Fu, “Micro-magnetofluidics in microfluidic systems: A review,” *Sensors and Actuators, B: Chemical*, vol. 224. Elsevier B.V., pp. 1–15, 2016.
- [55] E. Aursand, M. A. Gjennestad, K. Y. Lervåg, and H. Lund, “Potential of enhancing a natural convection loop with a thermomagnetically pumped ferrofluid,” *J. Magn. Magn. Mater.*, vol. 417, no. 7465, pp. 148–159, 2016.
- [56] A. E. Virden and K. O’grady, “The temperature dependence of magnetization in ferrofluids,” *J. Appl. Phys.*, vol. 99, no. 8, pp. 99–101, 2006.
- [57] S. J. Kemp, R. M. Ferguson, A. P. Khandhar, and K. M. Krishnan, “Monodisperse magnetite nanoparticles with nearly ideal saturation magnetization,” *RSC Adv.*, vol. 6, no. 81, pp. 77452–77464, 2016.
- [58] P. S. B. Szabo, M. Beković, and W. G. Früh, “Using infrared thermography to investigate thermomagnetic convection under spatial non-uniform magnetic field,” *Int. J. Therm. Sci.*, vol. 116, pp. 118–128, 2017.
- [59] P. S. B. Szabo and W. Früh, “Journal of Magnetism and Magnetic Materials The transition

- from natural convection to thermomagnetic convection of a magnetic fluid in a non-uniform magnetic field,” *J. Magn. Magn. Mater.*, vol. 447, pp. 116–123, 2018.
- [60] A. F. Pshenichnikov and V. V. Mekhonoshin, “Equilibrium magnetization and microstructure of the system of superparamagnetic interacting particles: numerical simulation,” *J. Magn. Magn. Mater.*, vol. 213, no. 3, pp. 357–369, 2000.
- [61] M. Goharkhah, M. Ashjaee, and M. Shahabadi, “Experimental investigation on convective heat transfer and hydrodynamic characteristics of magnetite nanofluid under the influence of an alternating magnetic field,” *Int. J. Therm. Sci.*, vol. 99, pp. 113–124, 2016.
- [62] H. C. Brinkman, “the Viscosity of Concentrated Suspensions,” *J. Chem. Phys.*, vol. 20, no. 4, 1952.
- [63] A. Salehpour and M. Ashjaee, “Effect of different frequency functions on ferrofluid FHD flow,” *J. Magn. Magn. Mater.*, vol. 480, no. February, pp. 112–131, 2019.
- [64] J. Coey, *Magnetism and Magnetic Materials*. Cambridge University Press, 2010.
- [65] A. O. Ivanov and O. B. Kuznetsova, “Magnetic properties of dense ferrofluids,” *J. Magn. Magn. Mater.*, vol. 252, no. 1-3 SPEC. ISS., pp. 135–137, 2002.
- [66] H. P. Langtangen, K.-A. Mardal, and R. Winther, “Numerical methods for incompressible viscous flow,” *Adv. Water Resour.*, vol. 25, no. 8–12, pp. 1125–1146, 2002.
- [67] C. Multiphysics, “CFD Module User ’s Guide,” *COMSOL Multiphysics*, 2016.
- [68] COMSOL Multiphysics, “Heat Transfer Module,” *Manual*, pp. 1–222, 2015.
- [69] COMSOL, “Comsol Multiphysics Reference Manual (Version 4.3b),” 2013.
- [70] J. C. Tannehill, D. A. Anderson, and R. H. Pletcher, “Computational fluid mechanics and heat transfer,” *[Book] Taylor Fr.*, 1997.
- [71] J. F. Wendt *et al.*, *Computational fluid dynamics: An introduction*. 2009.

- [72] D. Briand, E. Yeatman, and S. Roundy, *Micro Energy Harvesting*. Wiley-VCH, 2015.
- [73] A. Niell, Elvin and Erturk, *Advances in Energy Harvesting Methods*. Springer, 2012.
- [74] D. J. Inman, *Piezoelectric energy harvesting*. 2011.
- [75] B. P. D. Mitcheson *et al.*, “Human and Machine Motion for Wireless Electronic Devices,” vol. 96, no. 9, pp. 1457–1486, 2008.
- [76] S. Wang, L. Lin, and Z. Lin, “Triboelectric nanogenerators as self-powered active sensors,” *Nano Energy*, vol. 11, pp. 436–462, 2015.
- [77] S. Materials, “A piezoelectric vibration based generator,” 2006.
- [78] V. R. Challa, M. G. Prasad, Y. Shi, and F. T. Fisher, “A vibration energy harvesting device with bidirectional resonance frequency tunability,” 2008.
- [79] N. Thambi and A. M. Sastry, “Powering MEMS portable devices — a review of non-regenerative and regenerative power supply systems with special emphasis on piezoelectric energy,” 2008.
- [80] F. Cottone, H. Vocca, and L. Gammaitoni, “Nonlinear Energy Harvesting,” vol. 080601, no. February, pp. 1–4, 2009.
- [81] A. Erturk, W. G. R. Vieira, C. De Marqui, and D. J. Inman, “On the energy harvesting potential of piezoaeroelastic systems,” vol. 184103, no. 2010, 2014.
- [82] M. Seol, S. Jeon, J. Han, and Y. Choi, “Ferrofluid-based triboelectric-electromagnetic hybrid generator for sensitive and sustainable vibration energy harvesting,” *Nano Energy*, vol. 31, no. October 2016, pp. 233–238, Jan. 2017.
- [83] I. Related and T. O. The, “ENERGY HARVESTING EEL,” vol. 0, pp. 629–640, 2001.
- [84] S. R. Anton and H. A. Sodano, “A review of power harvesting using piezoelectric materials (2003 – 2006),” 2007.

- [85] L. Zuo and X. Tang, "Large-scale vibration energy harvesting," vol. 24, no. 11, pp. 1405–1430, 2013.
- [86] S. Naifar, S. Bradai, C. Viehweger, and O. Kanoun, "Survey of electromagnetic and magnetoelectric vibration energy harvesters for low frequency excitation," *Meas. J. Int. Meas. Confed.*, vol. 106, pp. 251–263, 2017.
- [87] M. Shahinpoor and K. J. Kim, "Ionic polymer – metal composites : I .," 2001.
- [88] K. J. Kim and M. Shahinpoor, "Ionic polymer – metal composites : II .," 2003.
- [89] M. Shahinpoor and K. J. Kim, "Ionic polymer – metal composites : III . Modeling and simulation as biomimetic sensors , actuators , transducers , and," 2004.
- [90] M. Shahinpoor and K. J. Kim, "Ionic polymer – metal composites : IV .," 2005.
- [91] A. Giacomello, M. Porfiri, A. Giacomello, and M. Porfiri, "Underwater energy harvesting from a heavy flag hosting ionic polymer metal composites," vol. 084903, 2011.
- [92] M. Shelley, N. Vandenberghe, and J. Zhang, "Heavy Flags Undergo Spontaneous Oscillations in Flowing Water," vol. 094302, no. March, 2005.
- [93] R. Tiwari and K. J. Kim, "IPMC as a mechanoelectric energy harvester : tailored properties," 2013.
- [94] L. Alamos, "An Energy Harvesting Comparison of Piezoelectric and Ionically Conductive Polymers," vol. 20, no. March, pp. 633–642, 2009.
- [95] R. Tiwari and E. Garcia, "The state of understanding of ionic polymer metal composite architecture : a," 2011.
- [96] F. Cellini, J. Pounds, S. D. Peterson, and M. Por, "Underwater energy harvesting from a turbine hosting ionic polymer metal composites."
- [97] Y. Cha, L. Shen, and M. Porfiri, "Energy harvesting from underwater torsional vibrations

- of a patterned ionic polymer metal composite.”
- [98] F. Cellini, Y. Cha, and M. Porfiri, “Energy harvesting from fluid-induced buckling of ionic polymer metal composites,” vol. 25, no. 12, pp. 1496–1510, 2014.
- [99] M. Aureli, C. Prince, M. Porfiri, and S. D. Peterson, “Energy harvesting from base excitation of ionic polymer metal composites in fluid environments,” 2010.
- [100] K. Abdelnour, E. Mancia, and S. D. Peterson, “Hydrodynamics of underwater propulsors based on ionic polymer – metal composites : a numerical study,” 2009.
- [101] J. M. Mcdonough, “COMPUTATIONAL FLUID DYNAMICS of INCOMPRESSIBLE FLOW : Mathematics , Algorithms and Implementations,” *Book*, p. 155, 2007.
- [102] S. D. Peterson, M. Porfiri, S. D. Peterson, and M. Porfiri, “Energy exchange between a vortex ring and an ionic polymer metal composite Energy exchange between a vortex ring and an ionic polymer metal composite,” vol. 114102, no. 2012, 2015.
- [103] S. D. Peterson and M. Porfiri, “Interaction of a vortex pair with a flexible plate in an ideal quiescent fluid,” vol. 23, no. 13, pp. 1485–1504, 2012.
- [104] D. J. Leo, *ENGINEERING ANALYSIS OF SMART. .*
- [105] J. Hu, Y. Cha, M. Por, and S. D. Peterson, “Energy harvesting from a vortex ring impinging on an annular ionic polymer metal composite.”
- [106] R. Kamakoti and W. Shyy, “Fluid-structure interaction for aeroelastic applications,” *Prog. Aerosp. Sci.*, vol. 40, no. 8, pp. 535–558, 2004.
- [107] H. D. Akaydin, N. Elvin, and Y. Andreopoulos, “Energy harvesting from highly unsteady fluid flows using piezoelectric materials,” in *Journal of Intelligent Material Systems and Structures*, 2010, vol. 21, no. 13, pp. 1263–1278.
- [108] V. Á. González, A. Z. Cruz, C. E. Arjonilla, D. P. Zepeda, and C. S. Forgach, *Selected*

Topics of Computational and Experimental Fluid Mechanics. 2015.

- [109] S. P. Kiselev, E. V. Vorozhtsov, and V. M. Fomin, *Foundations of Fluid Mechanics with Applications*. Birkhäuser, 2017.
- [110] H. D. Akayd and N. Elvin, “Wake of a cylinder : a paradigm for energy harvesting with piezoelectric materials,” pp. 291–304, 2010.
- [111] L. Ding, L. Zhang, C. Wu, X. Mao, and D. Jiang, “Flow induced motion and energy harvesting of bluff bodies with different cross sections,” *Energy Convers. Manag.*, vol. 91, pp. 416–426, 2015.
- [112] C. De Marqui and D. J. Inman, “Modeling and Analysis of Piezoelectric Energy Harvesting From Aeroelastic Vibrations Using the Doublet-Lattice Method,” vol. 133, no. February 2011, pp. 1–9, 2018.
- [113] S. Priya, “Advances in energy harvesting using low profile piezoelectric transducers,” pp. 165–182, 2007.
- [114] Y. Xia, S. Michelin, and O. Doaré, “Fluid-Solid-Electric Lock-In of Energy-Harvesting Piezoelectric Flags,” vol. 014009, pp. 1–8, 2015.
- [115] Y. Wu, D. Li, J. Xiang, and A. Da, “Piezoaeroelastic energy harvesting based on an airfoil with double plunge degrees of freedom : Modeling and numerical analysis,” *J. Fluids Struct.*, vol. 74, pp. 111–129, 2017.
- [116] J. S. Bae and D. J. Inman, “Aeroelastic characteristics of linear and nonlinear piezo-aeroelastic energy harvester,” *J. Intell. Mater. Syst. Struct.*, vol. 25, no. 4, pp. 401–416, 2014.
- [117] J. A. Dunnmon, S. C. Stanton, B. P. Mann, and E. H. Dowell, “Power extraction from aeroelastic limit cycle oscillations,” *J. Fluids Struct.*, vol. 27, no. 8, pp. 1182–1198, 2011.

- [118] D. Li, Y. Wu, A. Da, and J. Xiang, "Progress in Aerospace Sciences Energy harvesting by means of flow-induced vibrations on aerospace vehicles," *Prog. Aerosp. Sci.*, vol. 86, pp. 28–62, 2016.
- [119] V. Tech, "Piezoaeroelastic Modeling and Analysis of a Generator Wing with Continuous and Segmented Electrodes," vol. 21, no. July, 2010.
- [120] L. Wu, L. Chen, and C. Liu, "Acoustic pressure in cavity of variously sized two-dimensional sonic crystals with various filling fractions," *Phys. Lett. A*, vol. 373, no. 12–13, pp. 1189–1195, 2009.
- [121] L. Wu, L. Chen, and C. Liu, "Experimental investigation of the acoustic pressure in cavity of a two-dimensional sonic crystal," vol. 404, pp. 1766–1770, 2009.
- [122] W. Wang, L. Wu, and L. Chen, "Acoustic energy harvesting by piezoelectric curved beams in the cavity of a sonic crystal," 2010.
- [123] A. Yang *et al.*, "Enhanced Acoustic Energy Harvesting Using Coupled Resonance Structure of Sonic Crystal and Helmholtz Resonator," 2013.
- [124] L. Wu, L. Chen, C. Liu, L. Wu, L. Chen, and C. Liu, "Acoustic energy harvesting using resonant cavity of a sonic crystal Acoustic energy harvesting using resonant cavity of a sonic crystal," vol. 013506, no. 2009, 2016.
- [125] S. H. Chae *et al.*, "Electromagnetic vibration energy harvester using springless proof mass and ferrofluid as a lubricant," in *Journal of Physics: Conference Series*, 2013, vol. 476, no. 1.
- [126] R. Arulmurugan, G. Vaidyanathan, S. Sendhilnathan, and B. Jeyadevan, "Mn-Zn ferrite nanoparticles for ferrofluid preparation: Study on thermal-magnetic properties," *J. Magn. Mater.*, vol. 298, no. 2, pp. 83–94, 2006.

- [127] D. Wang and K. Chang, "Electromagnetic energy harvesting from flow induced vibration," *Microelectronics J.*, vol. 41, no. 6, pp. 356–364, 2010.
- [128] S. F. Alazemi, A. Bibo, and M. F. Daqaq, "A ferrofluid-based energy harvester: An experimental investigation involving internally-resonant sloshing modes," *Eur. Phys. J. Spec. Top.*, vol. 224, no. 14–15, pp. 2993–3004, 2015.
- [129] R. A. Ibrahim, *Liquid Sloshing Dynamics*. University Press, Cambridge, 2005.
- [130] W. G. Price and Y. G. Chen, "A simulation of free surface waves for incompressible two-phase flows using a curvilinear level set formulation," *Int. J. Numer. Methods Fluids*, vol. 51, no. May 2005, pp. 305–330, 2006.
- [131] J. L. Bautista-Jacobo, E. Rodríguez-Morales, J. J. Montes-Rodríguez, and H. Gámez-Cuatzín, "Effect of Baffles on the Sloshing in Road Tankers Carrying LPG: A Comparative Numerical Study," *Math. Probl. Eng.*, vol. 2015, 2015.
- [132] Q. Liu, M. F. Daqaq, and G. Li, "Performance Analysis of a Ferrofluid-Based Electromagnetic Energy Harvester," *IEEE Trans. Magn.*, vol. 54, no. 5, 2018.
- [133] H. Ki, "Level set method for two-phase incompressible flows under magnetic fields," *Comput. Phys. Commun.*, vol. 181, no. 6, pp. 999–1007, 2010.
- [134] P. Capobianchi, M. Lappa, and M. S. N. Oliveira, "Deformation of a ferrofluid droplet in a simple shear flow under the effect of a constant magnetic field," *Comput. Fluids*, vol. 173, pp. 313–323, 2018.
- [135] S. Elgeti and H. Sauerland, "Deforming fluid domains within the finite element method," *Arch. Comput. Methods Eng.*, 2014.
- [136] J. A. Sethian, "Level Set Techniques for Tracking Interfaces: Fast Algorithms, Multiple Regions, Grid Generation and Shape/Character Recognition," *Proc. Int. Conf.*, 1994.

- [137] et al. Tryggvason, Grétar, “Fluid mechanics with interfaces,” in *Direct Numerical Simulations of Gas–Liquid Multiphase Flows*, Cambridge University Press, 2011, pp. 21–49.
- [138] J. A. Sethian, “Theory, algorithms, and applications of level set methods for propagating interfaces,” *Acta Numer.*, vol. 5, pp. 309–395, 1996.
- [139] J. A. Sethian and P. Smereka, “Level Set Methods for Fluid Interfaces,” *Annu. Rev. Fluid Mech.*, vol. 35, no. 1, pp. 341–372, 2003.
- [140] E. Olsson, G. Kreiss, and S. Zahedi, “A conservative level set method for two phase flow II,” *J. Comput. Phys.*, vol. 225, no. 1, pp. 785–807, 2007.
- [141] C. Walker and B. Müller, “a Conservative Level Set Method for Sharp Interface Multiphase Flow Simulation,” in *V European Conference on Computational Fluid Dynamics ECCOMAS CFD 2010*, 2010, no. June, pp. 14–17.
- [142] F. Gibou, L. Chen, D. Nguyen, and S. Banerjee, “A level set based sharp interface method for the multiphase incompressible Navier-Stokes equations with phase change,” *J. Comput. Phys.*, vol. 222, no. 2, pp. 536–555, 2007.
- [143] M. Fattori, “A level set and sharp interface approach for simulating incompressible two-phase flow,” 2014.
- [144] A. Sharma, “Level set method for computational multi-fluid dynamics: A review on developments, applications and analysis,” *Sadhana - Acad. Proc. Eng. Sci.*, vol. 40, no. 3, pp. 627–652, 2015.
- [145] L. Lu, S. Jiang, M. Zhao, and G. Tang, “Two-dimensional viscous numerical simulation of liquid sloshing in rectangular tank with / without baffles and comparison with potential flow solutions,” *Ocean Eng.*, vol. 108, pp. 662–677, 2015.

- [146] L. Battaglia, M. Cruchaga, M. Storti, J. D'Elía, J. Núñez Aedo, and R. Reinoso, "Numerical modelling of 3D sloshing experiments in rectangular tanks," *Appl. Math. Model.*, vol. 59, pp. 357–378, 2018.
- [147] L. Wang and F. G. Yuan, "Vibration energy harvesting by magnetostrictive material," *Smart Mater. Struct.*, vol. 17, no. 4, 2008.
- [148] J. M. McCarthy, S. Watkins, A. Deivasigamani, and S. J. John, "Fluttering energy harvesters in the wind: A review," *J. Sound Vib.*, vol. 361, pp. 355–377, 2016.
- [149] S. P. Beeby, M. J. Tudor, and N. M. White, "Energy harvesting vibration sources for microsystems applications," *Meas. Sci. Technol.*, vol. 17, no. 12, 2006.
- [150] S. Alazmi, Y. Xu, and M. F. Daqaq, "Harvesting energy from the sloshing motion of ferrofluids in an externally excited container: Analytical modeling and experimental validation," *Phys. Fluids*, vol. 28, no. 7, 2016.
- [151] W. J. Jasper and N. Anand, "A generalized variational approach for predicting contact angles of sessile nano-droplets on both flat and curved surfaces," *J. Mol. Liq.*, vol. 281, pp. 196–203, 2019.
- [152] COMSOL Multiphysics and COMSOL, "Structural Mechanics Module," *COMSOL Multiphysics*, p. 454, 2008.
- [153] G. S. Flynn, K. R. Weisbrod, R. M. Chamberlin, and S. L. Yarbrow, "Modeling Two Phase Fluid Flow in High Speed Countercurrent Chromatography," in *COMSOL Conference*, 2010, pp. 1–7.
- [154] Y. C. Shu and I. C. Lien, "Analysis of power output for piezoelectric energy harvesting systems," *Smart Mater. Struct.*, vol. 15, no. 6, pp. 1499–1512, 2006.
- [155] J. G. Smits, S. I. Dalke, and T. K. Cooney, "The constituent equations of piezoelectric

bimorphs,” *Sensors Actuators A. Phys.*, vol. 28, no. 1, pp. 41–61, 1991.

- [156] M. Zhu, E. Worthington, and J. Njuguna, “Analyses of power output of piezoelectric energy-harvesting devices directly connected to a load resistor using a coupled piezoelectric-circuit finite element method,” *IEEE Trans. Ultrason. Ferroelectr. Freq. Control*, vol. 56, no. 7, pp. 1309–1318, 2009.

APPENDICES

Appendix A: Surface Evolution for L =10 cm tank

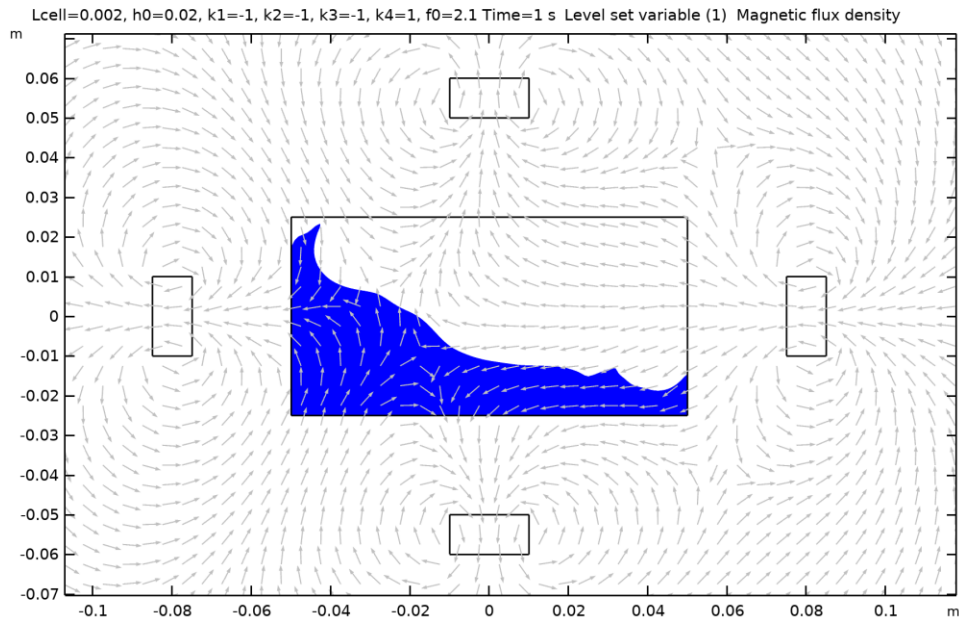


Figure 54 Case 2

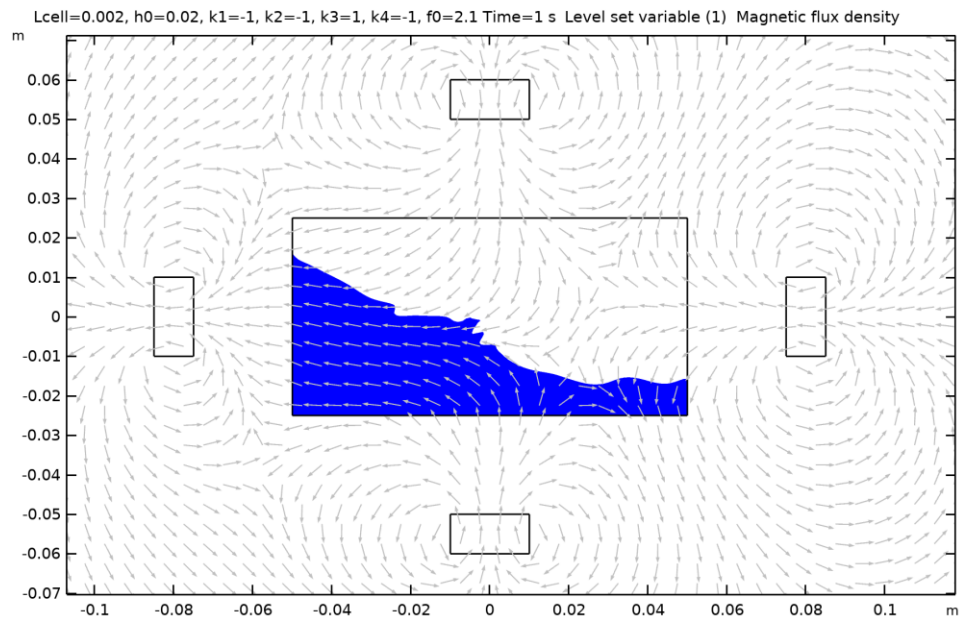


Figure 55 Case 3

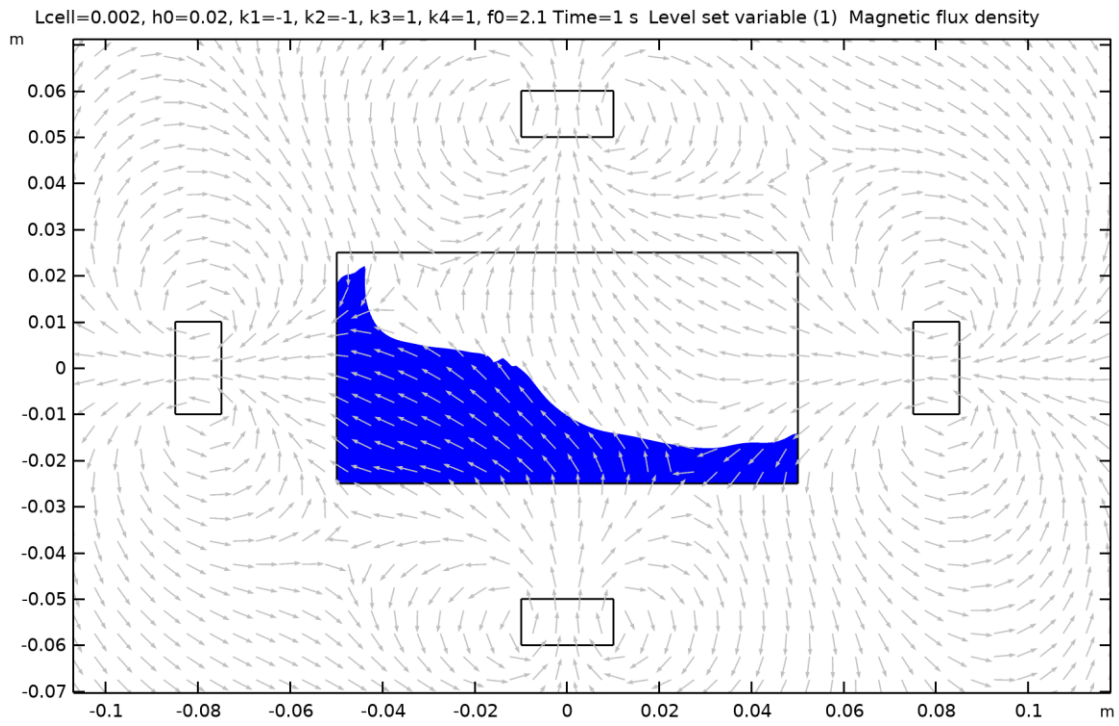


Figure 56 Case 4

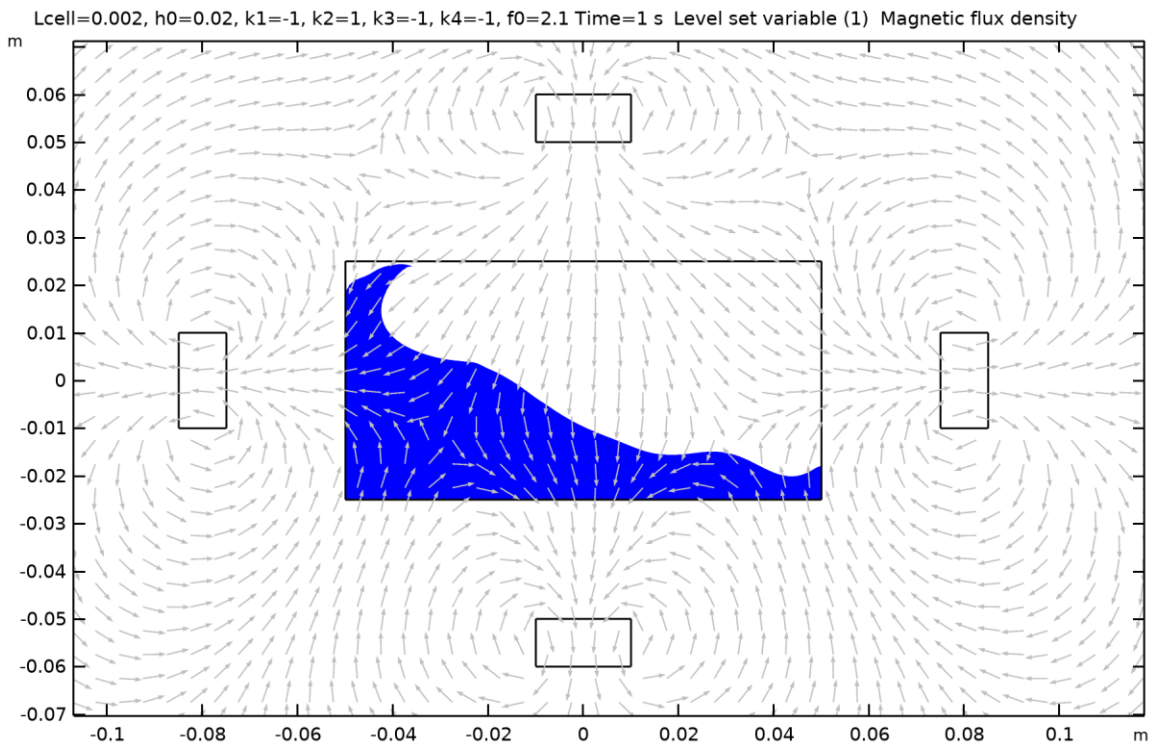


Figure 57 Case 5

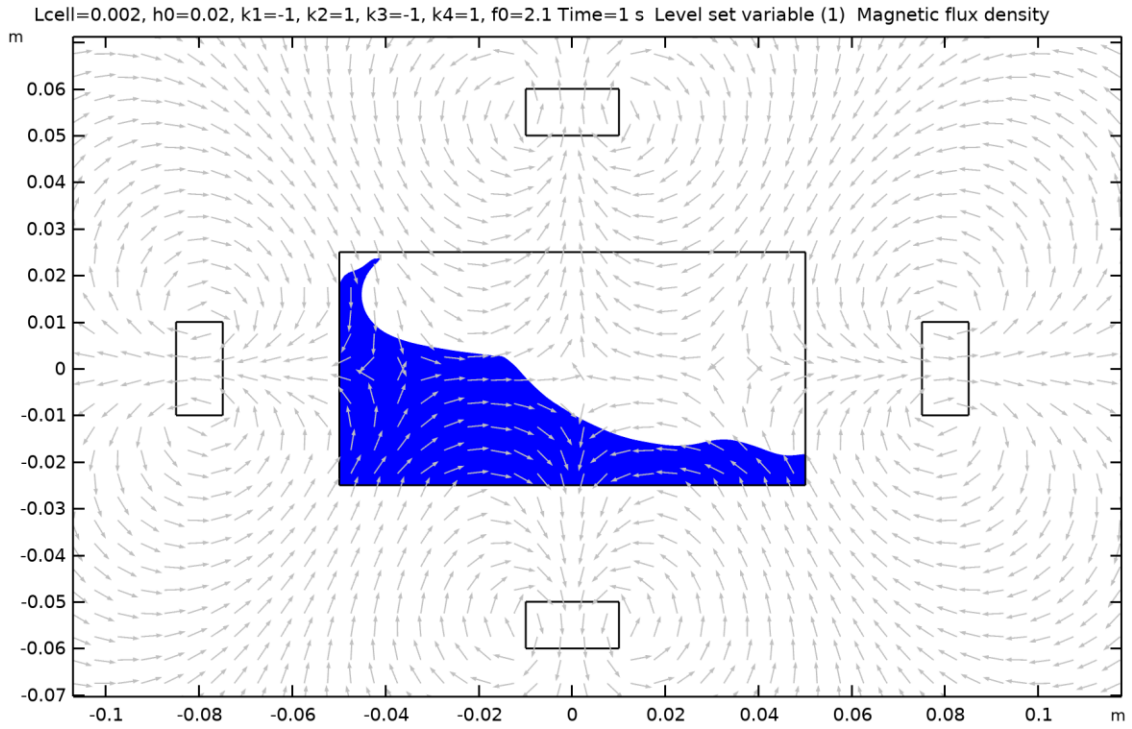


Figure 58 Case 6

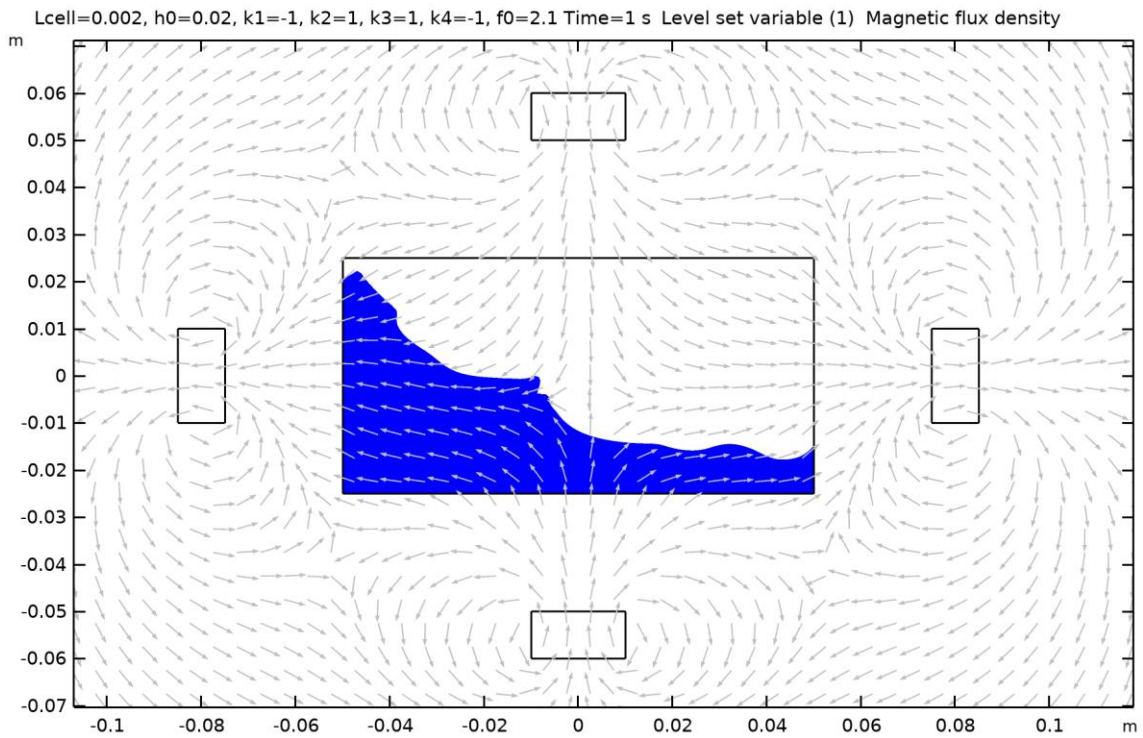


Figure 59 Case 7

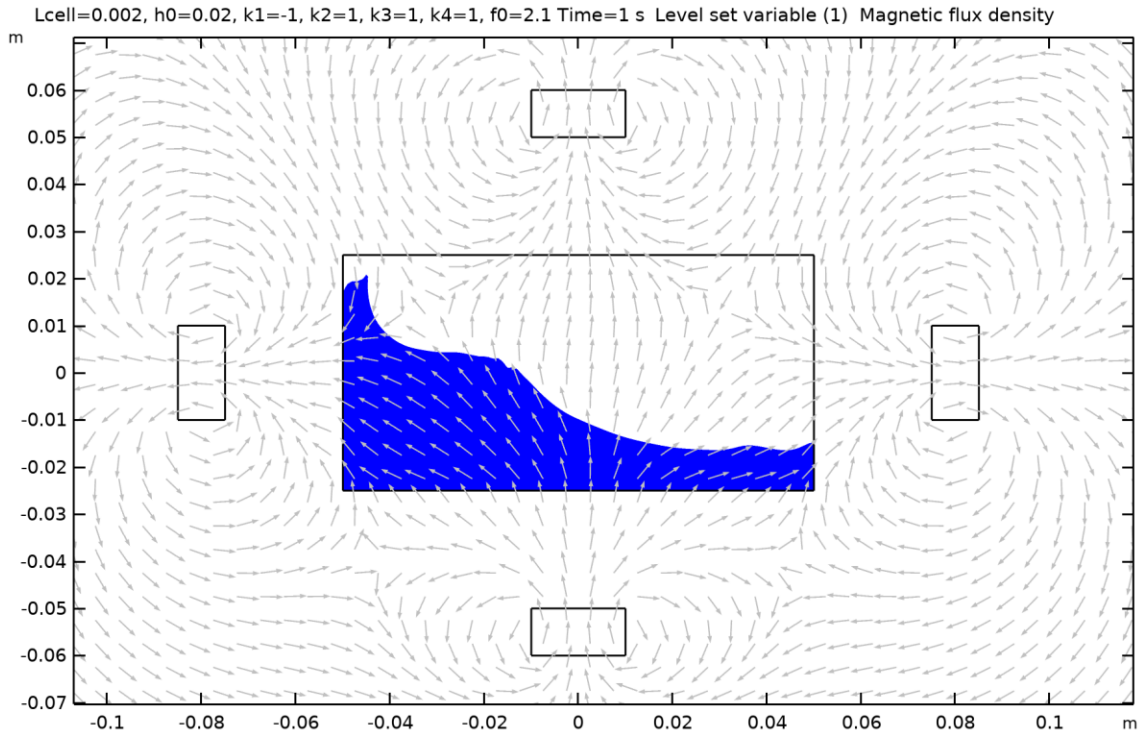


Figure 60 Case 8

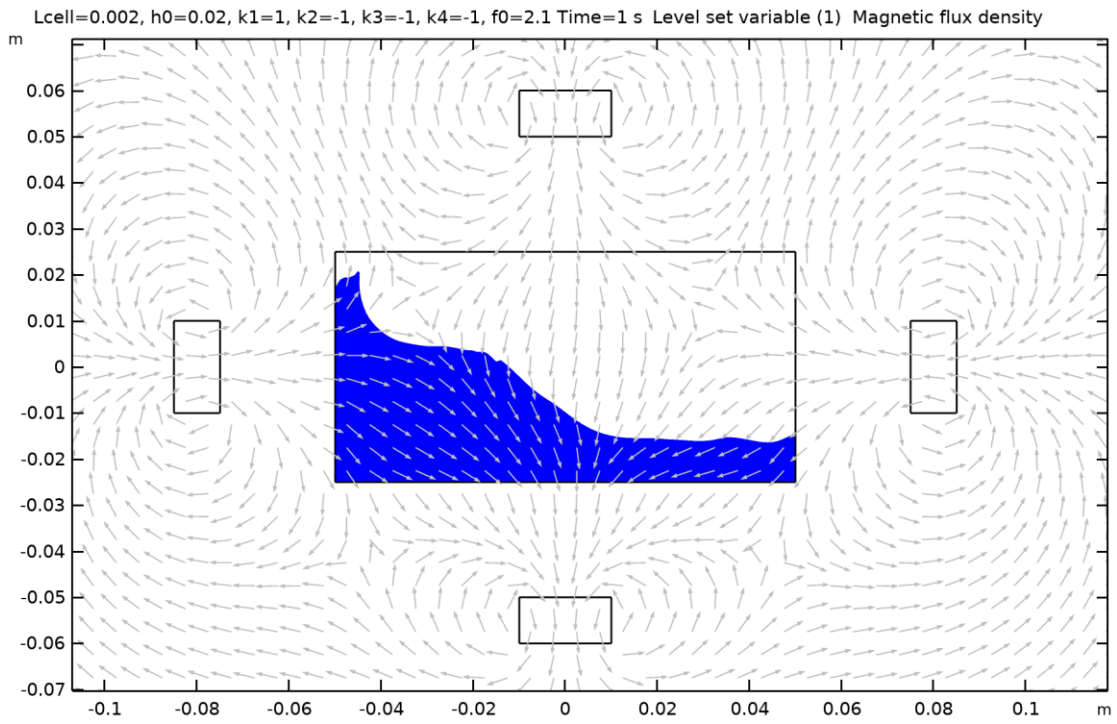


Figure 61 Case 9

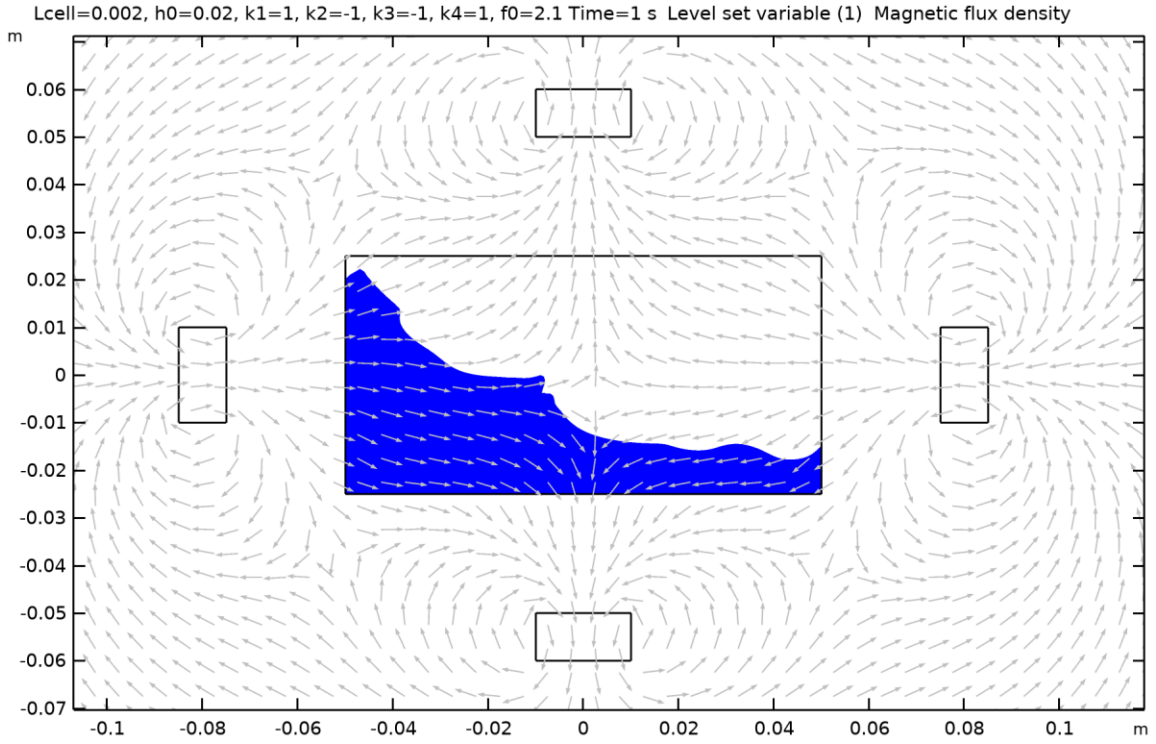


Figure 62 Case 10

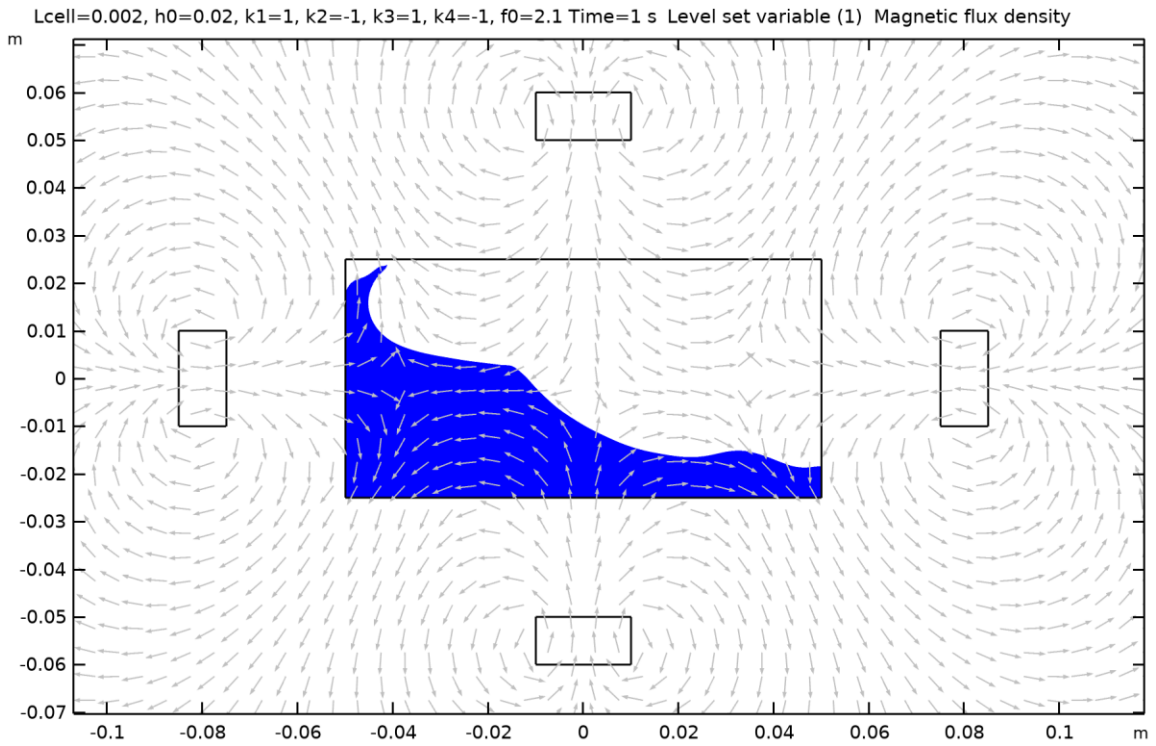


Figure 63 Case 11

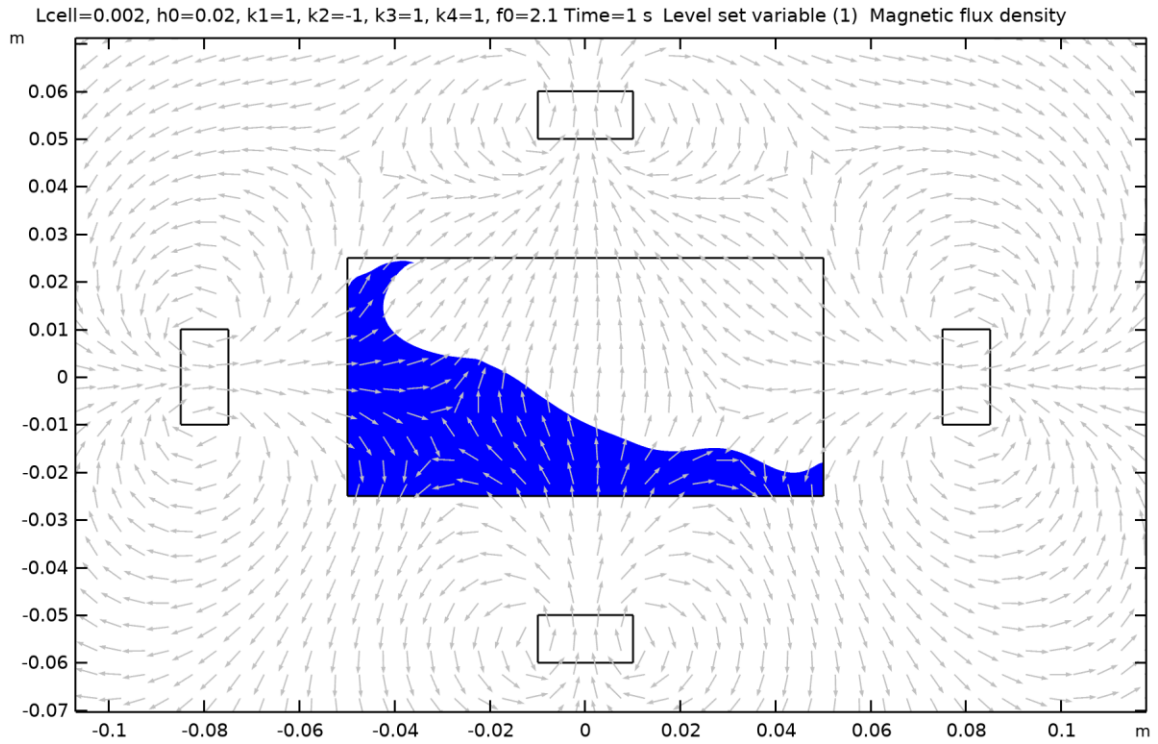


Figure 64 Case 12

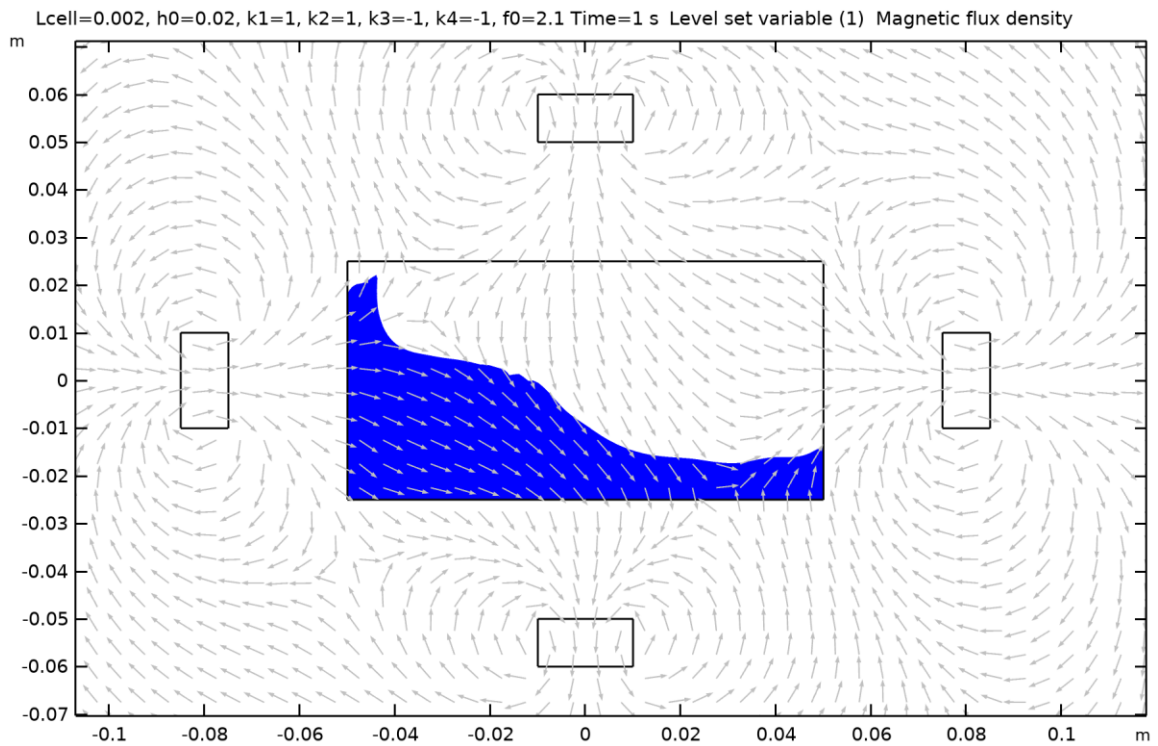


Figure 65 Case 13

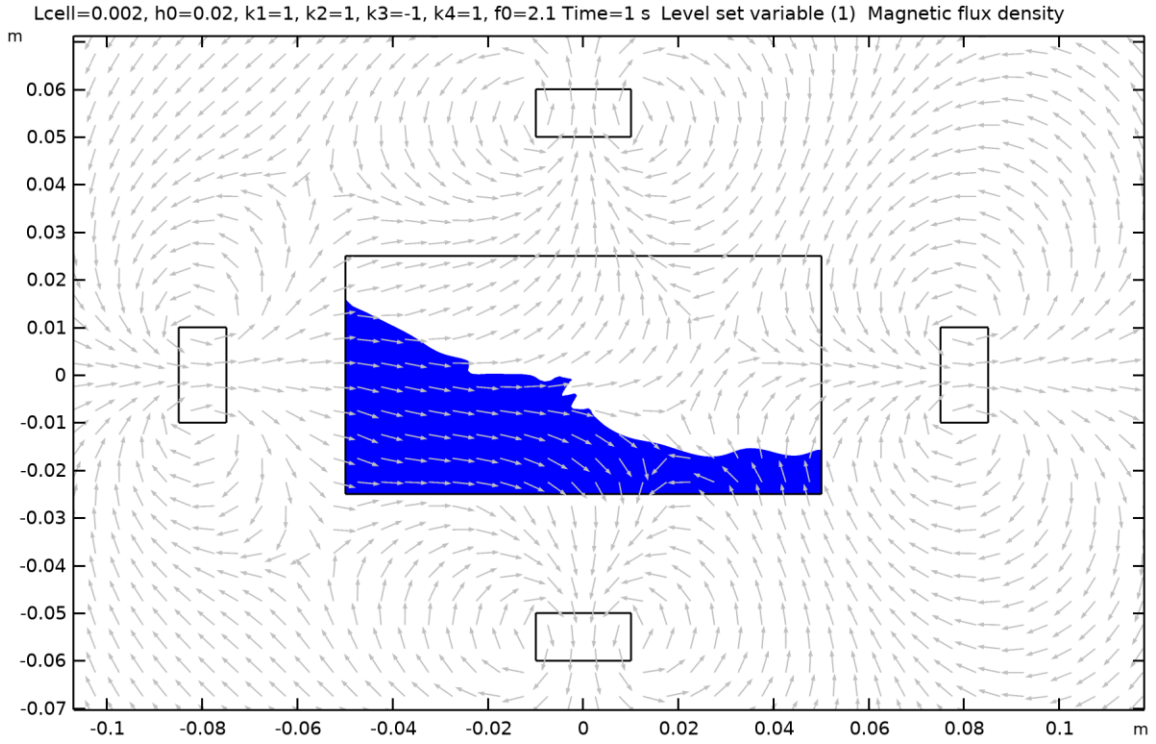


Figure 66 Case 14

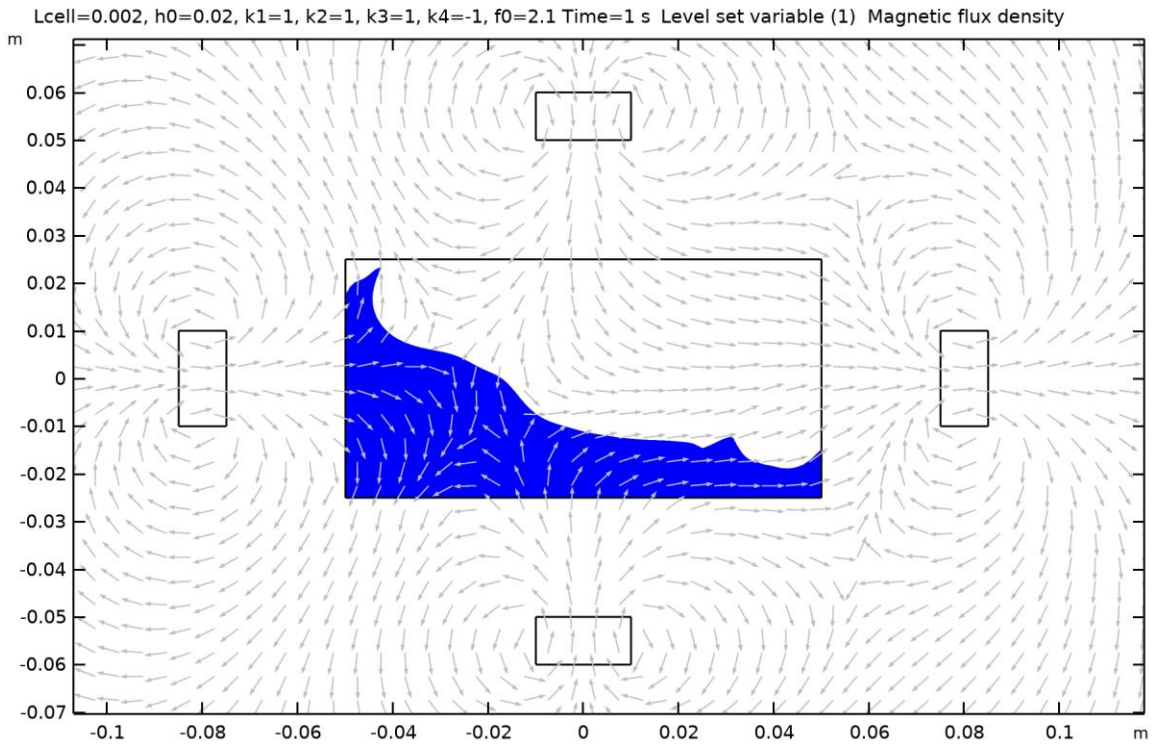


Figure 67 Case 15

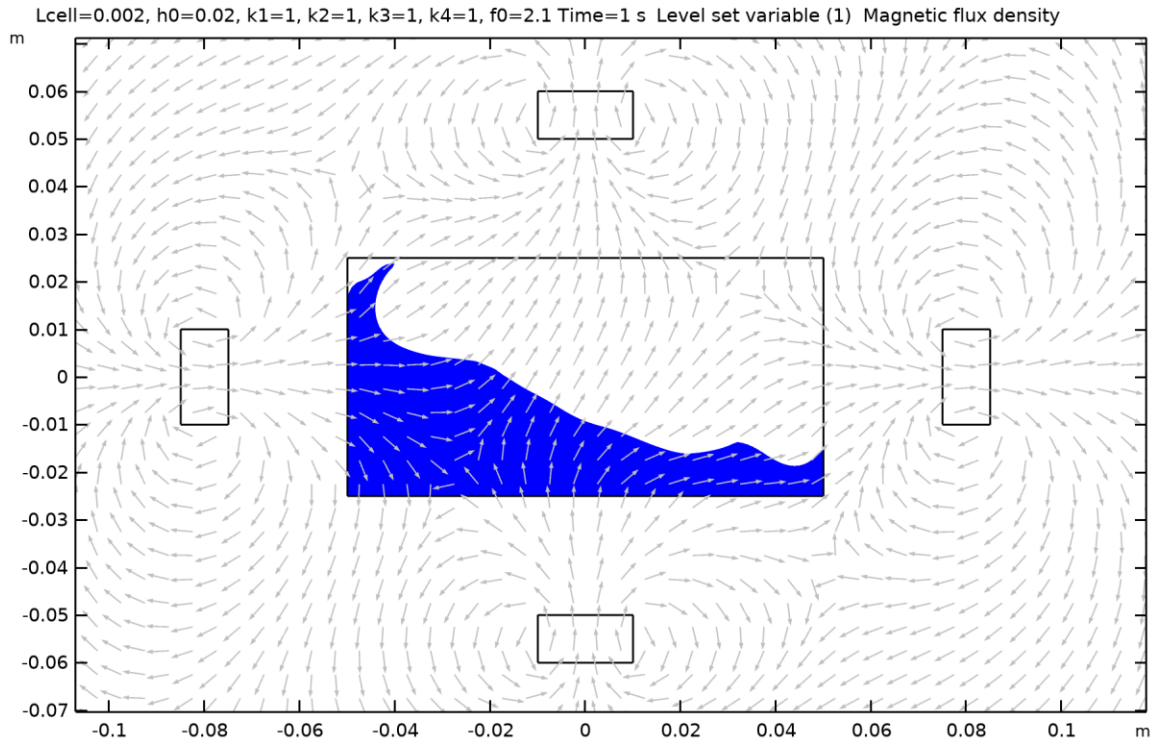


Figure 68 Case 16

Appendix B: Voltage Evolution plots for different cases

1. For PZT7A

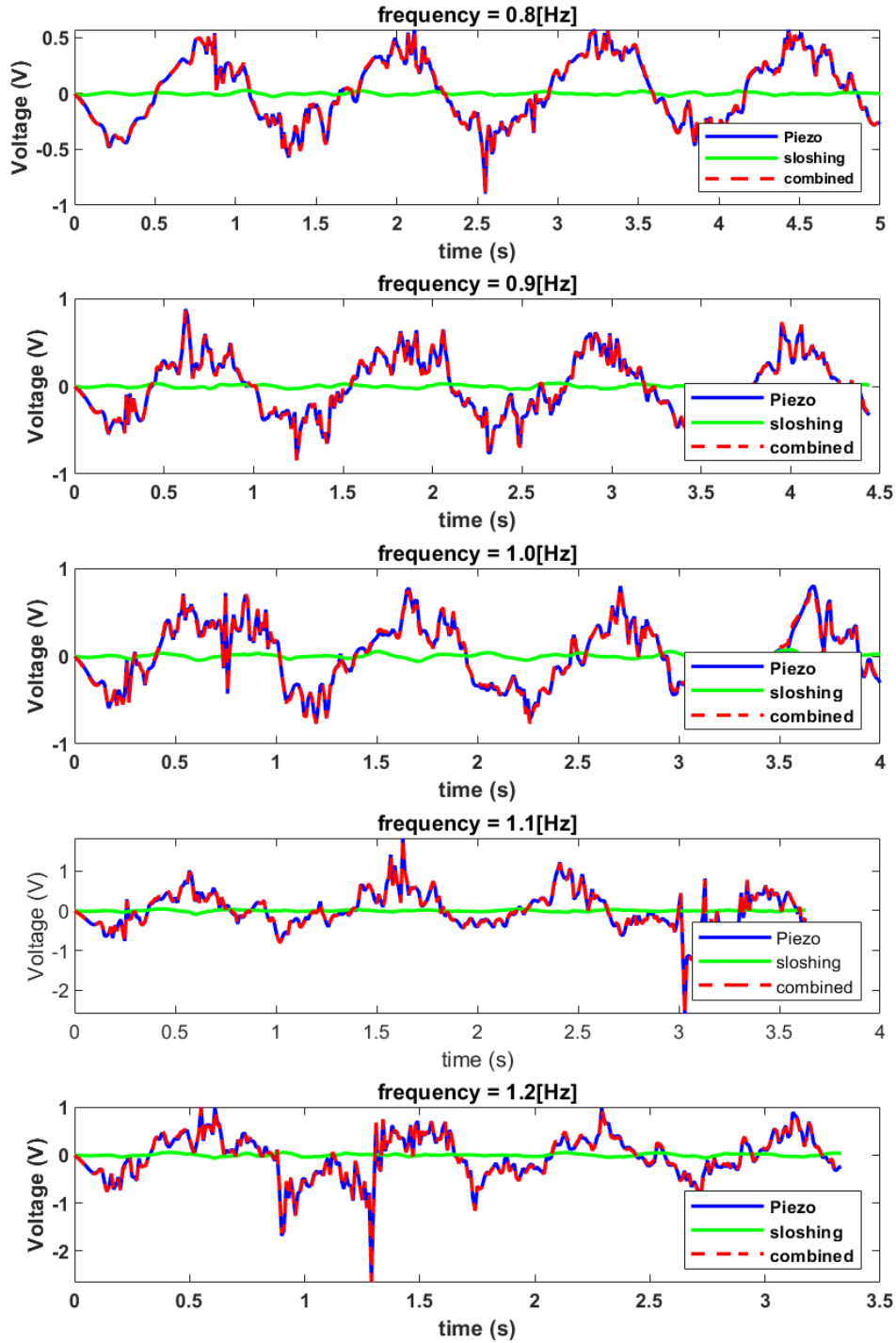


Figure 69 Case1 time evolution for different frequencies with PZT7A

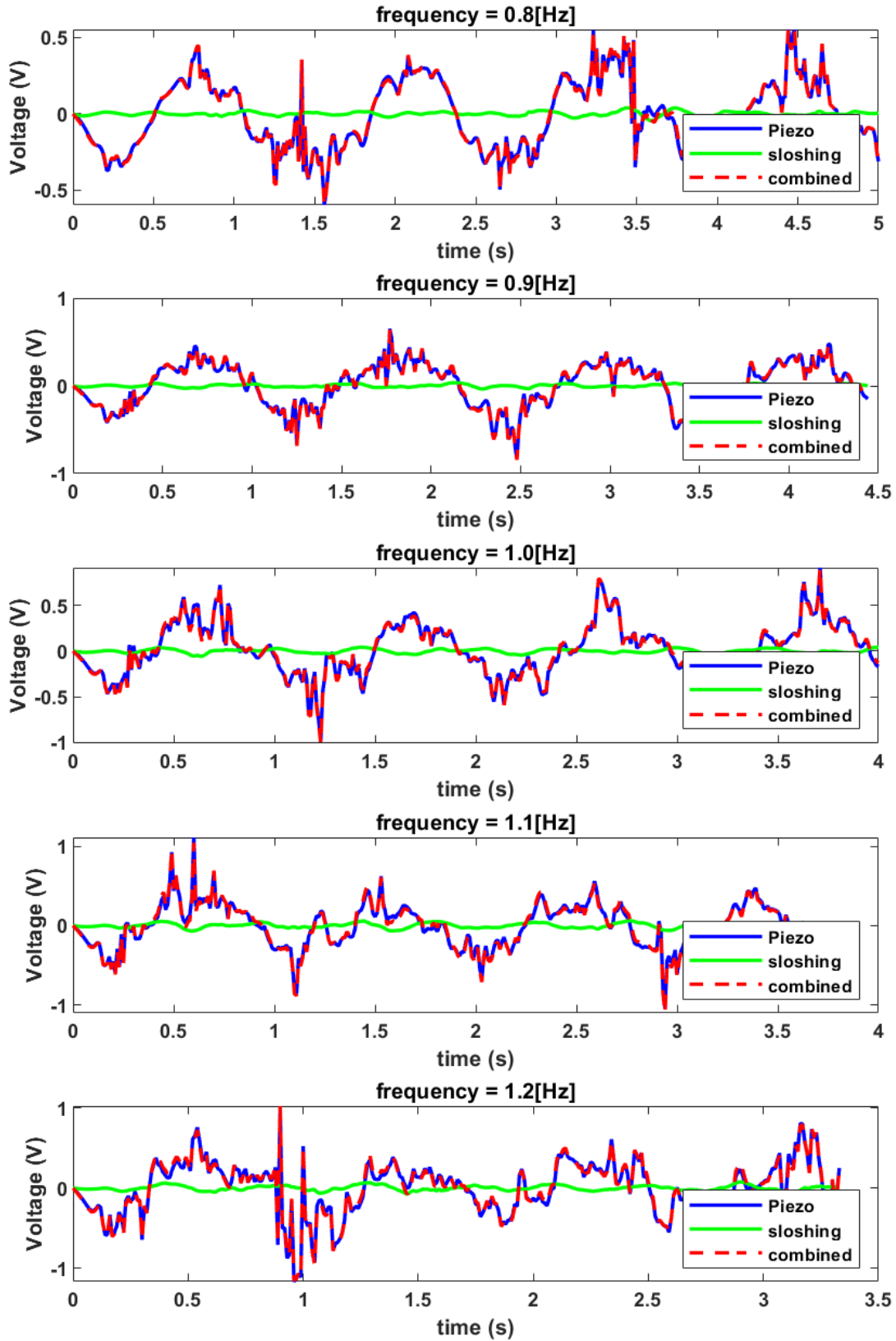


Figure 70 Case2 time evolution for different frequencies with PZT7A

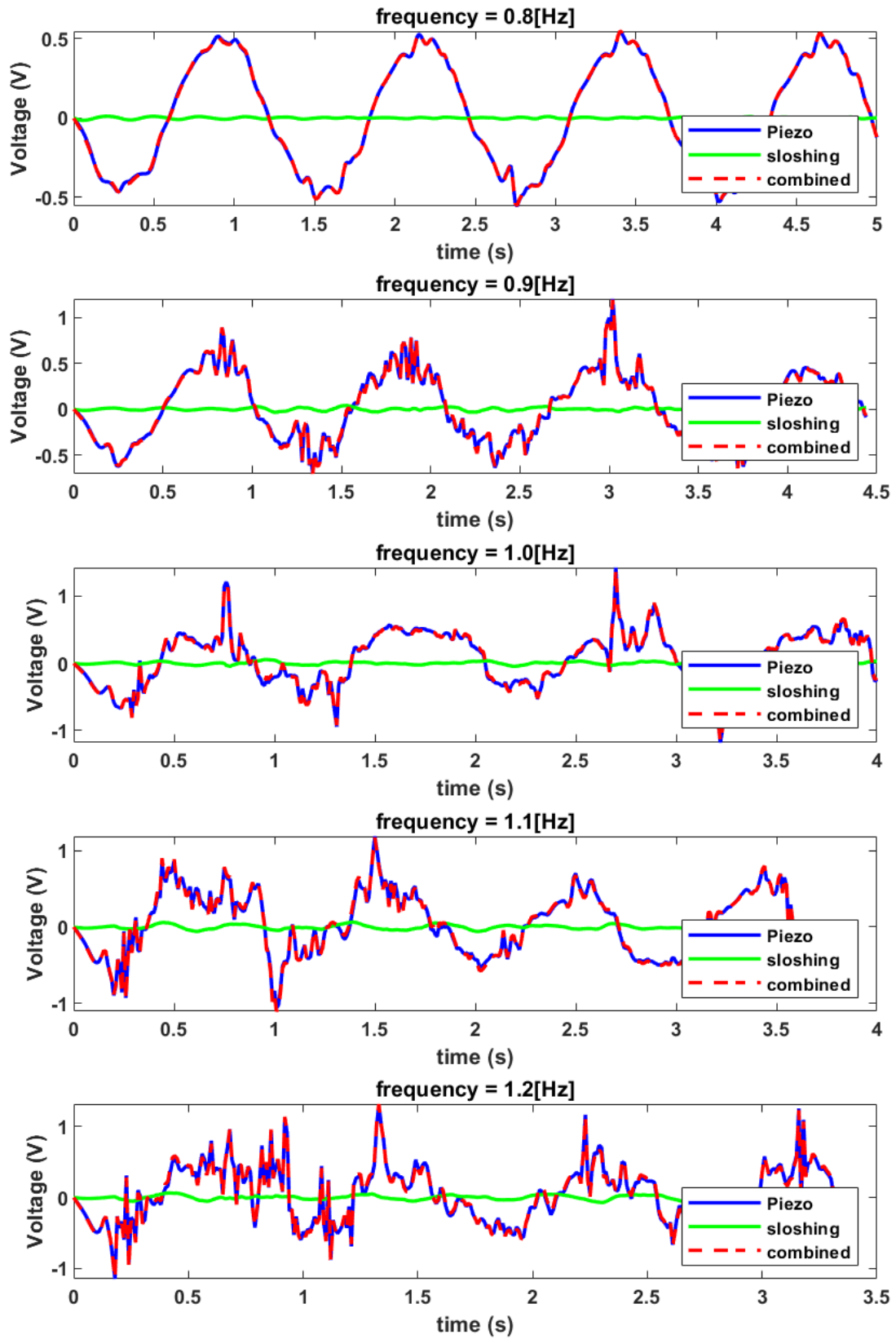


Figure 71 Case3 time evolution for different frequencies with PZT7A

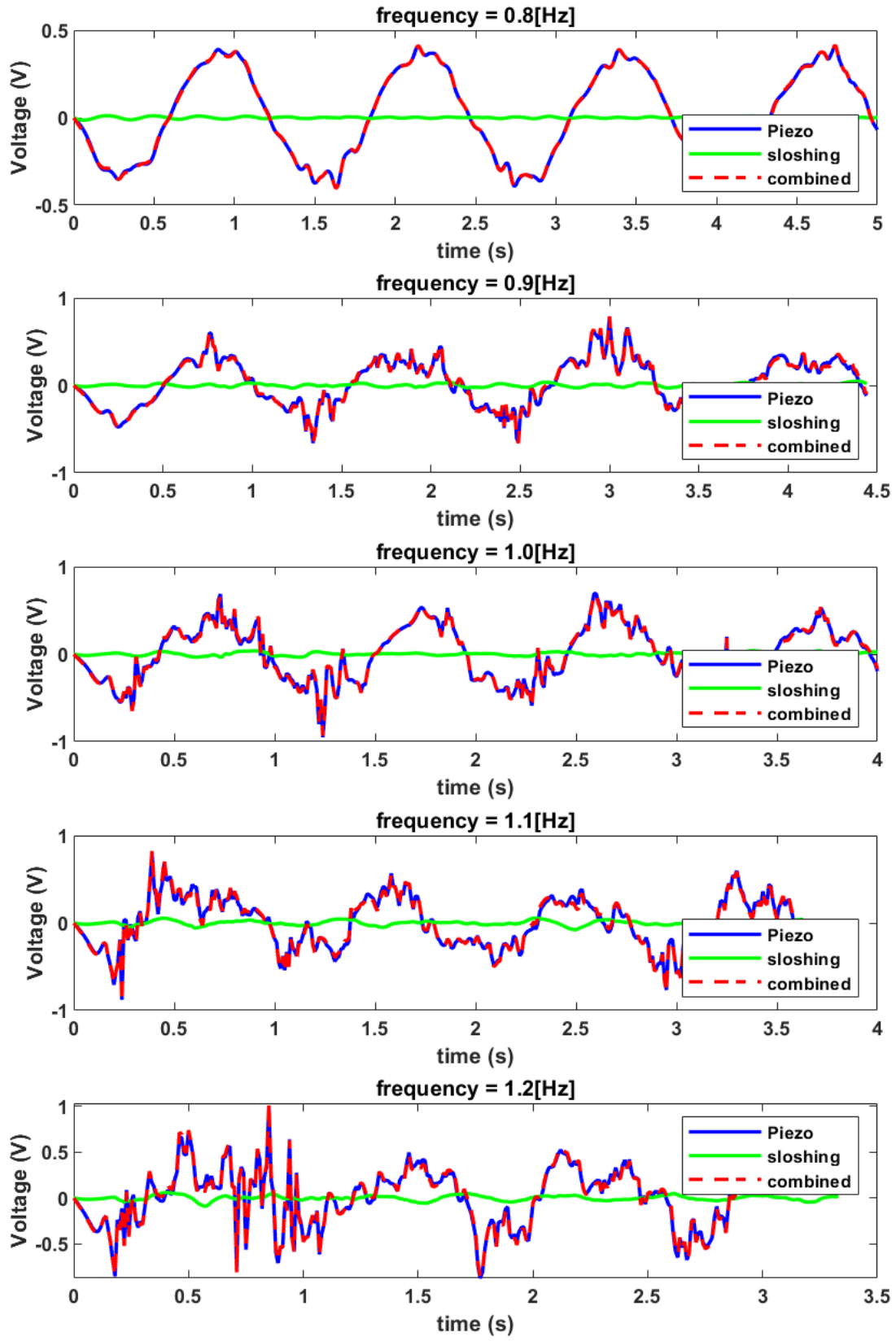


Figure 72 Case4 time evolution for different frequencies with PZT7A

2. For PVDF

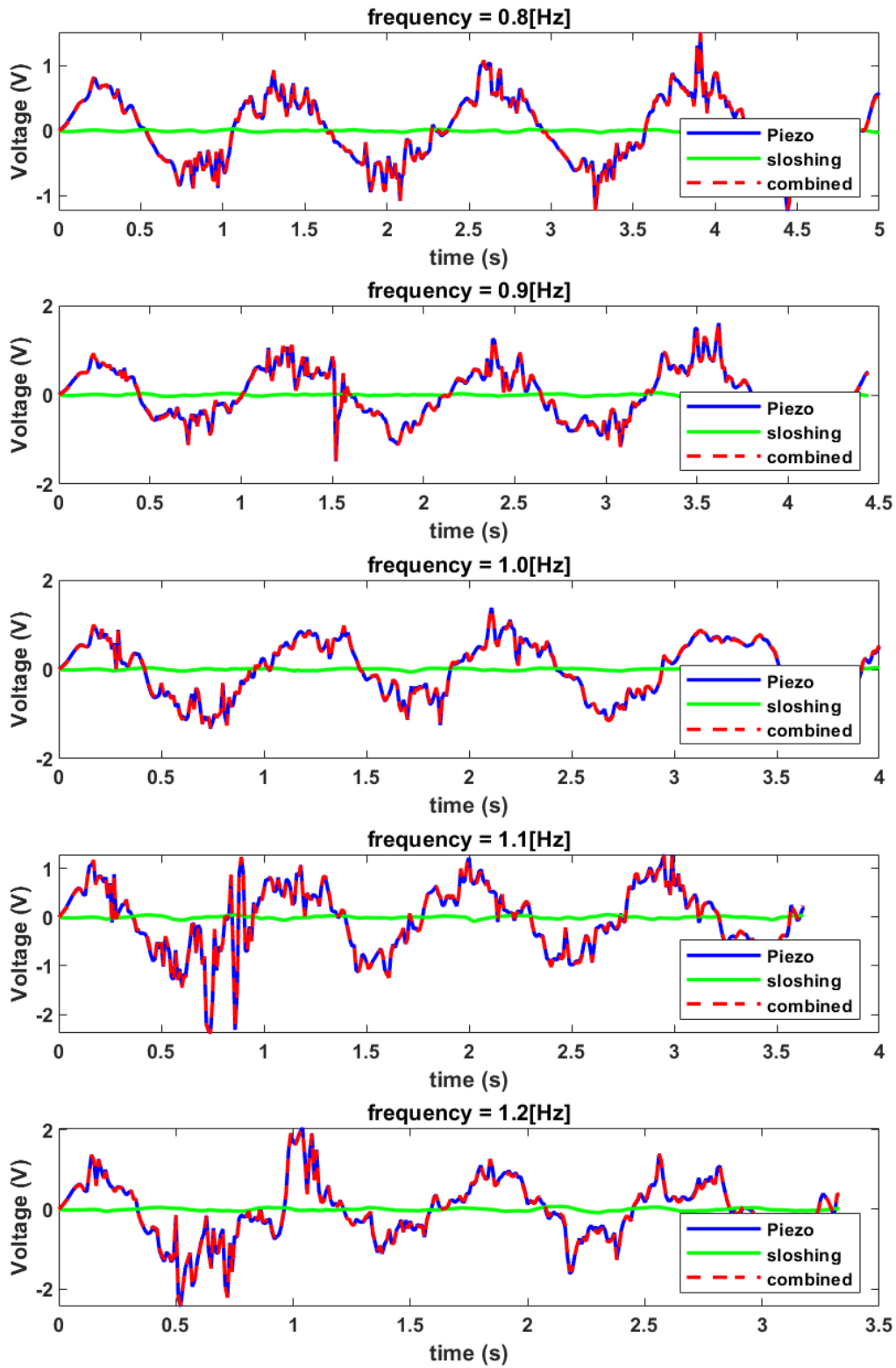


Figure 73 Case1 time evolution for different frequencies with PVDF

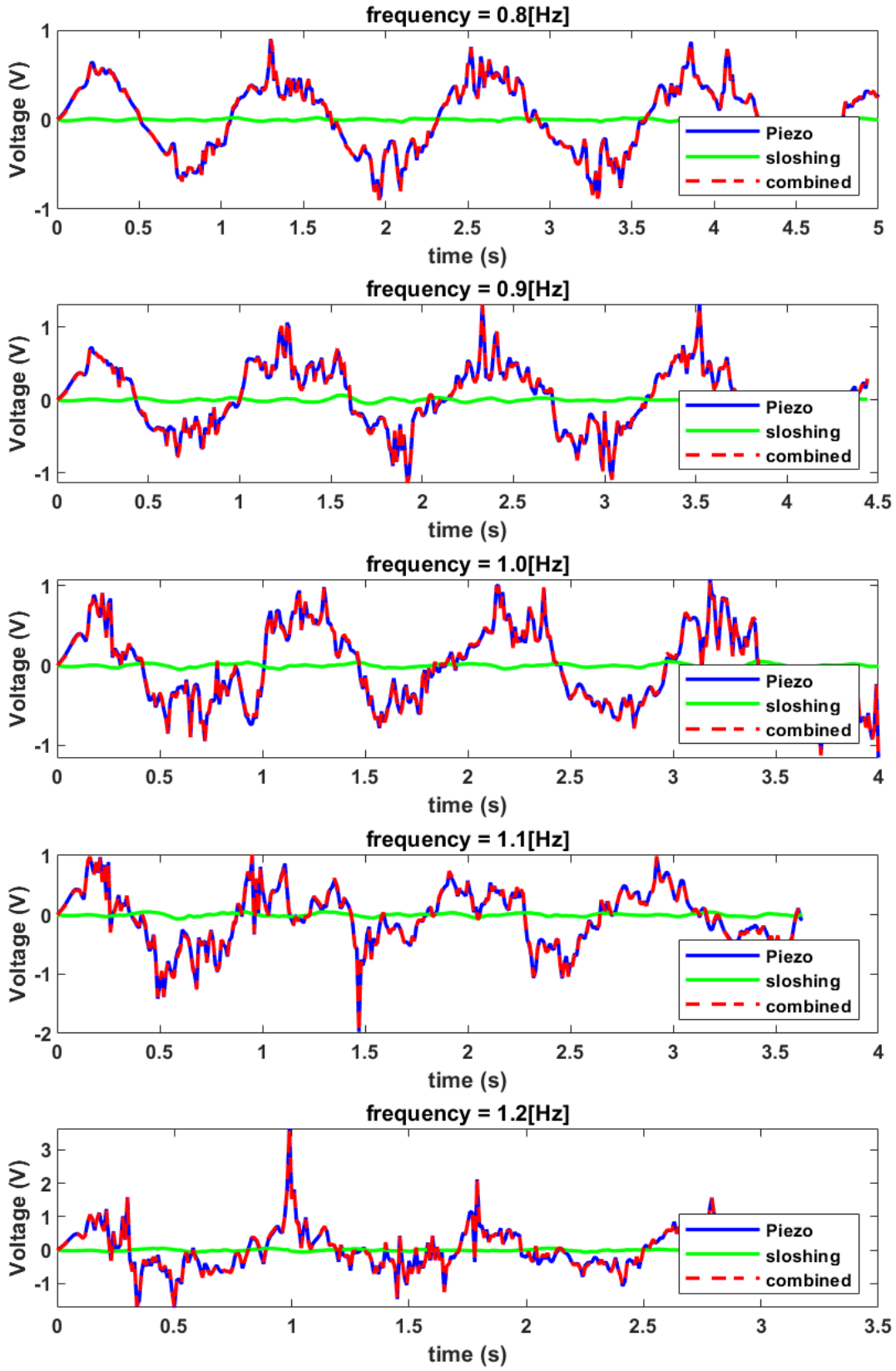


Figure 74 Case2 time evolution for different frequencies with PVDF

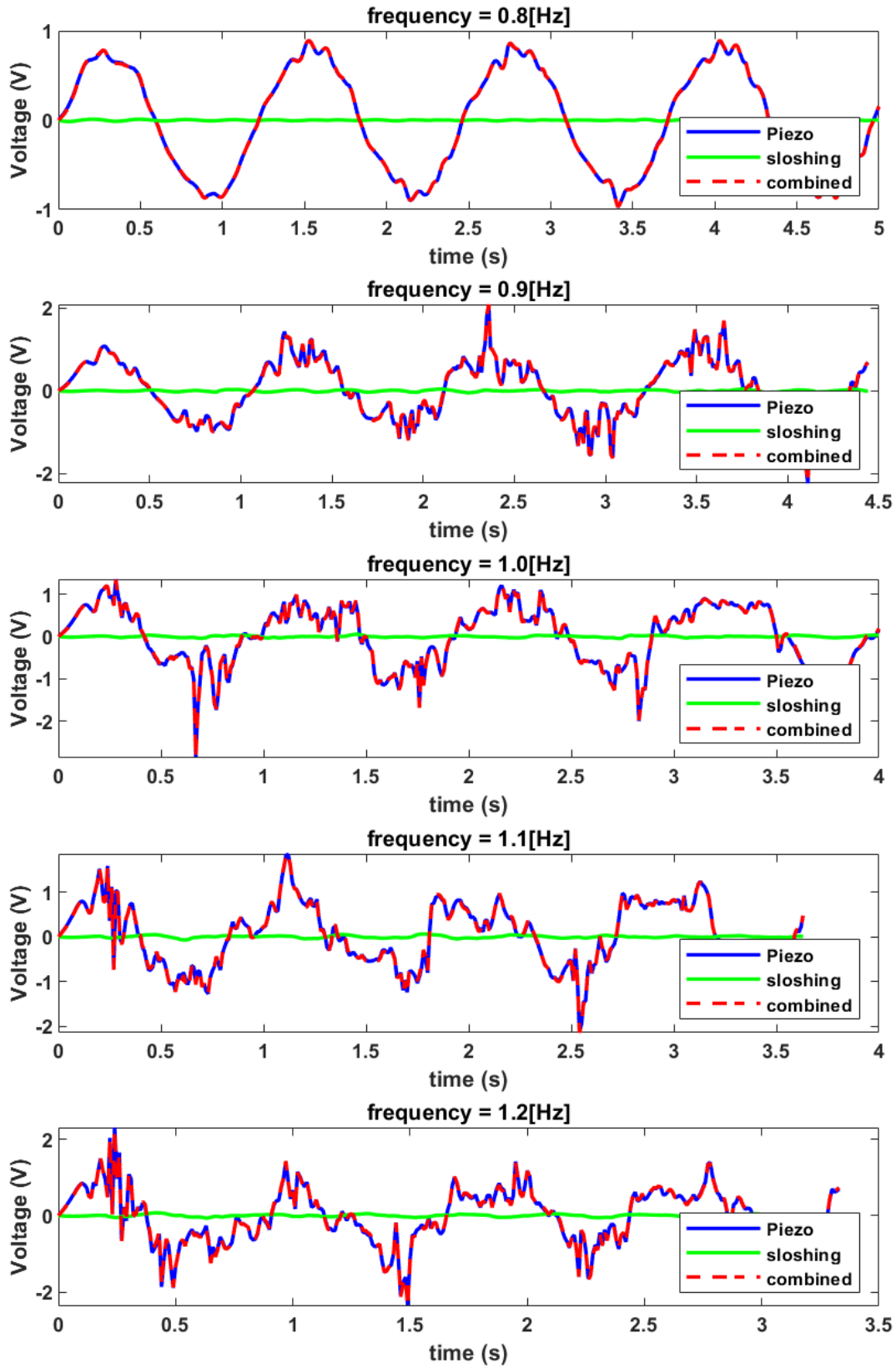


Figure 75 Case3 time evolution for different frequencies with PVDF

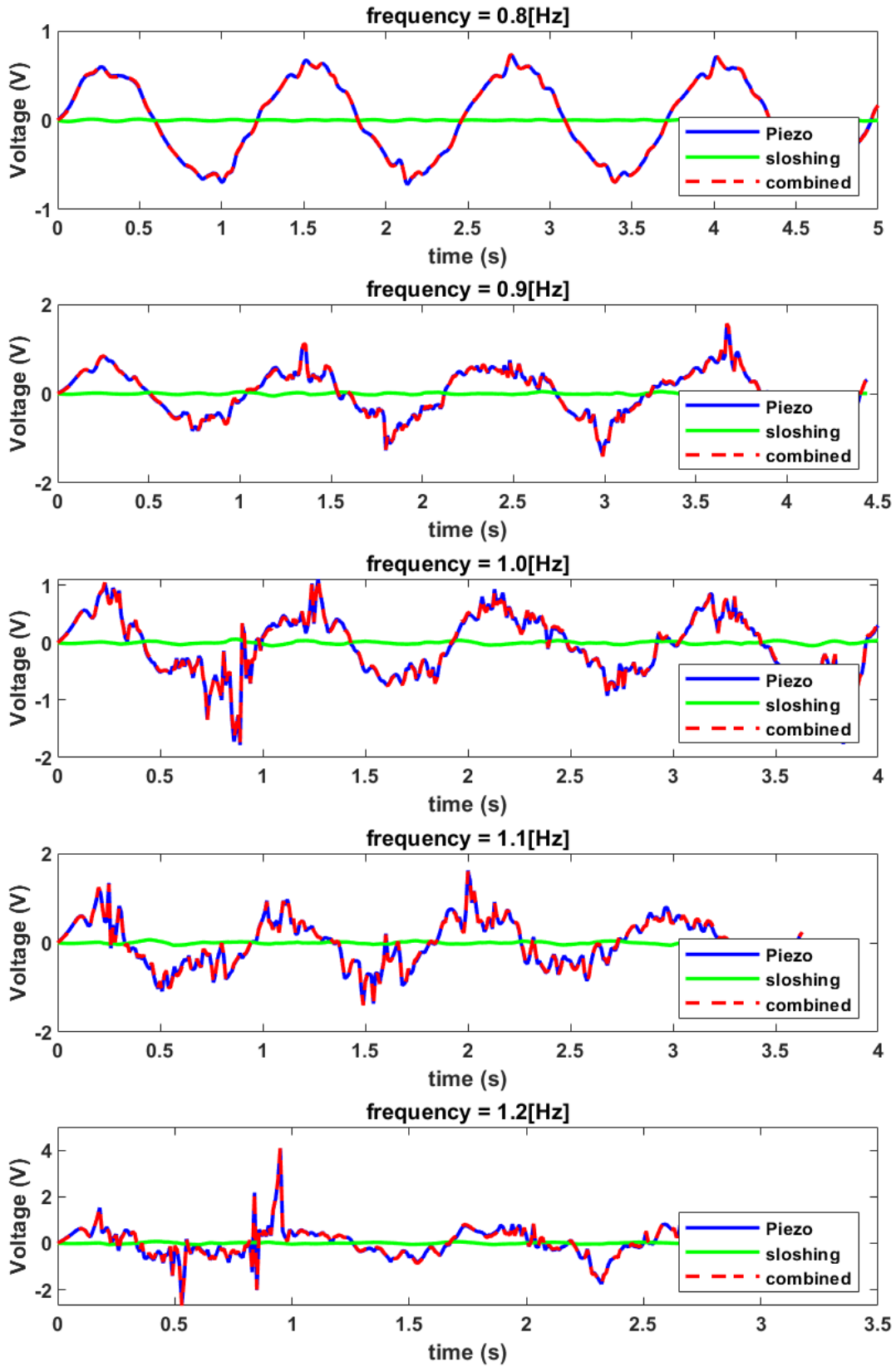


Figure 76 Case4 time evolution for different frequencies with PVDF

Appendix C: Physical properties of materials

Properties of EFH3 FerroTec corporation:

Property	Value
Viscosity	12 [mPa-s]
Density	1420 [kg/m ³]
Surface Tension	24.15 [mN/m]
Magnetic susceptibility	3.52
Saturation magnetization	65 [mT]

Properties of Lead Zirconate Titanate (PZT-7A) are as follows:

The elastic compliance matrix is given by:

$$s_E = \begin{bmatrix} 10.7 & -3.58 & -4.6 & 0.00 & 0.00 & 0.00 \\ -3.58 & 10.7 & -4.6 & 0.00 & 0.00 & 0.00 \\ -4.6 & -4.6 & 13.9 & 0.00 & 0.00 & 0.00 \\ 0.00 & 0.00 & 0.00 & 34.0 & 0.00 & 0.00 \\ 0.00 & 0.00 & 0.00 & 0.00 & 34.0 & 0.00 \\ 0.00 & 0.00 & 0.00 & 0.00 & 0.00 & 28.6 \end{bmatrix} \times 10^{-12} \left(\frac{1}{Pa} \right)$$

The strain coefficient matrix is given by:

$$d = \begin{bmatrix} 0.00 & 0.00 & 0.00 & 0.00 & 36.0 & 0.00 \\ 0.00 & 0.00 & 0.00 & 36.0 & 0.00 & 0.00 \\ -6.00 & -6.00 & 15.3 & 0.00 & 0.00 & 0.00 \end{bmatrix} \times 10^{-11} \left(\frac{C}{N} \right)$$

The dielectric permittivity matrix is given by:

$$\epsilon^T = \begin{bmatrix} 930 & 0.00 & 0.00 \\ 0.00 & 930 & 0.00 \\ 0.00 & 0.00 & 425 \end{bmatrix} \times \epsilon_0$$

Where, ϵ_0 is the permittivity of free space.

Properties of Polyvinylidene Flouride (PVDF) are as follows:

The elastic compliance matrix is given by:

$$s_E = \begin{bmatrix} 3.78 & -1.48 & -1.72 & 0.00 & 0.00 & 0.00 \\ -1.48 & 3.78 & -1.72 & 0.00 & 0.00 & 0.00 \\ -1.72 & -1.72 & 10.9 & 0.00 & 0.00 & 0.00 \\ 0.00 & 0.00 & 0.00 & 14.3 & 0.00 & 0.00 \\ 0.00 & 0.00 & 0.00 & 0.00 & 11.1 & 0.00 \\ 0.00 & 0.00 & 0.00 & 0.00 & 0.00 & 11.1 \end{bmatrix} \times 10^{-10} \left(\frac{1}{Pa} \right)$$

The strain coefficient matrix is given by:

$$d = \begin{bmatrix} 0.00 & 0.00 & 0.00 & 0.00 & 0.00 & 0.00 \\ 0.00 & 0.00 & 0.00 & 0.00 & 0.00 & 0.00 \\ 13.58 & 1.476 & -33.8 & 0.00 & 0.00 & 0.00 \end{bmatrix} \times 10^{-12} \left(\frac{C}{N} \right)$$

The dielectric permittivity matrix is given by:

$$\epsilon^T = \begin{bmatrix} 7.4 & 0.00 & 0.00 \\ 0.00 & 9.3 & 0.00 \\ 0.00 & 0.00 & 7.74 \end{bmatrix} \times \epsilon_0$$

Where, ϵ_0 is the permittivity of free space.